QUANTIFICATION OF SHEAR STRESS IN A MEANDERING NATIVE TOPOGRAPHIC CHANNEL USING A PHYSICAL HYDRAULIC MODEL

Prepared for the

U. S. Department of the Interior
Bureau of Reclamation
Albuquerque Area Office
555 Broadway N.E., Suite 100
Albuquerque, New Mexico 87102-2352

Prepared by

Michael E. Ursic, Christopher I. Thornton, Amanda L. Cox, and Steven R. Abt

July 2012

Colorado State University
Daryl B. Simons Building *at the*
Engineering Research Center
Fort Collins, Colorado 80523

Colorado State University

QUANTIFICATION OF SHEAR STRESS IN A MEANDERING NATIVE TOPOGRAPHIC CHANNEL USING A PHYSICAL HYDRAULIC MODEL

Prepared by

Michael E. Ursic, Christopher I. Thornton, Amanda L. Cox, and Steven R. Abt

July 2012

Colorado State University
Daryl B. Simons Building *at the*
Engineering Research Center
Fort Collins, Colorado 80523

Colorado State University

EXECUTIVE SUMMARY

Current guidelines for predicting increases in shear stress in open-channel bends were developed from investigations that were primarily prismatic in cross section. This study provides possible increases in shear stress relative to approach flow conditions resulting from planimetric and topographic geometric features. Boundary shear stress estimates were determined by several methods utilizing Acoustic Doppler Velocimeter (ADV) and Preston tube data in a physical model of a full meander representing native topographic features found in the Middle Rio Grande. Methods examined include: the law of the wall, Preston tube, turbulent Reynolds stress approximations, and a turbulent kinetic energy (TKE) proportionality constant approach.

Results from each method were compared by magnitude and distribution and limitations were noted. Measured boundary shear stresses in the bend were, in some instances, nearly thirteen times the approach shear stress. Relationships were determined for the expected increase that may provide practical application. Measured bend velocities were four times greater than approach velocities and relationships were determined between velocity and bend geometry. Multipliers for shear stress and velocities were determined for 1-D model results.

TABLE OF CONTENTS

LIST OF FIGURES

LIST OF TABLES

LIST OF SYMBOLS, UNITS OF MEASURE, AND ABBREVIATIONS

Symbols

a	=	inner radius of stagnation tube [L]
α_m	=	meander amplitude [L]
c	=	intercept
C	=	turbulent kinetic energy proportionality constant [dimensionless]
d	=	diameter of the Pitot tube [L]
d_s	=	grain size [L]
dH	=	differential head [L]
dP	=	differential pressure measured from Preston tube [L]
dV	=	differential voltage [$ML^2T^{-2}Q^{-1}$]
D_{50}	=	median sediment size of bed material [L]
δ	=	laminar sublayer thickness [L]
ε	=	percent increase
Fr	=	Froude number [dimensionless]
ϕ_b	=	local angle of the scoured bed with the horizontal
ϕ_m	=	bend deflection angle
g	=	gravitational acceleration [LT^{-2}]
γ	=	specific weight of water [$ML^{-2}T^{-2}$]
h	=	flow depth [L]
h_c	=	height of the center of stagnation tube from the zero datum (z_o) [L]
η	=	y/h [dimensionless]
θ	=	deviation or misalignment angle
k	=	von Kármán constant [dimensionless]
k_s	=	sand grain roughness height [L]
k_s'	=	grain roughness height [L]
K	=	conveyance [L^3T^{-1}]
K_b	=	ratio of shear stress in a bend to the straight channel shear stress [dimensionless]
$K_{b,NT}$	=	shear stress multiplier for natural topography [dimensionless]
$K_{b,TRAP}$	=	shear stress multiplier for trapezoidal channels [dimensionless]
$K_{bHEC\text{-}RAS}$	=	relative shear stress with approach estimates from HEC-RAS [dimensionless]

l_m = mixing length [L]

L_{ch} = channel length [L]

L_v = valley length [L]

λ = meander wavelength [L]

Λ_m = channel meander length [L]

m = regression slope

n = Manning's roughness coefficient [$TL^{(-1/3)}$]

μ = dynamic viscosity [$ML^{-1}T^{-1}$]

v = kinematic viscosity [L^2T^{-1}]

p_o = static pressure measured by static tube [$ML^{-1}T^{-2}$]

P = total pressure measured from Pitot tube [$ML^{-1}T^{-2}$]

P_w = wetted perimeter [L]

Q = flow rate [L^3T^{-1}]

r = inner radius of the stagnation tube [L]

R^2 = coefficient of determination

R_c = radius of curvature [L]

R_c/T_w = relative curvature [dimensionless]

R_h = hydraulic radius [L]

Re_* = grain shear Reynolds number [dimensionless]

ρ = mass density [ML^{-3}]

S_o = bed slope [dimensionless]

S_f = friction slope [dimensionless]

S_w = water-surface slope [dimensionless]

σ = normal stress [$ML^{-1}T^{-2}$]

σ_i = normal force acting on the i plane [$ML^{-1}T^{-2}$]

t = time [T]

T_w = top width of channel at current flow rate [L]

τ = shear stress [$ML^{-1}T^{-2}$]

$\bar{\tau}_{app}$ = average approach boundary shear stress [$ML^{-1}T^{-2}$]

$\bar{\tau}_{appHEC-RAS}$ = HEC-RAS average approach boundary shear stress [$ML^{-1}T^{-2}$]

τ_b = side shear stress on the channel [$ML^{-1}T^{-2}$]

$\tau_b{}^x$	=	bed shear stress acting in the x direction [ML^{-1}T^{-2}]
$\tau_b{}^y$	=	bed shear stress acting in the y direction [ML^{-1}T^{-2}]
τ_d	=	shear stress in channel at maximum depth [ML^{-1}T^{-2}]
τ_{ij}	=	shear stress acting on the *i* plane in the *j* direction [ML^{-1}T^{-2}]
τ_m	=	maximum shear stress in the bend [ML^{-1}T^{-2}]
τ_{max}	=	maximum shear stress [ML^{-1}T^{-2}]
$\tau_{max\ HEC\text{-}RAS}$	=	maximum shear stress from HEC-RAS [ML^{-1}T^{-2}]
τ_o	=	boundary shear stress [ML^{-1}T^{-2}]
$\overline{\tau_o}$	=	mean measured boundary shear stress [ML^{-1}T^{-2}]
τ_x	=	shear stress acting on the *x* plane [ML^{-1}T^{-2}]
τ_{xy}	=	shear stress acting on the *x* plane in the *y* direction [ML^{-1}T^{-2}]
τ_{xz}	=	shear stress acting on the *x* plane in the *z* direction [ML^{-1}T^{-2}]
τ_y	=	shear stress acting on the *y* plane [ML^{-1}T^{-2}]
τ_{yx}	=	shear stress acting on the *y* plane in the *x* direction [ML^{-1}T^{-2}]
τ_{yz}	=	shear stress acting on the *y* plane in the *z* direction [ML^{-1}T^{-2}]
τ_z	=	shear stress acting on the *z* plane [ML^{-1}T^{-2}]
τ_{zx}	=	shear stress acting on the *z* plane in the *x* direction [ML^{-1}T^{-2}]
τ_{zy}	=	shear stress acting on the *z* plane in the *y* direction [ML^{-1}T^{-2}]
u	=	mean velocity in the stream-wise flow direction [LT^{-1}]
u^+	=	v_x/u_* [dimensionless]
$\overline{u}$	=	average velocity in the stream-wise direction [LT^{-1}]
u_*	=	shear velocity [LT^{-1}]
u'	=	velocity fluctuation in the stream-wise flow direction [LT^{-1}]
$\overline{u'v'} = \overline{v'u'}$	=	covariance of velocity fluctuations in the stream-wise and transverse flow directions [L^{2}T^{-2}]
$\overline{u'w'} = \overline{w'u'}$	=	covariance of velocity fluctuations in the stream-wise and vertical flow directions [L^{2}T^{-2}]
v	=	mean velocity in the transverse flow direction [LT^{-1}]
v'	=	velocity fluctuation in the transverse flow direction [LT^{-1}]
v_x	=	component of velocity in *x*-direction (downstream) [LT^{-1}]
v_y	=	component of velocity in *y*-direction (transverse) [LT^{-1}]

v_z	=	component of velocity in z-direction (vertical) $[LT^{-1}]$
V	=	mean cross-sectional velocity $[LT^{-1}]$
V_{app}	=	approach velocity to a bend $[LT^{-1}]$
V_b	=	relative velocity [dimensionless]
V_{max}	=	maximum velocity $[LT^{-1}]$
w	=	mean velocity in the vertical flow direction $[LT^{-1}]$
$\bar{w}$	=	average velocity in the vertical direction $[LT^{-1}]$
w'	=	velocity fluctuation in the vertical flow direction $[LT^{-1}]$
$\overline{w'v'} = \overline{v'w'}$	=	covariance of velocity fluctuations in the transverse and vertical flow directions $[L^2T^{-2}]$
x	=	downstream (stream-wise) flow direction
ξ	=	relative curvature or tortuosity [dimensionless]
y	=	vertical distance from the boundary $[L]$
y	=	transverse flow direction
y^+	=	u_*y/v $[L]$
y/h	=	relative depth [dimensionless]
y_o	=	zero velocity roughness height $[L]$
z	=	vertical flow direction
z	=	vertical distance from the boundary $[L]$
z_o	=	zero datum $[L]$
Ω	=	channel sinuosity [dimensionless]

Units of Measure

cfs	cubic feet per second
cm	centimeter(s)
°	degree(s)
ft	feet or foot
ft/s	feet per second
Hz	Hertz
in.	inch(es)
mA	milliampere(s)
mi	mile(s)
mi^2	square mile(s)

%	percent
psf	pound(s) per square foot
sec	second(s)
slug(s)/ft^3	slug(s) per cubic foot
V	Volt(s)

Abbreviations

*	denotes calculated estimates from given parameters
-	denotes fields that are not applicable and/or data that were not provided
®	registered
1 – 18	model cross-section locations
a – g	test point locations on each cross section
A – F	measurement sections from Dey and Barbhuiya (2005)
1-D	one-dimensional
2-D	two-dimensional
3-D	three-dimensional
ADV	Acoustic Doppler Velocimeter
COR	correlations
FHWA	Federal Highway Administration
HEC-15	*Hydraulic Engineering Circular No. 15*
HEC-RAS	Hydrologic Engineering Center's River System Analysis
LDA	Laser Doppler Anemometer
LiDAR	Light Detection and Ranging
SNR	sound-to-noise ratio
TKE	turbulent kinetic energy
USACE	U. S. Army Corps of Engineers
USBR	U. S. Bureau of Reclamation

1 INTRODUCTION

1.1 General Background

Fluvial systems respond to changes in boundary conditions in order to sustain the flow and sediment supplied to the system. Local channel responses are typically difficult to predict due to possible affects from upstream, downstream, or local boundary conditions that cause changes in channel or planform geometry. Changes to the system can threaten riverside infrastructure and riparian zones, which may affect the local ecology. This research focuses on meandering channel patterns and the forces applied to their physical boundaries by the complex three-dimensional (3-D) flow found in meandering bends.

1.2 Project Background

The Middle Rio Grande is a 29-mi reach of the Rio Grande in central New Mexico that extends from downstream of Cochiti Dam, to Bernalillo, New Mexico. Figure 1.1 presents a location map of the Middle Rio Grande reach. In recent years, the Middle Rio Grande has been the focus of channel-restoration techniques including the use of native material and rock weir structures in attempts to control bank erosion rates, channel migration rates, and habitat degradation (Darrow 2004).
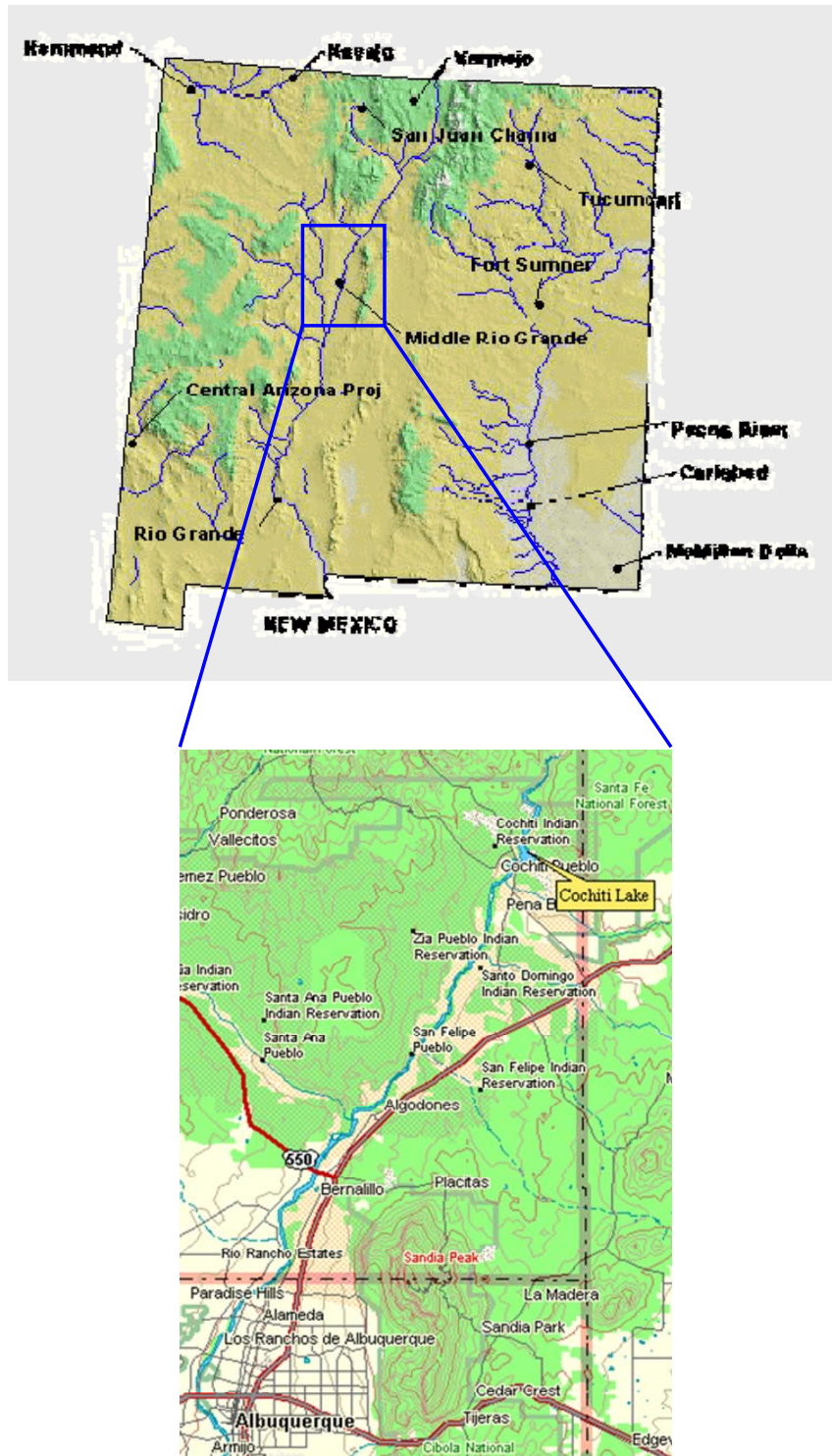
Figure 1.1: Location Map of Project Reach (Walker 2008)

In 1973, the Cochiti Dam was built to provide flood control and sediment detention for the Albuquerque area. Consequently, the dam traps nearly all the sediment supplied by a 14,600

mi^2 watershed causing a sediment deficiency in the Middle Rio Grande (Richard 2001). The river has responded to the lack of sediment by altering channel pattern from braided to meandering. Accompanied with the change in morphology, lateral migration has impacted riverside infrastructure as well as riparian vegetation and aquatic habitat (Heintz 2002). In a mitigation effort, the U. S. Bureau of Reclamation (USBR) has implemented a channel-maintenance program to stabilize the channel with an additional goal of improving habitat. In-stream structures such as bendway weirs have proven to stabilize banks, while providing diverse flow fields attractive to many aquatic species (Davinroy *et al*. 1998, Shields *et al*. 1998, Derrick 1998). Although bendway weirs have proven a suitable alternative to traditional methods, little to no design guidelines have been created. Previous implemented designs have largely been based upon engineering judgment. Colorado State University was contracted to determine hydraulic effects of in-stream structures to assist in the Middle Rio Grande mitigation effort.

1.3 Research Objectives

This research was conducted as a supplementary effort to research conducted on bendway weir design in a native topographic channel. The objectives were to compare shear stress calculation methods with data collected in a 3-D flow field and determine appropriate increases in shear stress due to bends, and correlate them with geometric features. The following steps were taken to conduct the shear stress comparison research:

- Conduct a thorough literature review of previous experimental work on shear stress in bends.
- Conduct a thorough literature review on methods available for estimating shear stress and instances where applied in a 3-D flow field.
- Calculate shear stresses by methods reviewed and display magnitudes and distributions for each testing configuration.
- Compare shear stress calculation methods to previous work and known characteristics of flow in bends.
- Provide guidelines that may be applicable in practice for determining the increase in shear stress due to secondary circulation and variable cross-sectional geometry.
- Provide guidelines that may be applicable in practice for determining the increase in velocity due to radial acceleration and native topographic features.

2 LITERATURE REVIEW

2.1 Introduction

Shear stress is used as an indicator in fluvial studies to predict locations of erosion or deposition. Erosion is particularly important for meandering channels where infrastructure and riparian zones are susceptible to changes in planform geometry. Extensive research has previously been conducted to assist in the prediction and prevention of changes in planform geometry by examining shear stress distributions in bends with variations in geometric and flow parameters. A review was conducted on previous experimental studies of shear stress distributions in bends and selected methodologies pertinent to this study for estimation of localized shear stress.

2.2 Shear Stress Distribution in Bends

Bends in meandering streams have been examined by researchers for decades to understand the distribution of velocity and shear stress and its effect on bend migration (Chen and Shen 1984). Complex nature of flow in bends is influenced by channel geometry characteristics, flow characteristics, and fluid and sediment properties (Yen 1965). Shear stresses are directly affected by local accelerating, decelerating, and secondary flows (Ippen *et al*. 1960). By isolating variables, researchers have developed relationships between boundary shear stress and geometric characteristics. Herein, a review of geometric descriptors and flow in bends are presented to facilitate an in-depth evaluation of experimental research.

2.2.1 Review of Fundamentals

Planimetric variables are useful in the description and analysis of meandering channels. Meandering channels, in general, are classified as having a sinuosity of 1.5 or greater (Knighton 1998). Sinuosity (Ω) is defined as the ratio of channel length (L_{ch}) to the corresponding valley

length (L_v) as presented in Figure 2.1 (Richards 1982). Other planimetric variables used to describe a meandering stream are defined in Figure 2.1 and include the radius of curvature (R_c), amplitude of meander (α_m), meander wavelength (λ), channel top width (T_w), and total angle of the bend (ϕ_m).
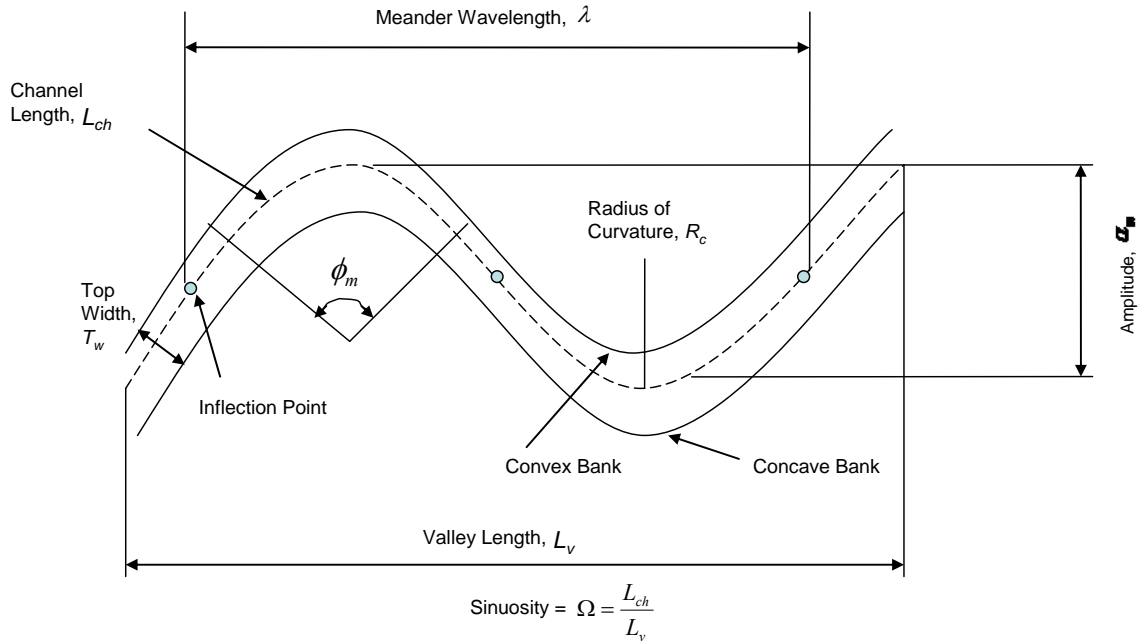
Figure 2.1: Planimetric Variables (adapted from Richards (1982))

Flow fields in meandering streams are controlled in large part by channel curvature and bed topography (Dietrich 1987). Relative curvature, or tortuosity (ξ), is a dimensionless ratio found to be important in the determination of shear stress distributions due to its influence on secondary circulation (Chen and Shen 1984, Knighton 1998). Relative curvature is the ratio of bend curvature to top width of the stream bend as presented in Equation 2.1:

$$\xi = \frac{R_c}{T_w}$$

Equation 2.1

where

ξ = tortuosity or relative curvature [dimensionless];

R_c = radius of curvature [L]; and

T_w = channel top width [L].

5

A characteristic spiral flow in bends results from centripetal acceleration directed to the outer bank. Near the bed, centripetal acceleration is influenced by a boundary causing a differential to the acceleration near the free surface. Differential forces result in tilting of the free surface against the outer bank and a transverse pressure gradient. Centrifugal acceleration coupled with super-elevation, or tilting of the free surface, causes larger velocities near the free surface directed toward the outer bank and slower near-bed velocities directed toward the inner bank. Secondary circulation is often referred to as helical flow as depicted in Figure 2.2 (Dietrich 1987, Knighton 1998, Thomson 1876).
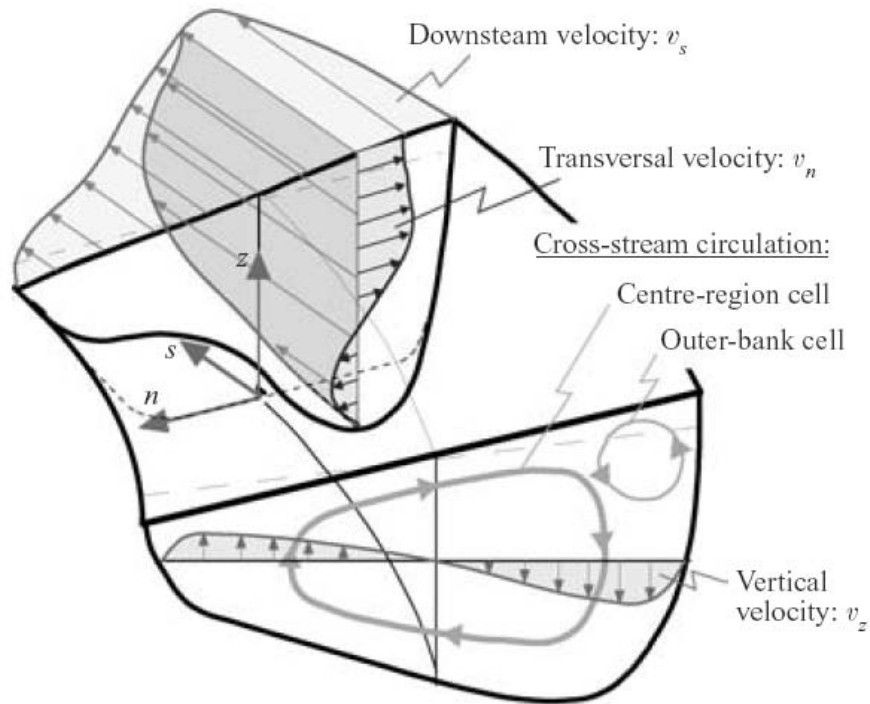
Figure 2.2: Secondary Flow Characteristics (Blanckaert and de Vriend 2004)

Velocity vectors in the stream-wise direction coupled with transverse vectors resulting from secondary circulation cause variations in boundary shear stress. Shear on the outer bank is large compared to shear on the inner bank due to the presence of super-elevation and the locally steep downstream energy gradient. Result of the cross-section differential shear, assuming homogeneous bed and bank material, is asymmetry of the cross section where the outer and inner banks can be described as concave and convex, respectively. Markham and Thorne (1992) divided bend cross sections into three identifiable flow regions: 1) a mid-channel region where the primary helicoidal and main downstream flow exists; 2) an outer bank region that exhibits an

6

opposite rotational cell from that of the primary helical motion; and 3) an inner bank region where outward flow is a result of shoaling over a point bar (Dietrich 1987, Knighton 1998). Figure 2.3 illustrates the bend cross-section regions identified by Markham and Thorne (1992).
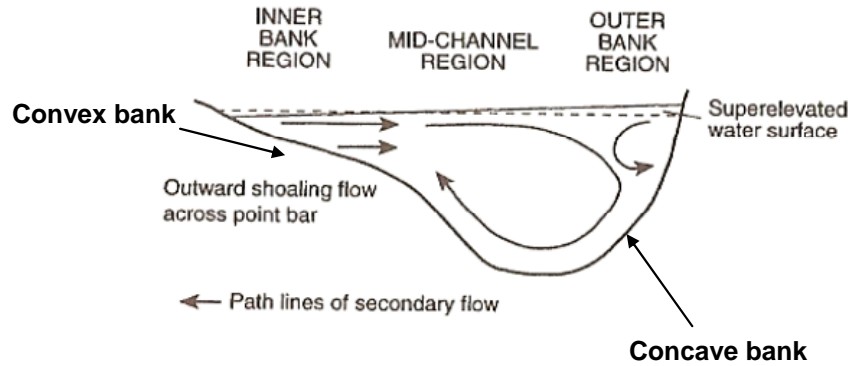
Figure 2.3: Cross-sectional Characteristics of Flow in a Bend (adapted from Knighton (1998))

Maximum shear stress is generally present just downstream of the bend apex where secondary circulation is strongest as seen in Figure 2.4.   As flow exits a bend, secondary circulation begins to decrease and is eventually dissipated near or in the second bend as opposing centripetal acceleration establishes secondary flows as seen in Figure 2.5.   While the general flow pattern is known, it is noted that shear stress is not temporally or spatially constant as it varies with discharge, bend tightness, and cross-sectional form (Knighton 1998).
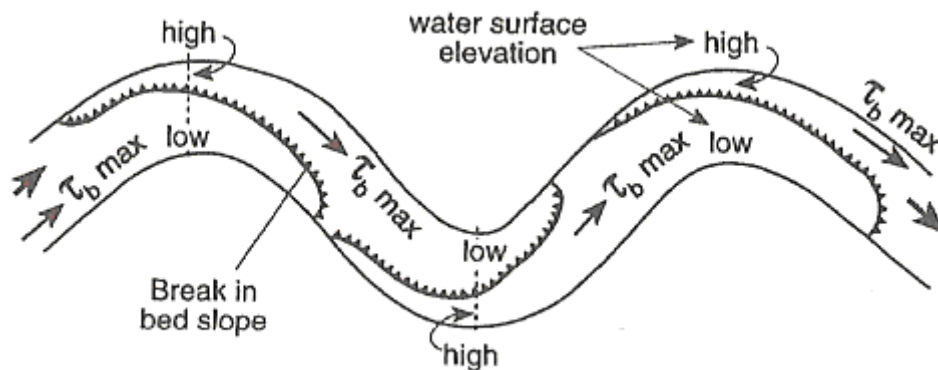
Figure 2.4: Generalized Shear Stress Distribution in Meandering Channels (Knighton (1998) after Dietrich (1987))
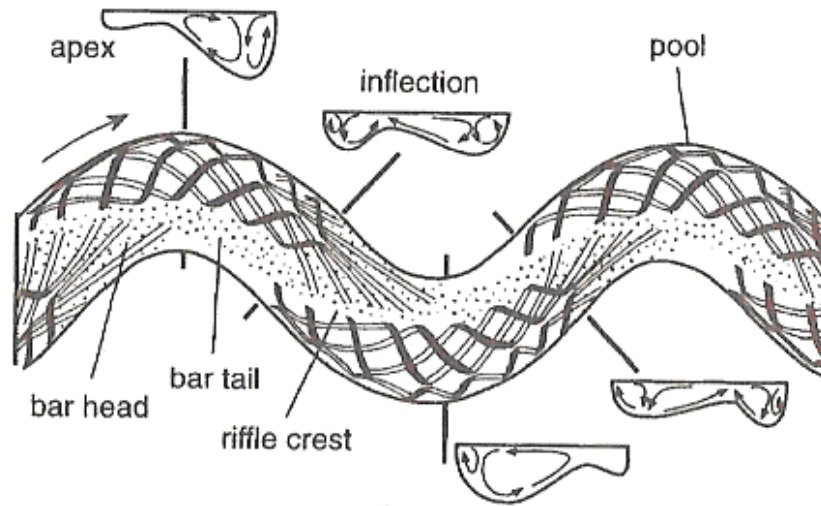
Figure 2.5: Flow Variation between Meanders (Knighton (1998) after Thompson (1986))

Large-scale bank erosion is initiated by fluvial attack of bank material at the base or toe of the outer bank. As base material is eroded, mass failure can occur due to gravitational forces. Basal clean-out removes material introduced by mass failure (Thorne 1991) and the process continues until quasi-equilibrium is established. Large-scale bank erosion processes are a major contributor to channel migration rates and are directly affected by relative curvature (Ippen *et al.* 1962), bed and bank materials (Simon *et al.* 2000), presence of the counter-rotating cell (Blanckaert and de Vriend 2004), vegetation (Shields *et al.* 2009, Simon *et al.* 2000), pore pressure gradient of the bank (Shields *et al.* 2009), transport capacity, and erosive or shear forces (Thorne 1991). Figure 2.6 presents a relationship of relative curvature to channel migration rates (Hicken and Nanson 1984). Maximum migration rates occur between $2 < R_c/T_w < 3$ as illustrated in Figure 2.6. Scatter of the plotted data can be attributed to the many aforementioned factors controlling bank erosion processes.
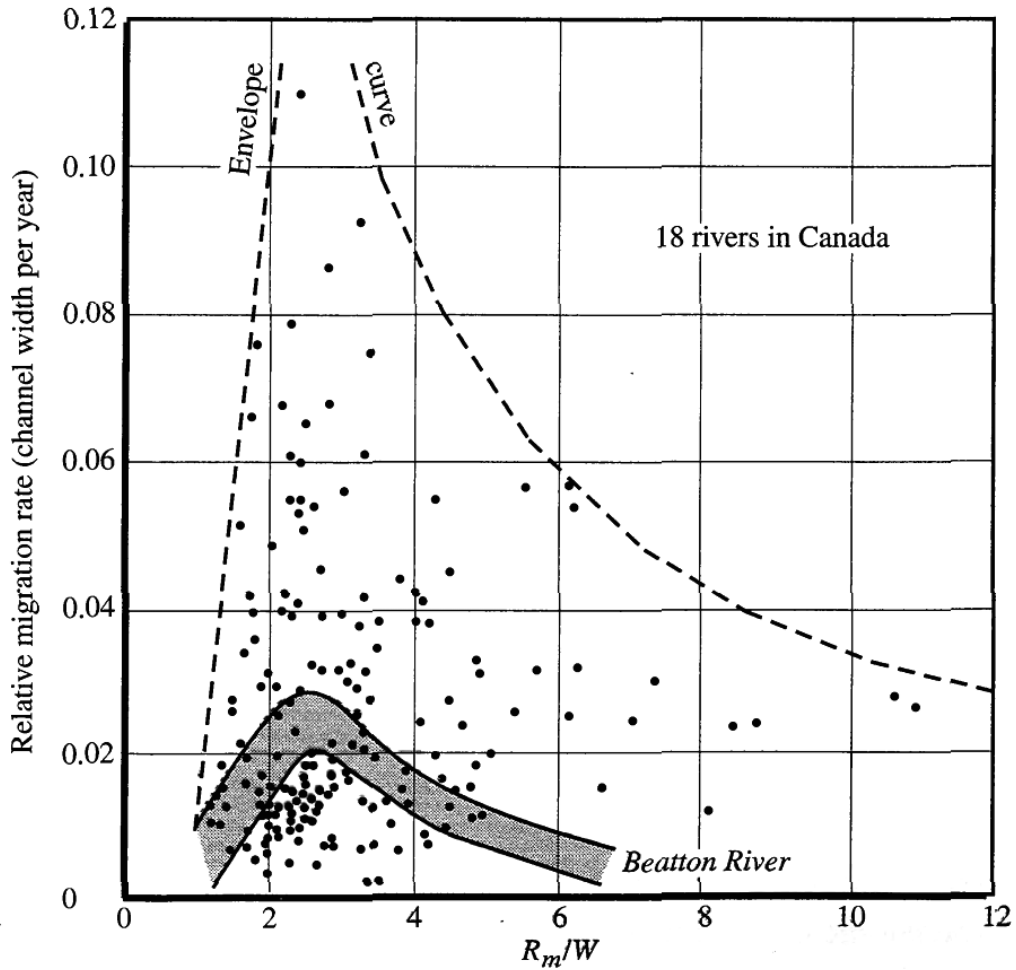
Figure 2.6: Relative Curvature and its Relation to Channel Migration Rates (Hickin and Nanson 1984)

Planform geometry in meandering channels can vary considerably and cause variations in entrance conditions to sequential bends. Figure 2.7 provides examples of different types of meandering streams. Variations in entrance conditions can change the location of the maximum shear stress (Bathurst 1979, Ippen *et al.* 1960, 1962) and, if assuming consistent bank material throughout the bend, variations in planform change. Figure 2.8 presents several methods in which meandering bends can evolve.

IRREGULAR MEANDERS

River Dean, Cheshire

REGULAR MEANDERS

River Myittha, Burma

Confined pattern

River Beaver, Canada

River Neyinzaya, Burma

TORTUOUS MEANDERS

River Bollin, Cheshire
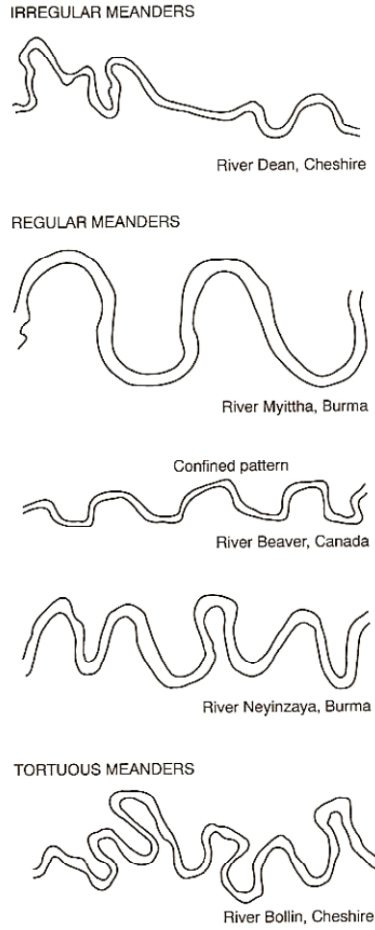
Figure 2.7: Types of Meanders (Knighton 1998)

TRANSLATION

ROTATION

EXTENSION

LOBING
AND
COMPOUND
GROWTH
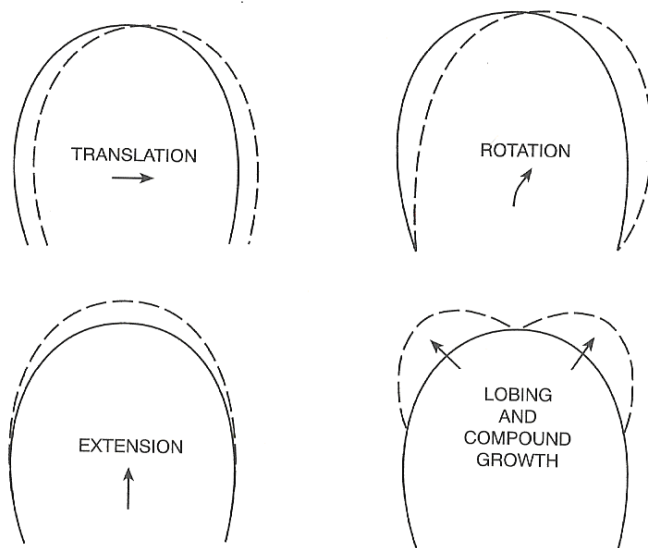
Figure 2.8: Methods for Bend Evolution (Knighton 1998)

10

Variation in the location of maximum shear stress in bends coupled with the many complex factors controlling bank erosion processes contribute to how bend evolution occurs. Experimental observations are needed to further understand the roles of complex factors contributing to bank erosion and meandering processes at both local and system-wide scales.

2.2.2 Previous Experiments

Previous studies have provided a wealth of information on shear stress distributions in bends and a strong foundation for this study. Discussions of general findings by each investigator(s) are presented in following subsections. Testing configurations and results of each investigator(s) are presented in Table 2.1 and Table 2.2.

Table 2.1: Summary of Channel Characteristics Given for Each Study Presented

Study	Reference Number	Q (cfs)	Average Velocity (ft/s)	R_c (ft)	T_w (ft)	Depth, h (ft)	R_c/T_w	T_w/h	τ_o (psf)	τ_{max}/τ_o	Bend Angle (°)	Fr	Boundary Type
Ippen et al. (1960)	1	0.85	1.36	6.5	3.0	0.25	2.17	12.1	0.007	2	60	0.53	Smooth
Ippen et al. (1960)	2	1.27	1.5	6.6	3.3	0.32	2.02	10.2	0.009	1.78	60	0.52	Smooth
Ippen et al. (1960)	3	1.27	1.5	6.6	3.3	0.33	2.02	9.9	0.009	2.22	60	0.52	Smooth
Ippen et al. (1960)	4	1.27	1.5	6.6	3.3	0.33	2.02	9.9	0.009	2.86	60	0.52	Smooth
Ippen et al. (1960)	5	2.02	1.67	6.9	3.7	0.42	1.86	8.7	0.101	2.2	60	0.52	Smooth
Ippen et al. (1960)	6	2.86	1.91	7.0	4.0	0.50	1.75	8.0	0.015	2.4	60	0.55	Smooth
Ippen et al. (1960)	7	2.86	1.91	7.0	4.0	0.50	1.75	8.0	0.012	2.4	60	0.55	Smooth
Ippen et al. (1960)	8	2.86	1.91	7.0	4.0	0.50	1.75	8.0	0.012	3	60	0.55	Smooth
Ippen et al. (1960)	9	0.96	1.08	6.7	3.3	0.33	2.00	10.0	0.013	2	60	0.38	Rough
Ippen et al. (1962)	10	0.85	1.36	5.0	3.0	0.2	1.67	12	0.007	2	60	0.53	Smooth
Ippen et al. (1962)	11	1.27	1.5	4.8	3.2	0.32	1.49	10	0.009	1.78	60	0.52	Smooth
Ippen et al. (1962)	12	2.02	1.67	5.1	3.7	0.423	1.37	8.8	0.010	2.2	60	0.52	Smooth
Ippen et al. (1962)	13	2.86	1.91	5.0	4.0	0.5	1.25	8	0.015	2.4	60	0.55	Smooth
Ippen et al. (1962)	14	0.19	0.87	5.8	1.7	0.17	3.45	10	0.003	1.6	60	0.42	Smooth
Ippen et al. (1962)	15	0.45	1.19	5.9	2.0	0.25	2.94	8	0.006	1.6	60	0.48	Smooth
Ippen et al. (1962)	16	0.77	1.4	5.8	2.3	0.33	2.50	7	0.007	1.75	60	0.51	Smooth
Ippen et al. (1962)	17	0.84	0.94	4.9	3.3	0.33	1.49	10	0.009	2.5	60	0.32	Rough
Ippen et al. (1962)	18	1.77	1.18	5.0	4.0	0.50	1.25	8	0.012	2.8	60	0.34	Rough
Ippen et al. (1962)	19	1.27	1.5	4.8	3.2	0.32	1.49	10	0.008	2.22	60	0.52	Smooth
Ippen et al. (1962)	20	2.86	1.91	5.0	4.0	0.5	1.25	8	0.012	2.4	60	0.55	Smooth
Ippen et al. (1962)	21	1.27	1.5	4.8	3.2	0.32	1.49	10	0.008	2.86	60	0.52	Smooth
Ippen et al. (1962)	22	2.86	1.91	5.0	4.0	0.5	1.25	8	0.012	3	60	0.55	Smooth
USBR (1964)	23	2.85	1.2	16	4.3*	0.75	3.8*	5.0*	0.006*	1.3*	15	0.3	Smooth
Yen (1965)	24	2.93*	2.68	28	6.7*	0.35	4.2*	19*	0.029	1.2	90	0.82	Smooth
Yen (1965)	25	4.76*	3.14	28	6.9*	0.50	4.0*	14*	0.037	1.3	90	0.81	Smooth
Yen (1965)	26	3.5*	2.27	28	7.0*	0.51	4.0*	14*	0.020	1.3	90	0.58	Smooth
Yen (1965)	27	2.2*	1.4	28	7.0*	0.52	4.0*	14*	0.008	1.3	90	0.36	Smooth
Yen (1965)	28	1.36*	0.626	28	7.4*	0.75	3.8*	10*	0.011	1.3	90	0.37	Smooth
Hooke (1975)	29	0.35	0.63	7.40	3.35	0.17	2.2	20	0.023	2	55	0.27	Rough
Hooke (1975)	30	0.71	0.90	7.40	3.43	0.24	2.2	14	0.029	1.5	55	0.33	Rough
Hooke (1975)	31	1.24	1.21	7.40	3.32	0.31	2.2	11	0.042	1.5	55	0.38	Rough
Hooke (1975)	32	1.77	1.29	7.40	3.36	0.42	2.2	8	0.056	1.75	55	0.35	Rough
Nouh and Townsend (1979)	33	0.13	1.0	2.95	0.98	0.13	3	7.5	-	1.8	45	0.49	Rough
Nouh and Townsend (1979)	34	0.13	1.0	2.95	0.98	0.13	3	7.5	-	2.4	60	0.49	Rough
Bathurst (1979)	35	40	1.6	232	30.8	0.80	7.5	38.4	0.046	-	62	0.32	Rough

Study	Reference Number	Q (cfs)	Average Velocity (ft/s)	R_c (ft)	T_w (ft)	Depth, h (ft)	R_c/T_w	T_w/h	τ_o (psf)	τ_{max}/τ_o	Bend Angle (º)	Fr	Boundary Type
Bathurst (1979)	36	83	1.8	231	39.4	1.15	5.9	34.3	0.064	-	62	0.31	Rough
Bathurst (1979)	37	32	0.9	144	28.7	1.24	5.0	23.1	0.009	-	50	0.15	Rough
Bathurst (1979)	38	58	1.3	139	27.9	1.49	5.0	18.7	0.017	-	50	0.19	Rough
Bathurst (1979)	39	86	1.8	144	27.6	1.69	5.2	16.3	0.024	-	50	0.25	Rough
Bathurst (1979)	40	373	4.4	144	29.9	2.85	4.8	10.5	0.289	-	50	0.5	Rough
Bathurst (1979)	41	184	1.8	312	59.1	1.69	5.3	35.0	0.047	-	38	0.25	Rough
Bathurst (1979)	42	242	2.1	312	63.6	1.83	4.9	34.9	0.039	-	38	0.28	Rough
Bathurst (1979)	43	547	3.1	312	82.0	2.17	3.8	37.7	0.115	-	38	0.38	Rough
Bathurst (1979)	44	42	0.9	-	47.2	0.95	-	49.9	0.008	-	38	0.17	Rough
Bathurst (1979)	45	505	3.4	-	86.0	1.72	-	50.0	0.132	-	38	0.46	Rough
Tilston (2005)	46	4	0.26	61	16.1	1.05	3.78	15.3	-	-	180	0.07	-
Tilston (2005)	47	7	0.33	61	19.6	1.02	3.09	19.3	-	-	180	0.09	-
Tilston (2005)	48	23	0.85	61	21.2	1.25	2.86	17.0	-	-	180	0.21	-
Tilston (2005)	49	22	0.82	61	20.1	1.31	3.02	15.3	-	-	180	0.2	-
Tilston (2005)	50	44	1.05	61	23.3	1.77	2.60	13.2	-	-	180	0.22	-
Tilston (2005)	51	72	1.67	61	24.9	1.74	2.44	14.3	-	-	180	0.35	-
Sin (2010)	52	8	0.98	39	13.7	0.56	2.82	24.5	0.01	1.79	125	0.23	Rough
Sin (2010)	53	8	1.70	66	9.7	0.61	6.81	15.8	0.03	1.78	73	0.38	Rough
Sin (2010)	54	12	1.13	39	14.8	0.75	2.62	19.7	0.02	1.78	125	0.23	Rough
Sin (2010)	55	12	1.66	66	10.8	0.79	6.12	13.6	0.03	1.88	73	0.33	Rough
Sin (2010)	56	16	1.25	39	15.6	0.89	2.49	17.5	0.02	1.93	125	0.23	Rough
Sin (2010)	57	16	2.05	66	11.5	0.86	5.72	13.4	0.04	1.99	73	0.39	Rough
Sin (2010)	58	20	1.27	39	16.5	1.02	2.35	16.2	0.02	1.99	125	0.22	Rough
Sin (2010)	59	20	2.18	66	12.1	1.04	5.44	11.6	0.04	1.68	73	0.38	Rough

* denotes calculated estimates from given parameters and - denotes data were not provided

Table 2.2: Continuation of Summary of Channel Characteristics Given for Each Study Presented

Study	Reference Number	Mobile Bed	Measurement Technique	Cross-sectional Shape	Configuration
Ippen *et al.* (1960)	1	No	Preston tube	Trapezoidal	single curve, uniform approach
Ippen *et al.* (1960)	2	No	Preston tube	Trapezoidal	single curve, uniform approach
Ippen *et al.* (1960)	3	No	Preston tube	Trapezoidal	double curve, non-uniform approach
Ippen *et al.* (1960)	4	No	Preston tube	Trapezoidal	reverse curve system, non-uniform approach
Ippen *et al.* (1960)	5	No	Preston tube	Trapezoidal	single curve, uniform approach
Ippen *et al.* (1960)	6	No	Preston tube	Trapezoidal	single curve, uniform approach
Ippen *et al.* (1960)	7	No	Preston tube	Trapezoidal	double curve, non-uniform approach
Ippen *et al.* (1960)	8	No	Preston tube	Trapezoidal	reverse curve system, non-uniform approach
Ippen *et al.* (1960)	9	No	Preston tube	Trapezoidal	single curve, uniform approach
Ippen *et al.* (1962)	10	No	Preston tube	Trapezoidal	single curve, uniform approach
Ippen *et al.* (1962)	11	No	Preston tube	Trapezoidal	single curve, uniform approach
Ippen *et al.* (1962)	12	No	Preston tube	Trapezoidal	single curve, uniform approach
Ippen *et al.* (1962)	13	No	Preston tube	Trapezoidal	single curve, uniform approach
Ippen *et al.* (1962)	14	No	Preston tube	Trapezoidal	single curve, uniform approach
Ippen *et al.* (1962)	15	No	Preston tube	Trapezoidal	single curve, uniform approach
Ippen *et al.* (1962)	16	No	Preston tube	Trapezoidal	single curve, uniform approach
Ippen *et al.* (1962)	17	No	Preston tube	Trapezoidal	single curve, uniform approach
Ippen *et al.* (1962)	18	No	Preston tube	Trapezoidal	single curve, uniform approach
Ippen *et al.* (1962)	19	No	Preston tube	Trapezoidal	double curve, non-uniform approach
Ippen *et al.* (1962)	20	No	Preston tube	Trapezoidal	double curve, non-uniform approach
Ippen *et al.* (1962)	21	No	Preston tube	Trapezoidal	reverse curve system, non-uniform approach
Ippen *et al.* (1962)	22	No	Preston tube	Trapezoidal	reverse curve system, non-uniform approach
USBR (1964)	23	No	Preston tube	Trapezoidal	single curve, uniform approach
Yen (1965)	24	No	Preston tube	Trapezoidal	single curve, uniform approach
Yen (1965)	25	No	Preston tube	Trapezoidal	single curve, uniform approach
Yen (1965)	26	No	Preston tube	Trapezoidal	single curve, uniform approach
Yen (1965)	27	No	Preston tube	Trapezoidal	single curve, uniform approach
Yen (1965)	28	No	Preston tube	Trapezoidal	single curve, uniform approach
Hooke (1975)	29	Yes	Preston tube	Dynamic	reverse curve system, non-uniform approach
Hooke (1975)	30	Yes	Preston tube	Dynamic	reverse curve system, non-uniform approach
Hooke (1975)	31	Yes	Preston tube	Dynamic	reverse curve system, non-uniform approach
Hooke (1975)	32	Yes	Preston tube	Dynamic	reverse curve system, non-uniform approach
Nouh and Townsend (1979)	33	Yes	LDA/Logarithmic Law	Rectangular/Dynamic	single curve, uniform approach
Nouh and Townsend (1979)	34	Yes	LDA/Logarithmic Law	Rectangular/Dynamic	single curve, uniform approach
Bathurst (1979)	35	Yes	Ott C31/Logarithmic Law	Natural, gravel bed	reverse curve system, non-uniform approach
Bathurst (1979)	36	Yes	Ott C31/Logarithmic Law	Natural, gravel bed	reverse curve system, non-uniform approach

Study	Reference Number	Mobile Bed	Measurement Technique	Cross-sectional Shape	Configuration
Bathurst (1979)	37	Yes	Ott C31/Logarithmic Law	Natural, gravel bed	reverse curve system, non-uniform approach
Bathurst (1979)	38	Yes	Ott C31/Logarithmic Law	Natural, gravel bed	reverse curve system, non-uniform approach
Bathurst (1979)	39	Yes	Ott C31/Logarithmic Law	Natural, gravel bed	reverse curve system, non-uniform approach
Bathurst (1979)	40	Yes	Ott C31/Logarithmic Law	Natural, gravel bed	reverse curve system, non-uniform approach
Bathurst (1979)	41	Yes	Ott C31/Logarithmic Law	Natural, gravel bed	reverse curve system, non-uniform approach
Bathurst (1979)	42	Yes	Ott C31/Logarithmic Law	Natural, gravel bed	reverse curve system, non-uniform approach
Bathurst (1979)	43	Yes	Ott C31/Logarithmic Law	Natural, gravel bed	reverse curve system, non-uniform approach
Bathurst (1979)	44	Yes	Ott C31/Logarithmic Law	Natural, gravel bed	reverse curve system, non-uniform approach
Bathurst (1979)	45	Yes	Ott C31/Logarithmic Law	Natural, gravel bed	reverse curve system, non-uniform approach
Tilston (2005)	46	Yes	ADV/TKE	Natural, gravel bed	reverse curve system, non-uniform approach
Tilston (2005)	47	Yes	ADV/TKE	Natural, gravel bed	reverse curve system, non-uniform approach
Tilston (2005)	48	Yes	ADV/TKE	Natural, gravel bed	reverse curve system, non-uniform approach
Tilston (2005)	49	Yes	ADV/TKE	Natural, gravel bed	reverse curve system, non-uniform approach
Tilston (2005)	50	Yes	ADV/TKE	Natural, gravel bed	reverse curve system, non-uniform approach
Tilston (2005)	51	Yes	ADV/TKE	Natural, gravel bed	reverse curve system, non-uniform approach
Sin (2010)	52	No	Preston tube	Trapezoidal	single curve, uniform approach
Sin (2010)	53	No	Preston tube	Trapezoidal	reverse curve system, non-uniform approach
Sin (2010)	54	No	Preston tube	Trapezoidal	single curve, uniform approach
Sin (2010)	55	No	Preston tube	Trapezoidal	reverse curve system, non-uniform approach
Sin (2010)	56	No	Preston tube	Trapezoidal	single curve, uniform approach
Sin (2010)	57	No	Preston tube	Trapezoidal	reverse curve system, non-uniform approach
Sin (2010)	58	No	Preston tube	Trapezoidal	single curve, uniform approach
Sin (2010)	59	No	Preston tube	Trapezoidal	reverse curve system, non-uniform approach

LDA denotes a Laser Doppler Anemometer and Ott C31 is a current meter

2.2.2.1 Ippen *et al.* (1960, 1962)

Ippen *et al.* (1960) examined shear stress and velocity distributions in trapezoidal meandering bends with varying entrance conditions. Sediment transport and native topographic features were excluded from this work as this was an "*initial attack on the erosion problem.*" Ippen *et al.* (1960) described flow separation on the inside of a bend that caused a decrease in effective flow area and flow acceleration away from the inner bank. Higher velocities on the outer bank downstream from the bend were found to be a result of three contributing factors: 1) the return to normal flow from the free vortex pattern causing acceleration on the outer bank, 2) separation zone decreasing effective area, and 3) helicoidal flow moving to the outer bank. Shear stress distributions were found to correspond to velocity patterns and flow depths. For the lower flow depths, the maximum shear occurred on the outer bank downstream of the bend; and for the larger flow depths, the maximum shear occurred on the inside bank in the approach to the bend. Maximum shear stresses for the simulated double-bend test were confined to the inner bank at the upstream entrance. Ippen *et al.* (1960) concluded that shear stress distributions are primarily functions of geometry and flow conditions.

Ippen *et al.* (1962) extended the range of stream parameters from that originally reported in Ippen *et al.* (1960). Ratios of top width to flow depth or relative curvature were varied and approach flows were altered to simulate sequential bends for four of the thirteen tests. Ippen *et al.* (1962) determined that as curvature increases so does the magnitude of shear stress relative to that of the approach flow and flow depths were less important than bend curvature on shear stress maximums. Shear stress patterns were reported similar for both rough and smooth boundary tests. Transfer of flows to the outer bank occurred more rapidly for the rough boundary test and downstream shear stresses on the outer bank were considerably higher. Ippen *et al.* (1960) surmised that due to the increase in flow resistance, a greater portion of the flow experienced transverse motion due to radial pressure gradient which is consistent with a decrease in super-elevation from that of the corresponding smooth boundary test. Simulated double-bend tests illustrated an increase in outer bank shear stresses from that of uniform approach flow. Ippen *et al.* (1962) concluded that boundary shear stress patterns obtained cannot be predicted quantitatively from the gross characteristics of flow. A relationship between relative curvature and maximum relative shear stress was determined.

2.2.2.2 U. S. Bureau of Reclamation (1964)

The USBR (1964) reported shear stress and velocity distributions in a single trapezoidal bend in an effort to determine optimal channel cross sections to stabilize earthen canals. Shear stress distributions were found similar to that of Ippen *et al*. (1960, 1962), where the highest shear stresses occurred on the inside bank at the bend entrance and on the outside bank downstream of the bend exit. It was suggested that future studies should focus on greater degrees of curvature, larger bend angles, and bends with steeper banks that might affect boundary shear magnitude and distribution.

2.2.2.3 Yen (1965)

Yen (1965) examined shear stress, velocity, direction of flow, and turbulence intensity in a trapezoidal channel. Configuration setup was created to resemble curvature commonly found on the Mississippi and Missouri Rivers with a full meander where the second bend was the focus for measurements. Yen reported growth of the secondary current in the first bend strongly affected the proceeding bend due to a short reach between bends. Growth of the secondary current in the second bend accelerated the decay rate of secondary flow remnants from the previous bend. Decaying of secondary flow remnants was confined to the upper corner of the outside bank, which was found to hinder secondary growth of that bend. It was found that the secondary current decayed by half in the midsection of the straight reach and three quarters at the entrance to the second bend. Maximum shear stresses were found near the inner bank at the entrance to the bend and near the outer bank at the bend exit. Reported shear stress distributions were similar to that of Ippen *et al*. (1960, 1962). Yen hypothesized that shear stress on the inner bank was not the location of maximum scour due to stabilization resulting from secondary motion. It was further postulated that erosive forces on the outside bank downstream of the bend apex are more effective than the inner bank due to the shear acting in a downward direction.

2.2.2.4 Hooke (1975)

Hooke (1975) examined distributions of sediment transport, shear stress, and helical strength within a meander. Channel geometry was approximated using empirical relationships of naturally occurring meandering streams. Cross-sectional geometry was rectangular except in three tests where a rounded corner was molded between bed and banks creating a concave shape.

Helical strength was measured using a needle and thread technique, where the angular differences between the bottom flow and surface flow directions were considered a measure of strength of secondary flows. Hooke (1975) concluded that locations of the maximum sediment discharge per unit width and shear stress coincided. Maximum shear stress was located on the concave side of the upstream entrance, where it followed the channel centerline until just downstream of the bend where it followed the concave bank. Reported shear stress distributions were similar to that of Ippen *et al*. (1960, 1962), the USBR (1964), and Yen (1965). Hooke postulated that bed geometry is adjusted to provide the proper amount of shear stress to transport the sediment supply. By examination of the helical strength, Hooke (1975) determined that the secondary currents influence on bed geometry is "*often overstated*" and the sediment distribution is responsible for point bar development and not secondary currents. Hooke theorized, while referencing others, that sediment movement is not eroded on the outside bank and distributed to the inside bank by secondary currents but rather eroded on the outside bank of one bend and distributed to the point bar in the following bend.

2.2.2.5 Nouh and Townsend (1979)

Nouh and Townsend (1979) tested bend angles and resulting effects on scour development in single-bend tests to relate theoretical approximations to measured values. Maximum scour was observed near the outer channel wall of the bend exit section and was found to move further downstream as the bend angle increased. Deposition was noted by flow-visualization techniques on the inside of the bend, which was attributed to flow separation near the inner wall at the entrance to the bend.

2.2.2.6 Bathurst (1979)

Bathurst (1979) examined velocity distributions in British cobble-bed streams for both straight and curved reaches. Bathurst's (1979) study provides insight into cross-sectional variation in cobble-bed streams. It was found that the region of high shear stress lags behind the core of maximum velocity crossing the channel and secondary circulation encourages high-velocity surface flow but inhibits similar movement near the wall. Bathurst theorized that secondary circulation was strongest at medium discharges and, as a result, the cross-over region of high shear stress should lie further upstream than at low or high discharges. Accordingly, at

high discharges, the shear stress would move further from the outer bank and effects of secondary circulation would be weak compared to primary flows.

2.2.2.7 Tilston (2005)

Tilston (2005) investigated shear stress distributions by several methods in a reach of the Petite Barbue River in Quebec. Shear stress estimates were made by the von Kármán logarithmic law, drag coefficient, Reynolds stress, turbulent kinetic energy (TKE), and vertically-based turbulent kinetic energy (TKE w') methods. The latter two methods are oceanographic methods that were suggested by Biron *et al*. (2004) to be adequate in complex flows during tests in a laboratory flume. A distinction was made between steady and turbulent methods, where the logarithmic law and drag coefficient methods were considered steady and the Reynolds and TKE methods were considered turbulent. Tilston (2005) concluded that turbulence methods are more reliable because they account for velocity fluctuations which are responsible for sediment entrainment or movement. Of the turbulence methods, the TKE resulted in higher shear stresses in the zones of bank failure before they occurred. Furthermore, all of the methods were compared to locations in which sediment transport was noted. It was found that steady flow methods resulted in values that were less than that required for movement.

Tilston (2005) calculated turbulence intensities throughout the bend at various discharges and determined that intensities were greatest at the bend exit during low to medium flows and at the bend entrance during high flows. A non-linear relationship between turbulence intensities and velocities was noted. Shear stress distributions resulting from the TKE method illustrated high shear stresses at the channel centerline at the apex of the band and between the entrance and apex on the convex bank for low and medium discharges. Maximum shear stress at high discharges was located near the outer bank at the exit of the bend. Multiple pools were noted during the medium and low stages and a single large pool at the high stage. Locations of mass failure were attributed to a consistent low flow as the stream is controlled by an upstream dam. Tilston (2005) surmised that flow in the bend was controlled by topographic steering over the point bar, where flows are directed toward the upstream outer bank and then redirected to make contact with the exit outer bank region. Furthermore, low flows were suggested to cause knickpoints at the upstream and downstream outer bank locations, which lower the relative curvature with respect to the apex centerline. Knickpoints created at low flows were locations of

mass failure during bankfull conditions. Tilston (2005) proposed that channel migration is determined at low flows and meandering evolution occurs at high flows.

2.2.2.8 Sin (2010)

Sin (2010) examined shear stress distributions in a large-scale prismatic channel with two bends at Colorado State University's Engineering Research Center. Shear stresses were estimated by Preston tube, Reynolds stresses, law of the wall, and Rozovskii methods. Sin concluded the Preston tube provided most accurate approximations due to its ability to take direct measurements on the bed. Maximum shear stress in the bends was related to approach shear stresses estimated from a one-dimensional (1-D) numerical model and presented with findings by others. Equation 2.2 relating relative curvature to increases in shear stress is provided:

$$K_b = 3.2135 \times \left(\frac{R_c}{T_w} \right)^{-0.2657}$$ **Equation 2.2**

where

K_b = ratio of maximum shear stress and averaged shear stress in the approach [dimensionless];

R_c = radius of curvature [L]; and

T_w = top width of the channel [L].

2.2.3 Design Guidelines

Design guidelines have been developed by the Federal Highway Administration (FHWA) and the U. S. Army Corps of Engineers (USACE) to assist in design of protection measures based on data collected in aforementioned studies. Guidelines are presented in the following subsections.

2.2.3.1 U. S. Army Corp of Engineers (1970)

The USACE (1970) outline a general guideline for expected increases in shear stress based on studies conducted by Ippen *et al.* (1960, 1962), the USBR (1964), and Yen (1965). Distributions of expected increase in shear stress were given in graphical form as illustrated in

Figure 2.9, which presents locations where a designer should increase riprap protection measures. Increases in D_{50} and riprap blanket thickness are suggested in areas of expected high shear. The USACE (1970) notes use of Figure 2.9 should be limited to trapezoidal shaped 60º bends or natural channels with similar attributes.
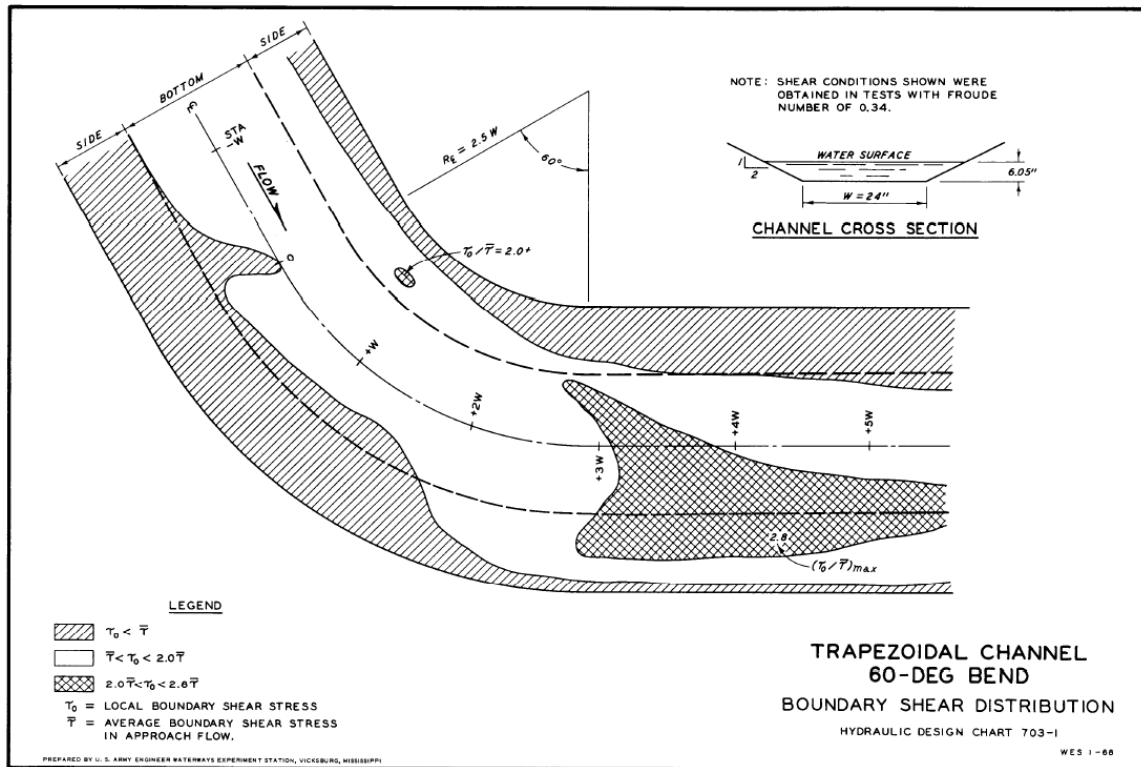
Figure 2.9: Reference for Expected Shear Stress Increase in Bends (USACE 1970)

2.2.3.2 Federal Highway Administration (2005)

The FHWA (2005) gives guidance for a shear stress multiplier around a bend in the *Hydraulic Engineering Circular No. 15* (*HEC-15*). It is stated that shear stress is affected by secondary currents and that maximums are found near the inside entrance of a bend and on the outside of the bend toward the bend exit where it persists further downstream as seen in Figure 2.10. The FHWA (2005) provides Equation 2.3 for utilizing the shear stress multiplier and Equation 2.4 developed by Young *et al.* (1996) based on Lane (1955) in determining the multiplier:

$$\tau_b = K_b \tau_d \qquad \qquad \textbf{Equation 2.3}$$

where

τ_b = side shear stress on the channel [$ML^{-1}T^{-2}$];

K_b = ratio of channel bend to bottom shear stress [dimensionless]; and

τ_d = shear stress in channel at maximum depth [$ML^{-1}T^{-2}$].

$$K_b = 2.00 \qquad \qquad \left(\frac{R_c}{T_w}\right) \leq 2$$

$$K_b = 2.38 - 0.206\left(\frac{R_c}{T_w}\right) + 0.0073\left(\frac{R_c}{T_w}\right)^2 \qquad 2 < \left(\frac{R_c}{T_w}\right) < 10 \qquad \textbf{Equation 2.4}$$

$$K_b = 1.05 \qquad \qquad 10 \leq \left(\frac{R_c}{T_w}\right)$$

where

K_b = ratio of channel bend to bottom shear stress [dimensionless];

R_c = radius of curvature [L]; and

T_w = top width of the channel [L].
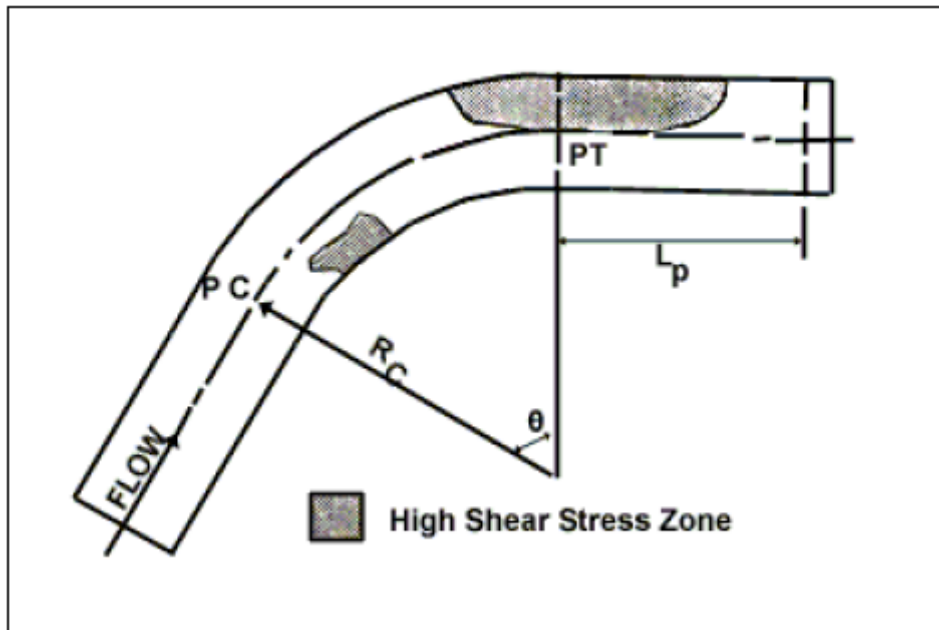
Figure 2.10: Locations of High Shear Stress (Nouh and Townsend 1979)

2.3 Shear Stress Computation Methods

Determining shear stress in bends is difficult due to the presence of secondary circulation and resulting complex flow fields. Some of the more common methods for determining shear stress may not be applicable in bends due to assumptions made in derivation. Methods for estimating shear stress considered for this study are presented with underlying assumptions and instances applied in complex flow fields.

2.3.1 Reach-averaged Shear Stress

Reach-averaged boundary shear stress estimates are common for open-channel flow studies. Programs such as the Hydrologic Engineering Center's River System Analysis (HEC-RAS), commonly used in practice (Gordon *et al.* 2004), calculates reach-averaged boundary shear stress estimates (USACE 2008). Henderson (1966), as well as other textbooks, provide derivations of shear stress based on momentum principles resulting in Equation 2.5:

$$\tau_o = \gamma R_h S_f \qquad\qquad \textbf{Equation 2.5}$$

where

$\tau_o = \tau_{zx} =$ boundary shear stress [$ML^{-1}T^{-2}$];

$\gamma =$ specific weight of the fluid [$ML^{-2}T^{-2}$];

$R_h =$ hydraulic radius; and

$S_f =$ friction slope [dimensionless].

A summary of assumptions in the derivation of Equation 2.5 follows (Henderson 1966, USACE 2008, Finnemore and Franzini 2002, Gates 2008):

- one-dimensional flow;
- steady flow;
- bed and bank shear are equal;
- velocity coefficients are constant over the reach;
- shear along the water surface is negligible; and
- small channel slope ($\tan\theta \approx \sin\theta$).

If further assuming steady uniform flow, the friction slope (S_f) can be assumed equal to the water-surface slope (S_w) as well as the bed slope (S_o) (Henderson 1966, Julien 1998).

HEC-RAS uses a standard step backwater calculation procedure for steady flow simulations to determine cross-sectional averaged properties of flow. Friction slopes are computed at each cross section by Equation 2.6 and boundary shear stress by Equation 2.5 for steady flow simulations (USACE 2008):

$$S_f = \left(\frac{Q}{K}\right)^2 \qquad \textbf{Equation 2.6}$$

where

S_f = friction slope or slope of the energy grade line [dimensionless];

Q = total flow rate [L^3T^{-1}]; and

K = total conveyance of cross section [L^3T^{-1}].

Nezu and Nakagawa (1993) note that the accuracy of this method is dependent on the amount of cross-sectional data available so that small deflections in the bed and water surface can be determined. Use of this model in determining shear stress in bends is unfounded due to the 1-D flow assumption, and because of its wide use, provides purpose for this study.

2.3.2 Law of the Wall

The von Kármán-Prandtl universal logarithmic law, or 'law of the wall' as it is commonly referred, is a method frequently used for estimating local shear stress in 1-D steady uniform flow. The law is derived from Prandtl's mixing length theory that describes shearing stresses as related to a characteristic length of transverse momentum exchange. Equation 2.7 describes the mixing length theory for developed turbulent flow over a solid boundary (Chow 1959):

$$\tau_{zx} = \rho \cdot l_m{}^2 \left(\frac{dv_x}{dy}\right)^2 \qquad \textbf{Equation 2.7}$$

where

τ_{zx} = shear stress acting on the z plane in the x direction [$ML^{-1}T^{-2}$];

ρ = mass density [ML^{-3}];

l_m = mixing length [L]; and

$$\left(\frac{dv_x}{dy}\right) = \text{velocity gradient at a normal distance } y \text{ from the solid surface.}$$

Prandtl assumed that in the near-bed region, mixing length is proportional to the distance from the bed and shear stress is constant. The law of the wall was derived based on Prandtl's assumptions by von Kármán who quantified the mixing length and the distance from the boundary. Equation 2.8 presents the universal form of the law of the wall and Equation 2.9 gives the relationship between shear velocity and shear stress:

$$\frac{v_x}{u_*} = \frac{1}{k}\ln\left(\frac{y}{y_o}\right)$$

Equation 2.8

where

v_x = velocity in the stream-wise direction $[LT^{-1}]$;

u_* = shear velocity $[LT^{-1}]$;

k = proportionality constant [dimensionless];

y = distance from the boundary [L]; and

y_o = zero velocity roughness height [L].

$$\tau_o = \rho u_*^{\,2}$$

Equation 2.9

where

τ_o = bed shear stress $[ML^{-1}T^{-2}]$;

ρ = fluid density $[ML^{-3}]$; and

u_* = shear velocity $[LT^{-1}]$.

The proportionality constant between the mixing length and the distance from the boundary is known as the von Kármán constant, which is approximately equal to 0.4 (Chow 1959, Julien 1998, Montes 1998). Several studies have been conducted to test the value of the von Kármán constant suggesting a more refined value of 0.41 (Nezu and Nakagawa 1993). The zero velocity roughness height (y_o) is related to the boundary and can be determined by either a smooth and rough boundary where y_o is approximated as the flat boundary or by $k_s'/30$, where k_s' is the grain roughness height. Boundary classification can be determined by the grain shear Reynolds number (Re_*), or by comparison of the grain size (d_s) to the height of the laminar

sublayer (δ). Equation 2.10 presents the grain shear Reynolds number. The laminar sublayer is the region above the bed that is dominated by viscous effects and is approximated by Equation 2.11 (Julien 1998):

$$Re_* = \frac{u_* d_s}{v}$$

Equation 2.10

where

      Re_* =   grain shear Reynolds number [dimensionless];

      u_* =   shear velocity [LT^{-1}];

      d_s =   grain size [L]; and

      v =   kinematic viscosity [L^{2}T^{-1}].

$$\delta = \frac{11.6v}{u_*}$$

Equation 2.11

where

      δ =   height of the laminar sublayer [L];

      v =   kinematic viscosity [L^{2}T^{-1}]; and

      u_* =   shear velocity [LT^{-1}].

Julien (1998) notes that grain-size classifications of gravel or cobble and larger are considered hydraulically rough. A summary of the classification criteria is presented in Figure 2.11.
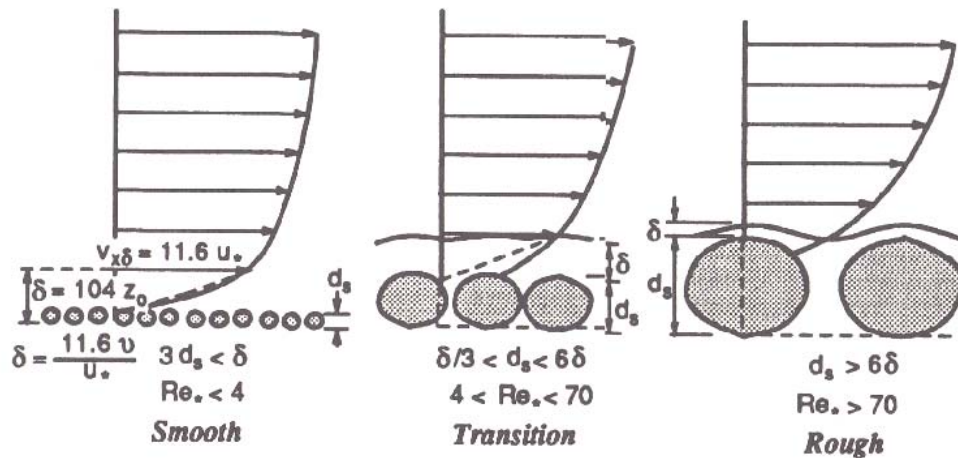
Figure 2.11: Boundary Classifications (Julien 1998)

26

Vertical velocity profiles can be divided into three regions: 1) the viscous or laminar sublayer, 2) the log layer, and 3) a defect layer where velocities are less likely to adhere to the law of the wall (Wilcox 2007). Figure 2.12 illustrates each region of the velocity profile. The log layer has generally been accepted as being below a relative depth (y/h) of 0.2 (Cardoso *et al.* 1989, Nezu and Nakagawa 1993, Biron *et al.* 1998, Afzalimehr and Anctil 2000, Song and Graf 1994) although some have found profiles are not strictly limited to this relative depth, especially in variable flow conditions (Baird 2004, Montes 1998, Afzalimehr and Rennie 2009). Departure from the logarithmic profile in the defect layer is due to invalidity of the constant shear stress and mixing length assumptions (Julien 1998). Coles (1956) defined a wake flow function that can be used to describe the defect layer.
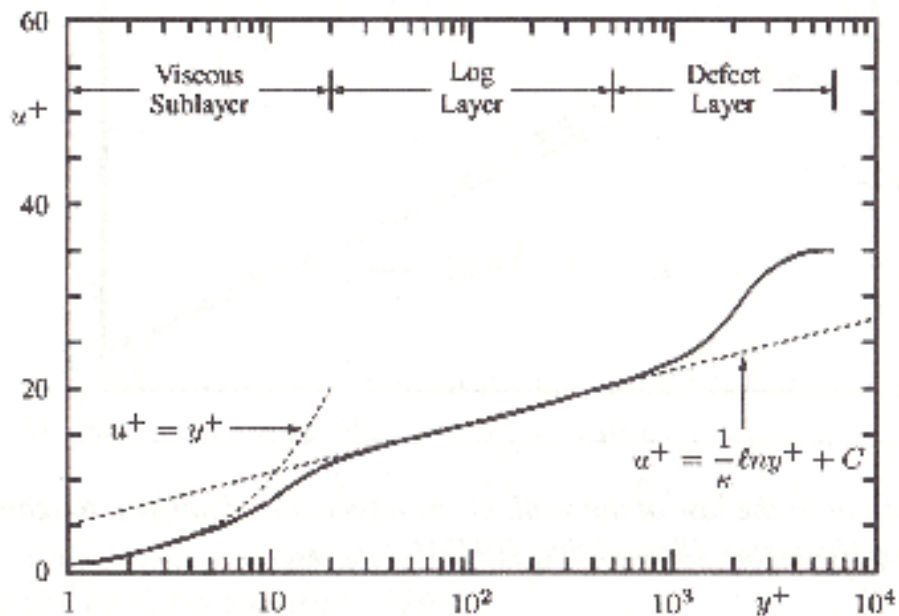
Figure 2.12: Regions Identified in the Velocity Profile Where $u^+ = v_x/u_*$ and $y^+ = u_* y/v$ (Wilcox 2007)

Researchers disagree with the applicability of the law of the wall in the presence of secondary or complex flows. Brown (1988) found that velocities deviated from a logarithmic profile especially in the upper portion of the flow in a study of shear stress distribution in bends. Wang and Cheng (2005) determined that the logarithmic law would generate misleading results in the presence of secondary flows due to deviations from the logarithmic profile. Biron *et al.* (2004) and Tilston (2005) also recognize deviations from the logarithmic profile in complex

flows. Knight and Shiono (1990) and Yen (1965) suggest deviations from the law of the wall occur when lateral Reynolds stresses (τ_{yx}) are not negligible and the vertical distribution of τ_{zx} is non linear. Alternatively, Nouh and Townsend (1979) found the method useful in examining the influence of secondary currents in downstream straight sections following bends at various angles. They concluded that the logarithmic profile, with variable von Kármán constants, was suitable for their study because longitudinal profiles of the stable sand bed parallel to the channel walls were smooth. Nouh and Townsend (1979) confirmed this assumption by examining differences between computed and measured profiles. Bathurst (1979) used the law of the wall to determine distributions of boundary shear stress in gravel-bed bends. They concluded that even though the law of the wall strictly applies to two-dimensional (2-D) flows, it can be applied reasonably well in the presence of secondary circulation if the bottom 10 to 15% of the flow is used. Furthermore, Afzalimehr *et al*. (2006), in an examination of flow resistance in a compound gravel-bed bend, found the law of the wall can be valid with a range of applicability in the vertical not limited to a relative depth less than 0.2. In addition to disagreement with applicability in complex flows, inherent uncertainty in determining the beginning and ending points of applicable data contribute to estimation errors (Afzalimehr and Rennie 2009, Kendall and Koochesfahani 2008, Biron *et al*. 1998).

2.3.3 Preston Tube

The Preston tube, properly named for Preston (1954), allows for direct local boundary shear stress measurements. The method employs a Pitot tube coupled with a static pressure tap to measure differential pressure near the bed and relates these measurements to boundary layer principles. From boundary layer principles, the velocity profile in the viscous sublayer over a smooth boundary can be represented by Equation 2.12 and then expressed by Equation 2.13 outside of the viscous sublayer, while remaining close to the wall (Ludweig and Tillman 1950):

$$\frac{v_x}{u_*} = f\left(\frac{yu_*}{v}\right)$$

Equation 2.12

$$\frac{v_x}{u_*} = 5.75\log\left(\frac{y}{y_o}\right)$$

Equation 2.13

where

v_x = velocity in the primary direction of flow [LT^{-1}];

u_* = shear velocity [LT^{-1}];

y = height above the bed [L];

v = kinematic viscosity [L^{2}T^{-1}]; and

y_o = zero velocity height [L].

From Equation 2.12, Preston (1954) reasoned that the shear stress (τ_o), fluid density (ρ), and kinematic viscosity (v) are independent variables and the pressure differential is dependent giving the relationship presented in Equation 2.14:

$$\frac{(P - p_o)d^2}{\rho v^2} = f\left(\frac{\tau_o d^2}{\rho v^2}\right)$$

Equation 2.14

where

P = total pressure [ML^{-1}T^{-2}];

p_o = static pressure [ML^{-1}T^{-2}];

d = diameter of Pitot tube [L];

ρ = fluid density [ML^{-3}];

v = kinematic viscosity of fluid [L^{2}T^{-1}]; and

τ_o = bed shear stress [ML^{-1}T^{-2}].

In comparing results, Preston determined Equation 2.15 accommodated for differing Pitot tube measurements. Preston surmised that Equation 2.15 could be used to determine boundary shear stress for rough or smooth boundaries as long as the roughness height is small compared to the least Pitot diameter:

$$\frac{(P - p_o)d^2}{4\rho v^2} = f\left(\frac{\tau_o d^2}{4\rho v^2}\right)$$

Equation 2.15

where

P = total pressure [ML^{-1}T^{-2}];

p_o = static pressure [ML^{-1}T^{-2}];

d = diameter of Pitot tube [L];

ρ = fluid density [ML^{-3}];

v = kinematic viscosity of fluid [L^{2}T^{-1}]; and

τ_o = bed shear stress [ML^{-1}T^{-2}].

Finally, in determining a fit to measurements of all Pitot diameters, Equation 2.16 was determined accurate for a defined range presented in Equation 2.17:

$$\log_{10} \frac{\tau_o d^2}{4\rho v^2} = -1.396 + \frac{7}{8} \log_{10}\left(\frac{(P - p_o)d^2}{4\rho v^2}\right) \qquad \textbf{Equation 2.16}$$

$$4.5 < \log_{10}\left(\frac{(P - p_o)d^2}{4\rho v^2}\right) < 6.5 \qquad \textbf{Equation 2.17}$$

where

τ_o = bed shear stress [ML^{-1}T^{-2}];

d = diameter of Pitot tube [L];

ρ = fluid density [ML^{-3}];

v = kinematic viscosity of fluid [L^{2}T^{-1}];

P = total pressure [ML^{-1}T^{-2}]; and

p_o = static pressure [ML^{-1}T^{-2}].

Equation 2.16 has been confirmed by others for the following ranges (Ackerman *et al.* 1994, Ackerman and Hoover 2001):

$$4.0 < \log_{10} \frac{\tau_o d^2}{4\rho v^2} < 6.5 \quad \text{and} \quad 2.0 < \log_{10}\left(\frac{(P - p_o)d^2}{4\rho v^2}\right) < 4.2$$

where

τ_o = bed shear stress [ML^{-1}T^{-2}];

d = diameter of Pitot tube [L];

ρ = fluid density [ML^{-3}];

v = kinematic viscosity of fluid [L^{2}T^{-1}];

P = total pressure [ML^{-1}T^{-2}]; and

p_o = static pressure [ML^{-1}T^{-2}].

Preston (1954) notes that the following criteria must be met for accurate results:

- The Pitot diameter must be small compared with pipe diameter.

- The outside diameter of the Pitot must be larger than the roughness height.

- Errors due to displacement of the effective center of the Pitot tube are small enough to be ignored.

- If applied to rough boundaries, the viscosity is assumed to dominate flow at the wall.

Ackerman and Hoover (2001) expand on requirements that should be met by suggesting the pressure differences must be large and the static pressure must be measured close to the Pitot tube and assumed constant. Hsu (1955) confirms the validity of Equation 2.16 but alternatively suggests that the ratio of the inner and outer Pitot tube diameters has a negligible effect.

Hwang and Laursen (1963) determined a relationship for the Preston tube in the presence of hydraulically rough boundaries. The derived relationship relates change in pressure to boundary shear stress based on Equation 2.13, where y_o for a rough boundary can be approximated by $k_s'/30$, where k_s' is the grain roughness height. Hwang and Laursen (1963) concluded from tests conducted over rough sand boundaries that correction factors were needed depending on grain roughness height. It was noted that difficulty with this procedure is determining the zero velocity height:

$$\frac{P-p_o}{\tau_o} = 16.531 \left\{ \begin{array}{l} \left[\log\frac{30h_c}{k_s}\right]^2 - \log\frac{30h_c}{k_s}\left[0.25\left(\frac{a}{h_c}\right)^2 + 0.0833\left(\frac{a}{h_c}\right)^4 + 0.00704\left(\frac{a}{h_c}\right)^6 + ...\right] + \\ \left[0.25\left(\frac{a}{h_c}\right)^2 + 0.1146\left(\frac{a}{h_c}\right)^4 + 0.0586\left(\frac{a}{h_c}\right)^6 + ...\right] \end{array} \right\}$$

Equation 2.18

where

P = total pressure [$ML^{-1}T^{-2}$];

p_o = static pressure [$ML^{-1}T^{-2}$];

τ_o = bed shear stress [$ML^{-1}T^{-2}$];

h_c = height of center of stagnation tube from the zero datum (z_o) [L];

k_s = sand roughness height [L]; and

a = inner radius of the stagnation tube [L].

Ghosh and Roy (1970) used the Preston tube to determine boundary shear stress in compound channels with hydraulically smooth and rough boundaries. They determined that the use of the inner law (Equation 2.12) was inappropriate for their situation due to unsteadiness and non-uniformity of the mean flow and adopted Hwang and Laursen's (1963) derivation technique. Accordingly, Ghosh and Roy (1970) concluded that the derived relationship presented in

Equation 2.19 was valid due to a reasonable relationship between shear velocities calculated and approximated discharge:

$$\frac{(P - p_o)}{\tau_o} = 16.531 \left\{ \begin{array}{l} \log\left(\dfrac{9u_* h_c}{v}\right)^2 - \ln\left(\log\left(\dfrac{9u_* h_c}{v}\right)\right) \\[2ex] \left[0.25(r/h_c)^2 + 0.0625(r/h_c)^4 + 0.026(r/h_c)^6 + ...\right] \\[2ex] + \ln^2\left[0.25(r/h_c)^2 + 0.1146(r/h_c)^4 + 0.0594(r/h_c)^6 + ...\right] \end{array} \right\}$$

Equation 2.19

where

P = total pressure $[ML^{-1}T^{-2}]$;

p_o = static pressure $[ML^{-1}T^{-2}]$;

τ_o = bed shear stress $[ML^{-1}T^{-2}]$;

u_* = shear velocity $[LT^{-1}]$;

h_c = height of the center of stagnation tube from the zero datum (z_o) $[L]$;

v = kinematic viscosity of fluid $[L^2T^{-1}]$; and

r = inner radius of the stagnation tube $[L]$.

Ghosh and Roy (1970) note that determining the zero velocity height (y_o) is problematic in cases where the roughness distribution is not uniform.

Ippen *et al*. (1960) used the Preston tube to determine boundary shear stress in trapezoidal bends for smooth and rough boundaries. Pressure differences for the hydraulically smooth condition were related to shear stress by way of Equation 2.16 empirically derived by Preston (1954). For the rough boundary condition where the inner law is invalid, Ippen *et al*. (1960) calibrated the Preston tube based on momentum principles in a straight flume where the flow is essentially two dimensional. They determined that for fully-developed turbulent flow over a rough boundary, there is a linear relationship between shear stress, flow depth, and pressure differential as presented in Equation 2.20. A coefficient was determined by best-fit regression:

$$\frac{v_x}{u_*} = f\left(\frac{y}{k_s'}\right)$$

Equation 2.20

where

v_x = velocity in the primary direction of flow [LT^{-1}];

u_* = shear velocity [LT^{-1}];

y = height above the bed [L]; and

k_s' = grain roughness height [L].

Ippen *et al.* (1960) suggest that error is introduced in a rough boundary condition due to surface irregularities causing placement errors or shielding effects from the flow. In an attempt to prevent errors caused by individual roughness elements, a sleeve was placed over the Pitot as illustrated in Figure 2.13.
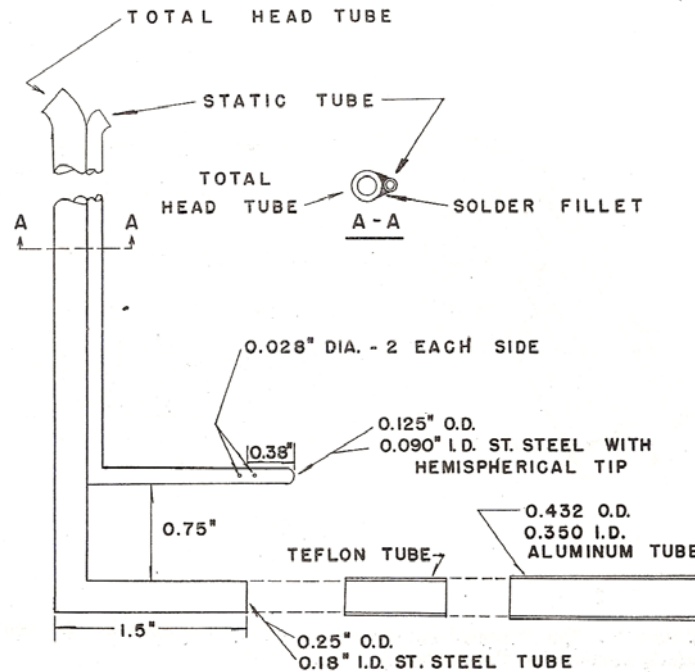
Figure 2.13: Adjustment for Rough Boundary (Ippen *et al.* 1962)

Ippen *et al.* (1960) determined a maximum probable error of 7% for their smooth boundary test by estimating error associated with each of the dependent parameters. Rough boundary error was estimated to be 15%, which was determined from fluctuations in calibration measurements. They attributed most of the error to local variations in velocity distribution and tube orientation. Error in misalignment with the flow was stated as varying by (1-cosθ), where θ is the misalignment angle. A 15° misalignment angle was found to result in 3.4% error during

tests in a straight flume. In concluding remarks, Ippen *et al*. (1960) state that the Preston tube was successfully adapted for smooth as well as rough boundary surfaces in fluvial systems.

The USBR (1964) used a Preston tube in determining shear stress in a trapezoidal bend and used the calibration proposed by Preston (1954). Yen (1965) also used a Preston tube in a trapezoidal bend to determine shear stress distributions. Yen (1965) calibrated the Preston tube for a carefully finished cement-mortar surface and found the calibration to be similar to Preston's (1954) and Hsu's (1955) curve with percent differences of 5.5% and 1.3%, respectively. Alternatively to that of Ippen *et al*. (1960), Yen (1965) used a thread mounted on a needle attached to the probe to determine the direction of flow. The Preston tube was then oriented in that direction for measurements. Brown (1988) also oriented with the direction of flow in using a Preston tube to measure boundary shear stress in a natural topographic setting. The calibration for the Preston tube was based upon the equations of motion as related to the pressure differential measured by the Preston tube, which is similar to Ippen *et al*.'s (1960) calibration for the rough boundary tests.

Preston tubes have been used in meandering bends with rough and smooth boundaries. Measurement errors associated with alignment are small, which provides versatility as the attack angle of flow in bends varies as transverse flow increase in strength due to radial acceleration. Preston tubes also provide the ability to take direct measurements on the bed providing simplicity and ease of use.

2.3.4 Reynolds Stresses

Flow in open channels can be classified into two modes of transport: 1) laminar and 2) turbulent. Laminar flow is described as being unidirectional with low velocities and flow layers sliding one above the other. Turbulent flow is classified as having irregular fluctuations in the transversal and longitudinal directions. The distinction between these two flows was described by Osborne Reynolds in flow-visualization studies in the late 1800s. Reynolds determined that the instantaneous velocities are composed of a mean value plus a fluctuating component as shown in Equation 2.21, Equation 2.22, and Equation 2.23 (Montes, 1998):

$$x = \bar{x} + x'$$
<div align="right">**Equation 2.21**</div>

$$y = \bar{y} + y'$$
<div align="right">**Equation 2.22**</div>

$$z = \bar{z} + z'$$ **Equation 2.23**

The x, y, and z directions of the Cartesian coordinate system correspond to the downstream, transverse, and vertical directions, respectively.

In inserting Reynolds theory into the Navier Stokes Equations, the Reynolds stresses can be obtained from the convective acceleration terms (Julien 1998). Equation 2.24 gives the relationship between covariances of velocity fluctuations and shear stress components and Figure 2.14 provides an example of the stress components acting on a fluid body. A thorough derivation of Equation 2.24 is provided by Schlichting (1968):

$$\begin{pmatrix} \sigma_x & \tau_{xy} & \tau_{xz} \\ \tau_{xy} & \sigma_y & \tau_{yz} \\ \tau_{xz} & \tau_{yz} & \sigma_z \end{pmatrix} = -\rho \begin{pmatrix} \overline{u'u'} & \overline{u'v'} & \overline{u'w'} \\ \overline{u'v'} & \overline{v'v'} & \overline{v'w'} \\ \overline{u'w'} & \overline{v'w'} & \overline{w'w'} \end{pmatrix}$$ **Equation 2.24**

where

σ_i = normal force acting on the i plane [$ML^{-1}T^{-2}$];

τ_{ij} = shear stress acting on the i plane in the j direction [$ML^{-1}T^{-2}$];

x = stream-wise flow direction;

y = transverse flow direction;

z = vertical flow direction;

ρ = fluid density;

$\overline{u'w'} = \overline{w'u'}$ = covariance of velocity fluctuations in the stream-wise and vertical flow directions [L^2T^{-2}];

$\overline{u'v'} = \overline{v'u'}$ = covariance of velocity fluctuations in the stream-wise and transverse flow directions [L^2T^{-2}]; and

$\overline{w'v'} = \overline{v'w'}$ = covariance of velocity fluctuations in the transverse and vertical flow directions [L^2T^{-2}].
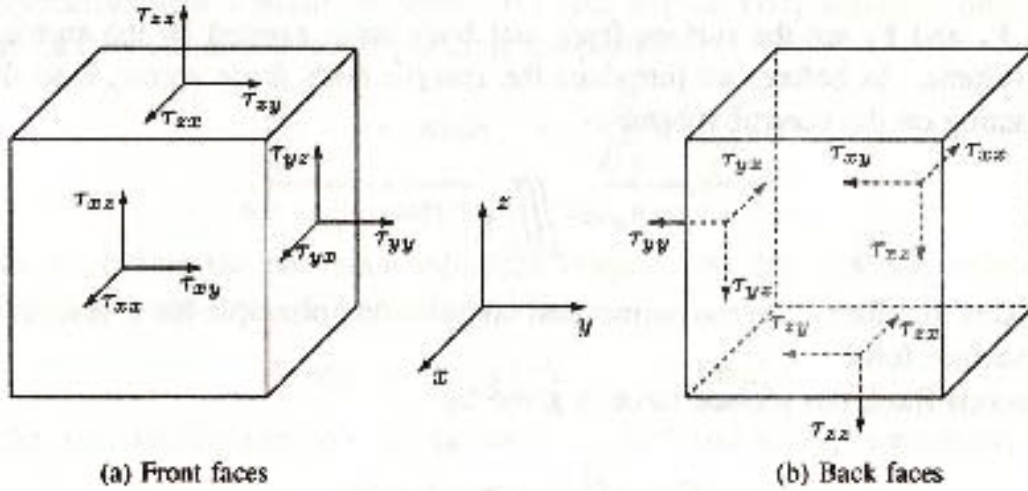
Figure 2.14: Stresses Acting on a Fluid Body (Wilcox 2007)

From symmetry, stress components are related as seen in Equation 2.25, Equation 2.26, and Equation 2.27:

$$\tau_{xz} = \tau_{zx}$$

Equation 2.25

$$\tau_{xy} = \tau_{yx}$$

Equation 2.26

$$\tau_{yz} = \tau_{zy}$$

Equation 2.27

where

τ_{xz} = shear stress acting on the x plane in the z direction [ML^{-1}T^{-2}];

τ_{zx} = shear stress acting on the z plane in the x direction [ML^{-1}T^{-2}];

τ_{xy} = shear stress acting on the x plane in the y direction [ML^{-1}T^{-2}];

τ_{yx} = shear stress acting on the y plane in the x direction [ML^{-1}T^{-2}];

τ_{yz} = shear stress acting on the y plane in the z direction [ML^{-1}T^{-2}]; and

τ_{zy} = shear stress acting on the z plane in the y direction [ML^{-1}T^{-2}].

The normal stresses (σ) in Equation 2.24 are external forces working on the fluid volume (Hinze 1959).

In considering 2-D flow (downstream and vertical), Equation 2.28 can be obtained from the Navier-Stokes Equations (Montes 1998):

$$\tau = \mu\left(\frac{\partial \bar{u}}{\partial y} + \frac{\partial \bar{w}}{\partial x}\right) - \rho\overline{u'w'}$$

Equation 2.28

where

τ = shear stress [$ML^{-1}T^{-2}$];

μ = dynamic viscosity [$ML^{-1}T^{-1}$];

$\bar{u}$ = average velocity in the stream-wise direction [LT^{-1}];

y = transverse flow direction;

$\bar{w}$ = average velocity in the vertical direction [LT^{-1}];

x = downstream flow direction;

ρ = mass density of water [ML^{-3}]; and

$\overline{u'w'}$ = covariance of velocity fluctuations in the stream-wise and vertical flow directions [L^2T^{-2}].

The second term in Equation 2.28 is known as the Reynolds stress and is much greater than the viscous shear stress except in the immediate wall region (Montes 1998, Wilcox 2007). Reynolds stresses are seen to act as an apparent shear stress as suggested by Boussinesq who made the assumption that viscous stresses act like turbulent stresses and are directly proportional to the velocity gradient (Hinze 1959, Montes 1998). Figure 2.15 presents a depiction on the theoretical basis between Reynolds and viscous stresses from measured data.
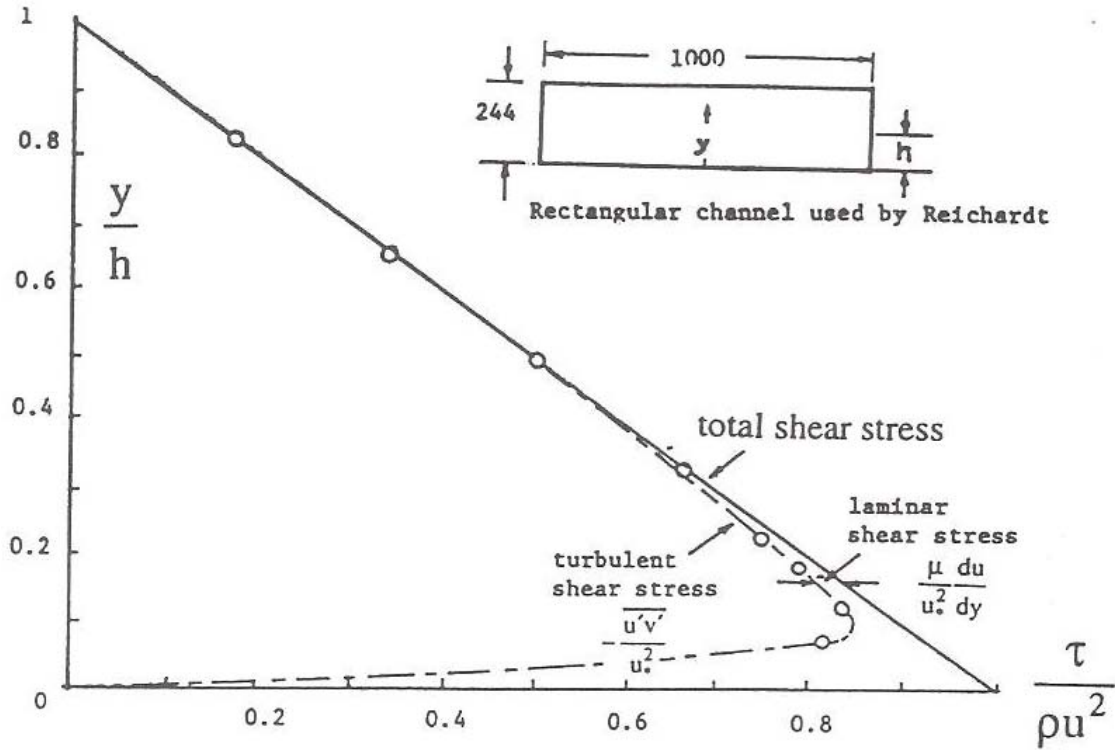
Figure 2.15: Theoretical Relationship between Reynolds and Viscous Stresses (Montes 1998)

Dey and Lambert (2005) give the theoretical relationship between Reynolds stress and bed shear stress for 2-D non-uniform unsteady flow as presented in Equation 2.29:

$$\tau = -\rho \overline{u'w'} = \tau\big|_{y=a} f(\eta, t)$$ **Equation 2.29**

where

τ = Reynolds stress [ML^{-1}T^{-2}];

ρ = mass density [ML^{-3}];

$\overline{u'w'}$ = covariance of velocity fluctuations in the stream-wise and vertical flow directions [L^{2}T^{-2}];

$\tau\big|_{y=a}$ = bed shear stress [ML^{-1}T^{-2}], where y = height above the bed [L] and a = zero-velocity height equal to $0.033\,k_s'$ (where k_s' = equivalent roughness height of Nikudurse);

η = y/h [dimensionless], where h = flow depth [L]; and

t = time [T].

Extrapolating the Reynolds stress to the bed to determine bed shear stress, as seen in Figure 2.15, has been viewed by some as the most appropriate method for estimating shear stress in 2-D flows (Nikora and Goring 2000, Nezu and Nakagawa 1993, Graf and Song 1995) but note that it is sensitive to deviations from 2-D flows (Nezu and Nakagawa 1993). Also, sensor misalignment has been found to skew resulting shear stresses (Roy *et al*. 1996). Roy *et al*. (1996) provide methods for data rotation. Song (1994) found that deviations from the linear distribution occurred in accelerating and decelerating flows with concave and convex profiles, respectively. Shiono and Muto (1998) found that the Reynolds stress can be negative in the upper portion of the profile when secondary currents are present. Nikora and Goring (2000) noted slight deviations from linearity near the free surface which were attributed to being either near surface effects, deviations from uniform flow, or effects from weak secondary currents.

An alternative to extrapolating Reynolds stress to the bed, is the use of a single near-bed point measurement (Biron *et al*. 2004, Heathershaw 1979). Biron *et al*. (2004) propose the use of a near-bed measurement located at the maximum of the Reynolds stress profile. They determined for their study that the maximum was located at a relative depth (*y/h*) of 0.1 for rough and smooth boundaries but gave caution to the use of this value because of its possible relation to variations in instrumentation. Biron *et al*. (2004) further note that extrapolating to the bed should be done when profile measurements are available because it provides a good estimate of the expected increase in bed shear stress with bed roughness.

Shear stress estimates by Reynolds stresses have been determined in cases where 1-D flows were not assumed thereby incorporating a stress component acting in the transverse direction. Huthnance *et al*. (2002) determined bed shear stress in an oceanographic study utilizing velocity fluctuations acting on the vertical plane in the downstream and transverse directions as seen in Equation 2.30. It was noted that the method is highly sensitive to measurement of vertical velocity fluctuations but was more reliable than the logarithmic distribution. Tilston (2005) used the method in a meandering bend but cautioned results may be misleading as the resulting magnitude accommodates stresses acting in a direction opposite that of the primary:

$$\tau = \rho(\overline{u'w'}^2 + \overline{v'w'}^2)^{1/2} \qquad \qquad \textbf{Equation 2.30}$$

where

τ = shear stress [ML^{-1}T^{-2}];

ρ = mass density [ML^{-3}];

$\overline{u'w'}$ = covariance of velocity fluctuations in the stream-wise and vertical flow directions [L^{2}T^{-2}]; and

$\overline{v'w'}$ = covariance of velocity fluctuations in the transverse and vertical flow directions [L^{2}T^{-2}].

Dey and Barbhuiya (2005) used a combination of Reynolds stresses in determining bed shear near a vertical-wall abutment for pre- and post-scour conditions. Bed shear stress was determined by Equation 2.31 or Equation 2.32, depending on the location near the abutment as presented in Figure 2.16. Equation 2.31 was used to determine boundary shear stress for Sections A, B, and F and Equation 2.32 for Sections C, D, and E (Dey and Barbhuiya 2005):

$$\tau_o = \sqrt{\tau_y^2 + (\tau_x \cos\phi_b + \tau_z \sin\phi_b)^2} \qquad \textbf{Equation 2.31}$$

$$\tau_o = \sqrt{\tau_x^2 + (\tau_y \cos\phi_b + \tau_z \sin\phi_b)^2} \qquad \textbf{Equation 2.32}$$

where

τ_o = bed shear stress [ML^{-1}T^{-2}];

τ_y = $-\rho(\overline{u'v'} + \overline{w'v'})$ [ML^{-1}T^{-2}], where ρ = mass density of water;

τ_x = $-\rho(\overline{w'u'} + \overline{v'u'})$ [ML^{-1}T^{-2}];

τ_z = $-\rho(\overline{u'w'} + \overline{v'w'})$ [ML^{-1}T^{-2}]; and

ϕ_b = local angle of the scoured bed with the horizontal (equals 0 for plane bed) (°).
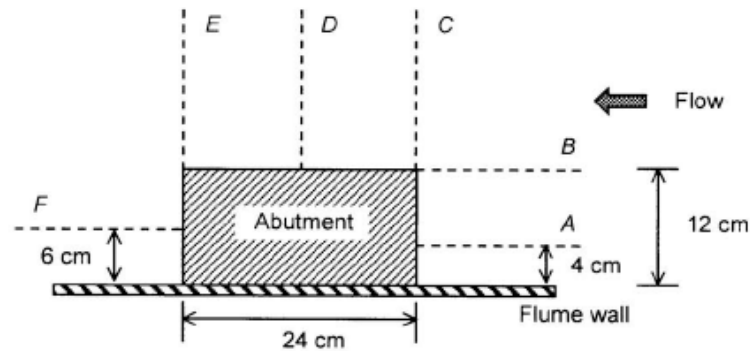
Figure 2.16: Measurement Sections around Abutment (Dey and Barbhuiya 2005)

40

Although it is not explicitly stated, it appears that Dey and Barbhuiya (2005) used a single near-bed measurement for bed shear stress determination. Duan (2009) used the same principle as that of Dey and Barbhuiya (2005) in a similar straight-flume flat-bed experimental study with a dike in the flow field. Assuming a flat bed reduces Equation 2.32 to Equation 2.33:

$$\tau_o = \sqrt{(\tau_b^x)^2 + (\tau_b^y)^2}$$ **Equation 2.33**

where

τ_o = bed shear stress [ML^{-1}T^{-2}];

τ_b^x = $-\rho(\overline{w'u'} + \overline{v'u'})\big|_{bed}$ [ML^{-1}T^{-2}], where ρ = mass density of water [ML^{-3}]; and

τ_b^y = $-\rho(\overline{w'v'} + \overline{u'v'})\big|_{bed}$ [ML^{-1}T^{-2}].

Reynolds stress distributions have been examined in river bends by many researchers. Anwar (1986), in an examination of Reynolds stresses in a river bend, found maximum values of lateral Reynolds shear stresses occurred near the outer bank at the bend entrance, where it increased through the bend and decreased at the bend exit. Reynolds shear stress distributions in each cross section were given with respect to maximum velocity. Shiono and Muto (1998) examined complex flow mechanisms in compound meandering channels with overbank flow and determined that the Reynolds stress $-\overline{v'w'}$ can reach values that are three to four times greater than $-\overline{u'w'}$ in the lower layer when strong secondary currents are present. Blanckaert and Graf (2001) examined the three turbulent components in flow through a bend at a location 60º from the bend entrance. Reynolds shear stress components were normalized based on straight uniform flow approximations and isocontours are given for cross-sectional variations. Blanckaert and Graf (2001) were able to extrapolate the cross-stream component acting on the horizontal plane $(-\rho\overline{u'v'})$ to the bank but found the component only attributed approximately 35% of the total shear given by a straight uniform flow approximation on the bank. They concluded that the turbulent stress components $-\rho\overline{u'w'}$ and $-\rho\overline{u'v'}$ were low in the outer bank region and resulted in boundary shear stress less than predicted, which was contrary to an expected increase. Reduction in shear stress was attributed to the outer-bank circulating cell acting in a direction opposite that of the primary secondary flow and was further suggested that the reduction in turbulence helps support the hypothesis that the cell protects from the core of maximum velocity.

Blanckaert and Graf (2001) found the turbulent shear component $-\rho\overline{v'w'}$ is related to the circulation cells and reaches a maximum at the cells' center.

Turbulent Reynolds stresses have been used by many in the presence of complex flows to estimate bed shear stress. Reynolds stresses provide estimates that are not reliant on 1-D assumptions given transverse components are utilized in approximations. Flows in meandering bends exhibit 3-D characteristics and approximations using Reynolds stresses make the method appropriate for this study. Extrapolation of Reynolds stress profiles should be used if trends are discernable to account for expected increases in shear stress due to bed roughness (Biron *et al.* 2004).

2.3.5 Turbulent Kinetic Energy

TKE is the mean kinetic energy per unit mass associated with large eddies in turbulent flow whose dimensions are comparable with height above the bed. Large eddies breakdown into successively smaller eddies until they are small enough for viscous forces to take effect near the bed. Generally, turbulent energy and shear stress increase to a maximum value near the bed (Soulsby 1983).

In oceanographic studies, TKE approximately 1 meter above the bed is related to the shear stress at the bed (Soulsby 1983). Soulsby (1983) states that within a few meters of the seabed there is a surface layer where the decrease with height of shear stress is a small fraction of bed shear. Furthermore, Reynolds stresses and variances in this region are more or less constant with height and are proportional to u_*^2. By averaging Reynolds stress values above the bed in the surface layer region, TKE proportionality constants have been determined varying from 0.18 to 0.2 (Soulsby 1983). Kim *et al.* (2000), in estimating bottom shear stress in a tidal boundary layer, concluded that more study is needed to determine the relationships between TKE and shear stress as they found a best-fit constant of 0.21 near the bed:

$$\tau_o = C\left[0.5\rho\left(\overline{u'^2} + \overline{v'^2} + \overline{w'^2}\right)\right]$$

Equation 2.34

where

τ_o = boundary shear stress [ML^{-1}T^{-2}];

C = proportionality constant (0.19) [dimensionless];

42

ρ = mass density [ML^{-3}];

u' = velocity fluctuations in the downstream direction [LT^{-1}];

v' = velocity fluctuations in the transverse direction [LT^{-1}]; and

w' = velocity fluctuations in the vertical direction [LT^{-1}].

Biron *et al*. (2004) used the TKE proportionality constant to estimate shear stress in a fluvial environment with simple and complex flow fields. They determined that in a complex flow field over a mobile bed, the TKE method produced the best match with bed topography with marked increase of shear stress values over scour holes. Biron *et al*. (2004) suggest that in a complex flow field, the TKE method is most appropriate because stream-wise velocity fluctuations may contribute more to shear stress than the vertical fluctuations. It is noted that contrary to oceanographic studies, shear stress estimates are determined close to the bed and that proportionality constants may vary markedly. In their concluding remarks, they suggest that the proportionality constant should be evaluated in laboratory and river environments (Biron *et al*. 2004). Tilston (2005) found the TKE method most reasonable in a field study of shear stress in a meandering bend due to the method being insensitive to sensor alignment errors.

2.4 Literature Review Summary

This literature review has presented the many facets associated with the current research. As a precursor, known generalized flow and shear stress distributions in meandering channels were presented. Previous research conducted and resulting design guidelines used in practice were then presented. Finally, methods for determining local shear stress and instances where each method was applied in similar applications were given.

Previous studies conducted in controlled laboratory environments have been primarily trapezoidal in cross section (Ippen *et al*. 1960, 1962, USBR 1964, Yen 1965, Sin 2010). Furthermore, of the studies conducted, only two presented comparisons of methods for estimating bed shear stress in meandering bends (Sin 2010, Tilston 2005). Tilston (2005) conducted research in a natural environment which is limited by constant changes in flow conditions and resulting bed topography. This study provides comparisons of methods for estimating shear stress with data collected in a proportionally representative laboratory model of two bends in the Middle Rio Grande. Scale of the physical model used in this study enabled acquisition of detailed velocity profiles and turbulent statistics throughout the water column

utilizing state-of-the-art technology. Research reported herein presents comparisons of methods for estimating bed shear stress and identifies possible increases in shear stress caused by natural topographic features.

3 EXPERIMENTAL SETUP

3.1 Native Topography

Design of the native topography was based on cross-sectional data taken by the USBR of two bends found in the Middle Rio Grande: 1) the Cochiti and 2) San Felipe bends (USBR 2000). Plan views of the surveyed bends are presented in Figure 3.1. Proportional representations of the surveyed bends were combined creating a full meander wavelength with the Cochiti and San Felipe bends represented in the upstream and downstream, respectively. Walker (2008) provides development and construction of the physical model.
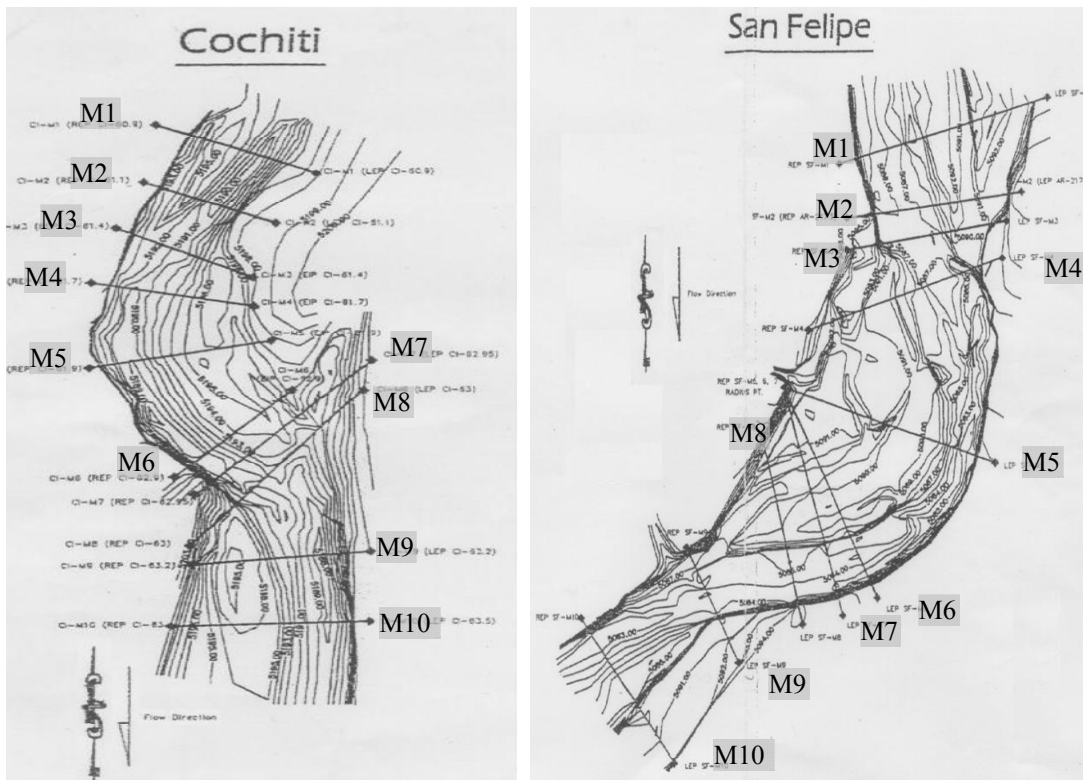
Figure 3.1: Plan View of Cross Sections Provided by the USBR for the Cochiti and San Felipe Bends (Walker 2008)

Physical model bed and banks were lined with a grouted mixture composed of 1/4-in. gravel, which corresponds to an estimated Manning's value (*n*) of 0.018. Tests were conducted for 8, 12, and 16 cfs flows with 16 cfs representing the maximum capacity of the system. Flow depths within the model were controlled by stop logs at the downstream end to maintain subcritical flow conditions and prevent drawdown. Modeled average bankfull width and depths are given in Table 3.1 and model cross sections are presented in Appendix A. Radii of curvature for the upstream and downstream bends are 41.5 ft and 69.5 ft, respectively.

Table 3.1: Bankfull Width and Depth per Model Cross Section

Cross-section Number	Top Width at Bankfull (ft)	Bankfull Depth (ft)
1	17.52	1.48
2	18.75	1.46
3	20.35	1.49
4	9.35	1.45
5	11.01	1.37
6	12.97	1.25
7	13.56	1.23
8	14.73	1.04
9	12.23	1.33
10	10.52	1.38
11	10.57	1.26
12	9.95	1.34
13	9.45	1.39
14	9.3	1.45
15	10.05	1.4
16	11.03	1.37
17	14.7	1.21
18	14.87	1.25

3.2   Test Setup and Instrumentation

The laboratory model was equipped with a mobile data-acquisition cart capable of minor rotation enabling the cart to be oriented parallel to channel cross sections. Figure 3.2 presents a photograph of the mobile data-acquisition cart and laboratory setup. Instrumentation used for data collection was mounted on point gages that were able to move laterally along a cross section on a leveled piece of angle iron mounted on the front of the data-acquisition cart. Data acquisition included velocity, shear stress, discharge, and depth measurements as well as

surveying of bed topography. Instrumentation used to measure each of the aforementioned parameters is described herein.

Figure 3.2: Overview of Data-acquisition Cart and Laboratory Setting

3.2.1 Flow Rate Measurement

The laboratory was equipped with two 85-horsepower pumps that recirculate flow to the headbox through two 12-in. pipes from a sump located at the downstream end of the model. Flow was controlled by butterfly valves mounted on a bypass that diverts flow back to the sump. Flow rates were maintained by additional butterfly valves that create back pressure to the pumps. Flow rates were measured by a George Fischer® SIGNET 2550 Insertion Magmeter installed in each pipe (Figure 3.3). The SIGNET 2550 is accurate within ±2%. Digital displays of magmeter readings were mounted on the data-acquisition cart, which was monitored throughout data-acquisition procedures.

Figure 3.3: SIGNET 2550 Insertion Magmeters and Digital Display Boxes
(Kinzli 2005)

3.2.2 Flow Depth Measurements

The flow depth was measured at each testing location with the use of a standard point gage capable of measuring ±0.001 ft. Point gages were mounted on the front of the data-acquisition cart along a leveled piece of angle iron to ensure accurate results. Flow depths were calculated as the difference between bed and water-surface elevations.

3.2.3 Velocity Measurements

3-D velocity measurements were taken with a SonTek® Acoustic Doppler Velocimeter (ADV). The probe has three arms corresponding to the x, y, and z axis which relate to the downstream, lateral, and vertical flow directions, respectively, due to cart orientation. Acoustic Doppler velocimetry works by emitting an acoustic burst into the water column, where the signal is reflected off of suspended particles to the three corresponding arms as depicted in Figure 3.4. Travel times of the acoustic signal are post-processed to determine velocities.
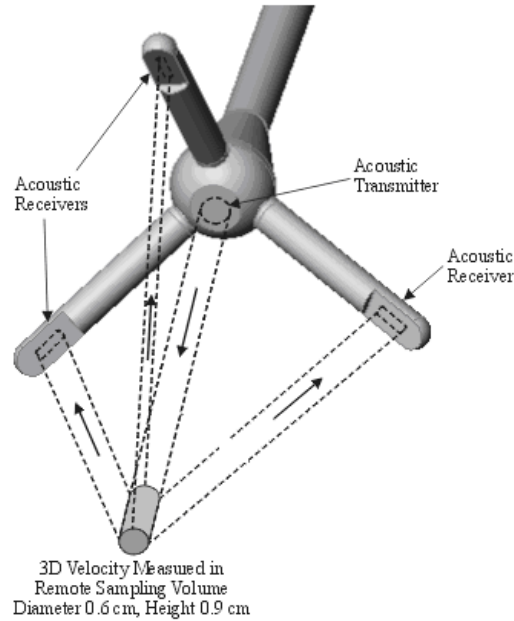
Figure 3.4: ADV Measurement Principles (Sontek 2001)

Velocity measurements were recorded by a personal computer and the HorizonADV program (Sontek 2001) at a rate of 25 Hz over a period of 60 seconds. The ADV probe was mounted on a standard point gage to ensure accuracy of testing locations in the water column. The sampling volume was located 0.164 ft (5 cm) below the acoustic transmitter, which hindered measurements in the upper portion of the water column at low flow depths. An example flow depth less than 1.64 ft would limit data collection at the 10% depth location.

3.2.4 Preston Tube Measurements

Shear stress was measured by use of a Preston tube capable of taking direct measurements on the bed and banks of the model from the data-acquisition cart. The Preston tube has two tubes: 1) a 1/4-in. bottom tube with an 11/64-in. port open to the current that collects the dynamic and hydrostatic pressures and 2) a 1/8-in. upper tube that receives the hydrostatic pressure through two small 1/32-in. ports on each side of the tube that are directed perpendicular to the flow (Figure 3.5). Resulting differential pressure was read by a Rosemount, low range (maximum: 5 in.), pressure transducer and recorded by LABView, data-acquisition software by National Instruments, Inc., over 30-sec intervals. Data collected were initially processed by converting the receiving amps to a voltage based upon a scale of 4 to 20 mA

corresponding to 1 to 5 Volts (V) by Ohm's Law. Recorded voltage was converted to differential pressure in inches by Equation 3.1. Finally, shear stress was calculated based upon a calibration coefficient determined in a 4-ft straight rectangular flume with a bed composed of the same material as that in the native topography model (Sclafani 2008). Differential pressures were related to shear stress values based upon momentum principles over a wide range of flow depths and velocities. Figure 3.6 gives the calibration curve and Equation 3.2 is the resulting calibration equation for the native topography bed:

$$dH = 0.75dV - 0.75 \qquad \textbf{Equation 3.1}$$

where

dH = differential head (in inches); and

dV = differential voltage (V).

$$\tau_o = 0.2986 \cdot dH \qquad \textbf{Equation 3.2}$$

where

τ_o = boundary shear stress (psf); and

dH = differential head (in inches).
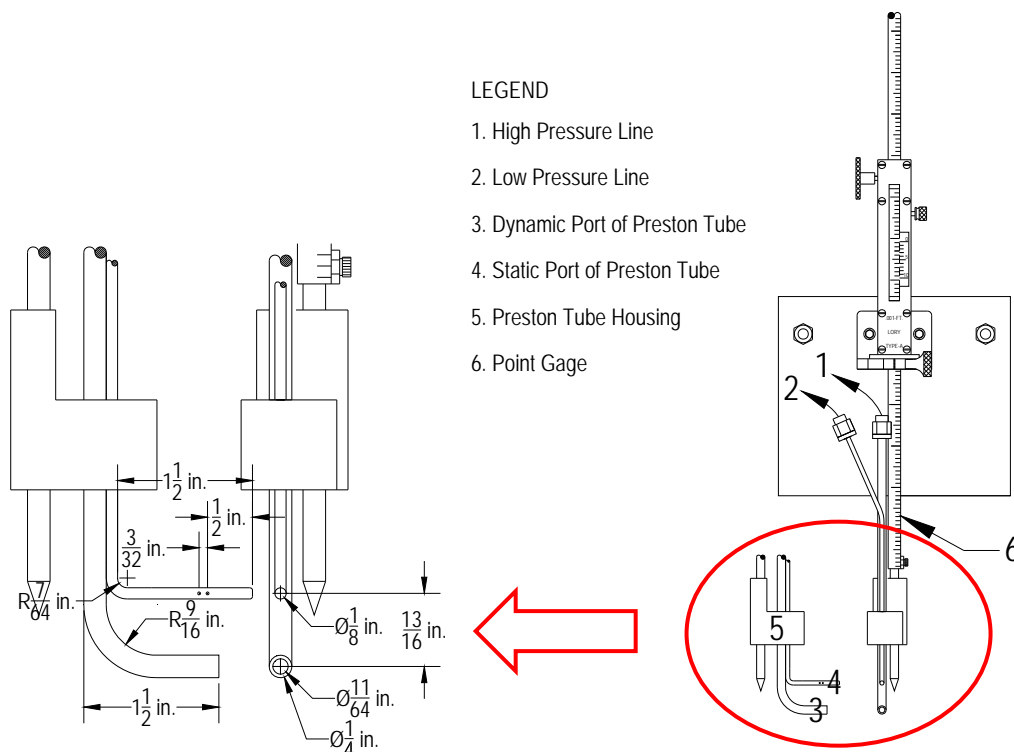
Figure 3.5: Preston Tube Schematic (Sclafani 2008)
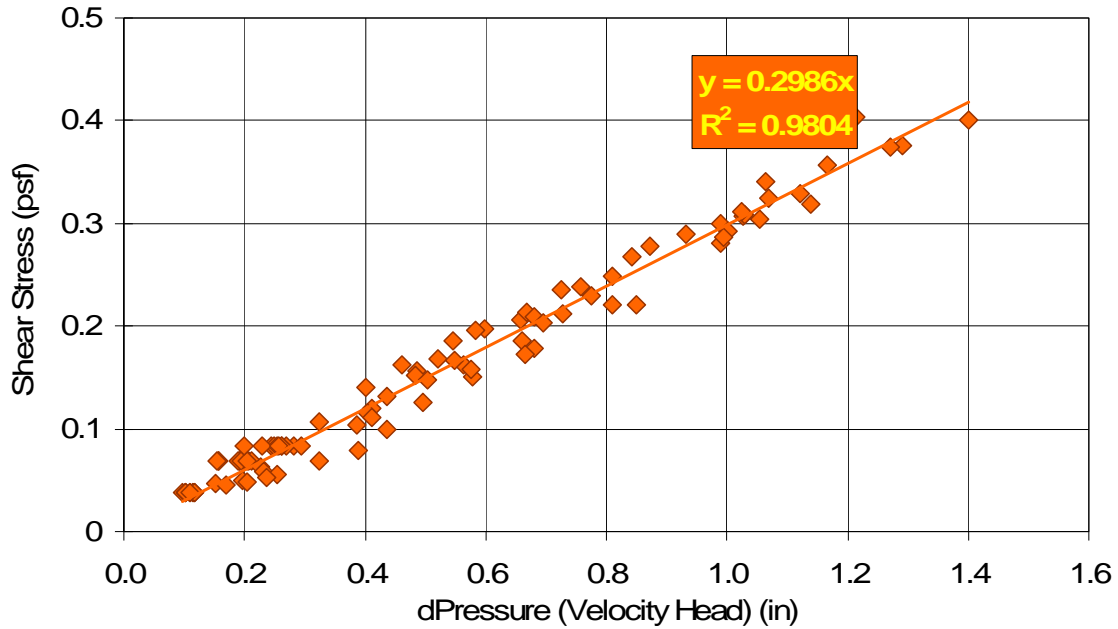
Figure 3.6: Calibration Results from Tests Conducted in a 4-ft Flume (Sclafani 2008)

Preston tube alignment at each testing location was oriented parallel to the flow assuming the flow was perpendicular to the radius of curvature, an assumption discussed in Section 4.1. Preston tube error was assumed negligible as long as the angle of attack of the flow was not greater than 15º from the radius of curvature.

4 TEST PROGRAM

A test program was created to provide extensive data for determining hydraulics associated with the native topographic features. Eighteen cross sections evenly spaced at 10.5-ft intervals were identified for data collection as depicted in Figure 4.1. For each cross section, measurements were taken at seven transverse locations, which were named alphabetically increasing from river right to left. Locations were determined, surveyed, and implemented by Walker (2008).
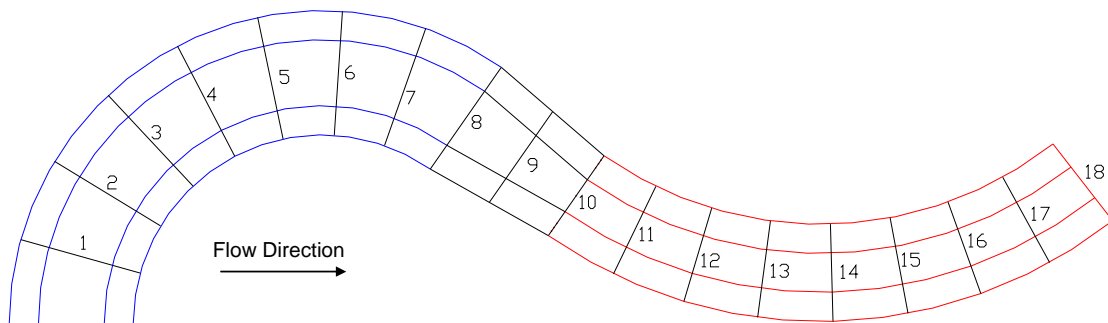
Figure 4.1: Model Cross-section Locations (Walker 2008)

Extensive acquisition of ADV data was conducted with samples taken at a minimum of 2.5%, 5%, or 10% incremental increases in percent depth depending on location. A test matrix was identified to remain consistent between discharges. Table 4.1 gives the percent depths for a given number of test points in the water column. The number of test points determined for each location is presented in Figure 4.2 and Figure 4.3.

Table 4.1: Percent Depths per Point Number Designation

	Number of Test Points						
	25	**23**	**21**	**19**	**15**	**13**	**9**
	97.5%	97.5%	97.5%	97.5%	95.0%	95.0%	95.0%
	95.0%	95.0%	95.0%	95.0%	92.5%	92.5%	92.5%
	92.5%	92.5%	92.5%	92.5%	90.0%	90.0%	90.0%
	90.0%	90.0%	90.0%	90.0%	87.5%	87.5%	85.0%
	87.5%	87.5%	87.5%	87.5%	85.0%	85.0%	80.0%
Percent Depth of Tests	85.0%	85.0%	85.0%	85.0%	82.5%	80.0%	70.0%
	80.0%	80.0%	80.0%	80.0%	80.0%	75.0%	50.0%
	77.5%	77.5%	75.0%	75.0%	75.0%	70.0%	30.0%
	75.0%	75.0%	70.0%	70.0%	70.0%	65.0%	10.0%
	72.5%	70.0%	65.0%	65.0%	65.0%	60.0%	
	70.0%	65.0%	60.0%	60.0%	60.0%	50.0%	
	67.5%	60.0%	55.0%	55.0%	55.0%	30.0%	
	65.0%	55.0%	50.0%	50.0%	50.0%	10.0%	
	60.0%	50.0%	45.0%	45.0%	30.0%		
	55.0%	45.0%	40.0%	40.0%	10.0%		
	50.0%	40.0%	35.0%	35.0%			
	45.0%	35.0%	30.0%	30.0%			
	40.0%	30.0%	25.0%	20.0%			
	35.0%	25.0%	20.0%	10.0%			
	30.0%	20.0%	15.0%				
	25.0%	15.0%	10.0%				
	20.0%	10.0%					
	15.0%	5.0%					
	10.0%						
	5.0%						
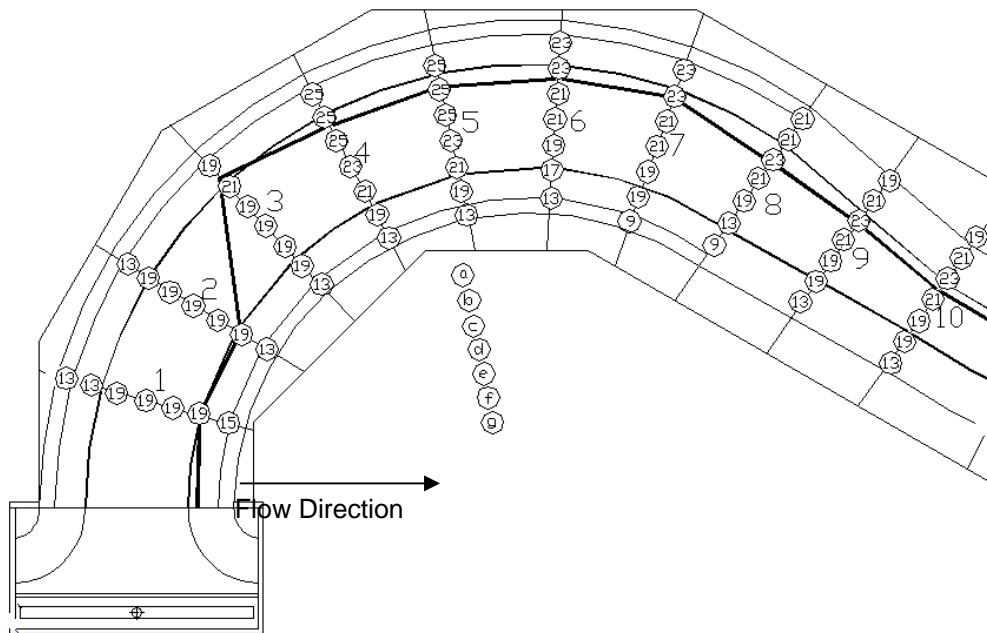
Figure 4.2: Testing Locations with Reference to Point Number Designations for the Upstream Bend
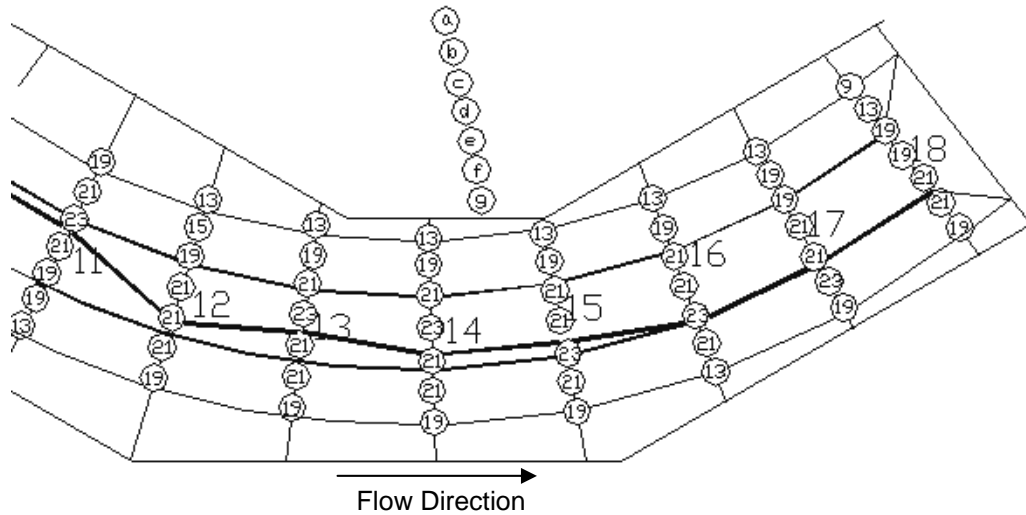
Figure 4.3: Testing Locations with Reference to Point Number Designations for the Downstream Bend

Preston tube measurements were taken at each location given flow depths were adequate to submerge the Pitot static tube. ADV measurements were limited near the surface due to a 5-cm vertical offset from the measured volume. A summary of ADV and Preston tube data collected is presented in Table 4.2.

Table 4.2: Number of ADV and Preston Tube Measurements per Location and Discharge

Cross-section Number	Location	ADV			Preston Tube		
		8 cfs	12 cfs	16 cfs	8 cfs	12 cfs	16 cfs
1	a	9	11	11	0	1	0
1	b	11	11	12	1	1	1
1	c	16	16	18	1	1	1
1	d	17	16	18	1	1	1
1	e	17	17	18	1	1	1
1	f	17	18	18	1	1	1
1	g	14	14	14	1	1	1
Cross Section 1 Totals		**101**	**103**	**109**	**6**	**7**	**6**
2	a	11	12	12	1	1	1
2	b	17	17	18	1	1	1
2	c	17	18	17	1	1	1
2	d	18	16	18	1	1	1
2	e	17	18	18	1	1	1
2	f	17	18	18	1	1	1
2	g	11	12	12	1	1	1
Cross Section 2 Totals		**108**	**111**	**113**	**7**	**7**	**7**

Cross-section Number	Location	ADV			Preston Tube		
		8 cfs	12 cfs	16 cfs	8 cfs	12 cfs	16 cfs
3	a	14	16	17	1	1	1
3	b	18	19	19	1	1	1
3	c	16	17	17	1	1	1
3	d	9	15	16	1	1	1
3	e	9	14	16	1	1	1
3	f	11	15	17	1	1	1
3	g	8	11	11	1	1	1
Cross Section 3 Totals		**85**	**107**	**113**	**7**	**7**	**7**
4	a	21	22	22	1	1	1
4	b	22	22	23	1	1	1
4	c	22	22	23	1	1	1
4	d	19	20	20	1	1	1
4	e	18	18	18	1	1	1
4	f	15	16	15	1	1	1
4	g	0	0	10	0	1	1
Cross Section 4 Totals		**117**	**120**	**131**	**6**	**7**	**7**
5	a	19	20	21	1	1	1
5	b	22	22	23	1	1	1
5	c	22	22	23	1	1	1
5	d	19	20	20	1	1	1
5	e	17	18	18	1	1	1
5	f	12	15	16	1	1	1
5	g	0	3	0	0	1	1
Cross Section 5 Totals		**111**	**120**	**121**	**6**	**7**	**7**
6	a	18	19	19	1	1	1
6	b	20	20	21	1	1	1
6	c	16	18	17	1	1	1
6	d	15	18	18	1	1	1
6	e	14	15	17	1	1	1
6	f	4	13	15	1	1	1
6	g	0	9	11	1	1	1
Cross section 6 Totals		**87**	**112**	**118**	**7**	**7**	**7**
7	a	17	18	19	1	1	1
7	b	20	20	20	1	1	1
7	c	14	16	17	1	1	1
7	d	12	14	16	1	1	1
7	e	11	14	17	1	1	1
7	f	6	12	15	1	1	1
7	g	0	0	6	0	1	1
Cross Section 7 Totals		**80**	**94**	**110**	**6**	**7**	**7**
8	a	14	16	18	1	1	1
8	b	17	18	18	1	1	1
8	c	18	19	20	1	1	1
8	d	14	16	18	1	1	1
8	e	7	12	16	1	1	1

Cross-section Number	Location	ADV			Preston Tube		
		8 cfs	12 cfs	16 cfs	8 cfs	12 cfs	16 cfs
8	f	0	0	10	0	1	1
8	g	0	0	6	0	0	1
Cross Section 8 Totals		**70**	**81**	**106**	**5**	**6**	**7**
9	a	10	15	17	1	1	1
9	b	18	19	19	1	1	1
9	c	20	20	21	1	1	1
9	d	16	18	19	1	1	1
9	e	14	16	18	0	1	1
9	f	12	16	17	0	0	1
9	g	3	11	11	0	0	0
Cross Section 9 Totals		**93**	**115**	**122**	**4**	**5**	**6**
10	a	10	15	17	1	1	1
10	b	18	19	20	1	1	1
10	c	20	20	21	1	1	1
10	d	18	18	19	1	1	1
10	e	15	17	18	1	1	1
10	f	14	17	17	0	1	1
10	g	10	11	12	0	0	1
Cross Section 10 Totals		**105**	**117**	**124**	**5**	**6**	**7**
11	a	0	12	16	1	1	1
11	b	16	18	19	1	1	1
11	c	19	20	20	1	1	1
11	d	17	18	18	1	1	1
11	e	14	17	17	1	1	1
11	f	11	16	17	1	1	1
11	g	6	11	8	1	1	1
Cross Section 11 Totals		**83**	**112**	**115**	**7**	**7**	**7**
12	a	0	6	8	1	1	1
12	b	7	12	13	1	1	1
12	c	15	16	16	1	1	1
12	d	17	18	19	1	1	1
12	e	18	19	20	1	1	1
12	f	16	18	18	1	1	1
12	g	0	10	15	1	1	1
Cross Section 12 Totals		**73**	**99**	**109**	**7**	**7**	**7**
13	a	0	0	8	0	1	1
13	b	12	16	17	1	1	1
13	c	18	18	19	1	1	1
13	d	19	20	21	1	1	1
13	e	18	19	19	1	1	1
13	f	17	18	19	1	1	1
13	g	12	15	17	1	1	1
Cross Section 13 Totals		**96**	**106**	**120**	**6**	**7**	**7**
14	a	0	0	10	0	1	1

Cross-section Number	Location	ADV 8 cfs	ADV 12 cfs	ADV 16 cfs	Preston Tube 8 cfs	Preston Tube 12 cfs	Preston Tube 16 cfs
14	b	12	15	17	1	1	1
14	c	17	18	19	1	1	1
14	d	19	20	20	1	1	1
14	e	19	18	20	1	1	0
14	f	18	19	19	1	1	1
14	g	13	15	17	1	1	1
Cross Section 14 Totals		**98**	**105**	**122**	**6**	**7**	**6**
15	a	0	0	7	0	1	1
15	b	13	15	16	1	1	1
15	c	17	17	19	1	1	1
15	d	18	19	19	1	1	1
15	e	19	20	21	1	1	1
15	f	16	17	18	1	1	1
15	g	0	3	11	0	1	1
Cross Section 15 Totals		**83**	**91**	**111**	**5**	**7**	**7**
16	a	0	6	10	1	1	1
16	b	15	17	17	1	1	1
16	c	17	20	18	1	1	1
16	d	18	19	19	1	1	1
16	e	20	20	20	1	1	1
16	f	16	17	18	1	1	1
16	g	0	6	11	1	1	1
Cross Section 16 Totals		**86**	**105**	**113**	**7**	**7**	**7**
17	a	0	0	9	0	1	1
17	b	1	11	7	1	1	1
17	c	4	11	14	1	1	1
17	d	13	15	12	1	1	1
17	e	17	18	19	1	1	1
17	f	18	20	20	1	1	1
17	g	4	13	14	1	1	1
Cross Section 17 Totals		**57**	**88**	**95**	**6**	**7**	**7**
18	a	0	0	2	0	0	1
18	b	0	0	8	0	1	1
18	c	0	6	14	1	1	1
18	d	7	13	15	1	1	1
18	e	17	17	18	1	1	1
18	f	16	18	19	1	1	1
18	g	0	10	14	1	1	1
Cross Section 18 Totals		**40**	**64**	**90**	**5**	**6**	**7**
Total of Measurements		**1573**	**1850**	**2042**	**108**	**121**	**123**

4.1 Probe Alignment

Both ADV and Preston tubes were oriented in the flow direction by use of the data-acquisition cart. Measurement tape was placed along the cart railing and surveyed using an arbitrary coordinate system tailored to the laboratory. AutoCAD drawings of the laboratory were created from survey data, which enabled determination of stream parameters and cross referencing for tape and data-acquisition locations. As a result, the data-acquisition cart was oriented in the stream-wise direction. Figure 4.4 presents percent occurrence of deviation angles from the data-acquisition cart and assumed stream-wise direction as calculated by Equation 4.1. For simplicity, the absolute value of the deviation angle was taken; less than 3% of flows were in a direction opposite that of the primary. Angles greater than 15º can be attributed to re-circulation zones:

$$\theta = \left| \tan^{-1}\left(\frac{v_y}{v_x} \right) \right| \hspace{3cm} \textbf{Equation 4.1}$$

where

θ = deviation angle (º);

v_y = velocity in the transverse direction [LT⁻¹]; and

v_x = velocity in the stream-wise direction [LT⁻¹].
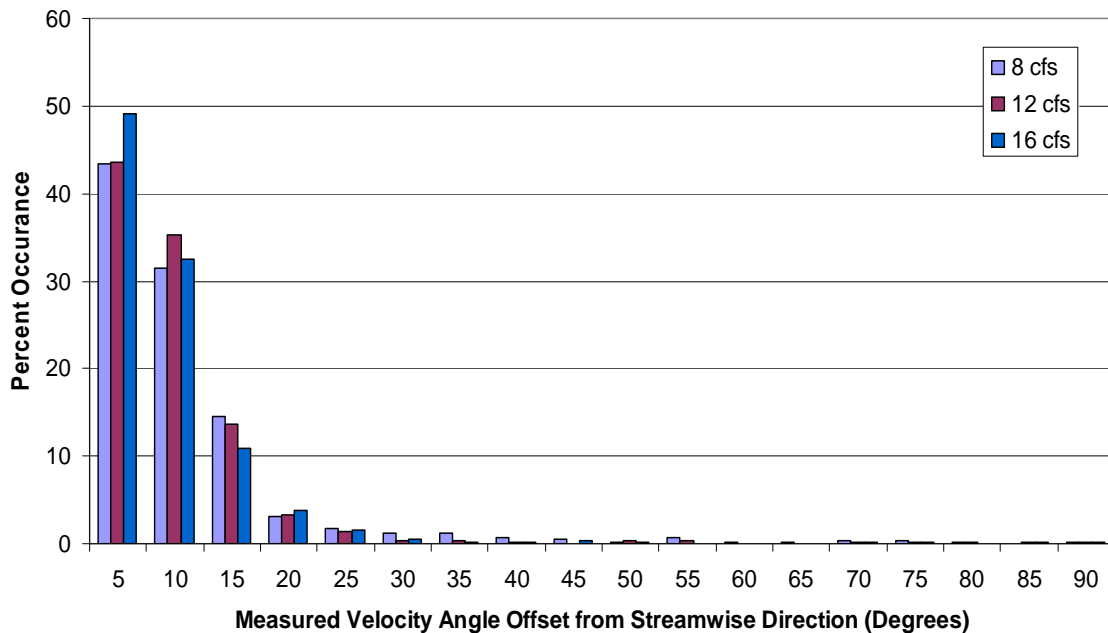
Figure 4.4: Deviation Angles from the Stream-wise Direction

4.2 Test Procedure

Testing began each day by filling the sump with water supplied by a 36-in. line connected directly to Horsetooth Reservoir. Pumps were then adjusted to stabilize the flow at the desired discharge. The cart was set at the appropriate location by referencing measurement tape along the railing and locked into place so that no movement occurred while taking measurements. Flow depths were found at each of the testing locations by bed and water-surface elevations measured by the standard point gage. ADV data were then taken at the appropriate percent depths based on the aforementioned test matrix. Preston tube measurements were taken directly on the bed at each location after ensuring the validity of the zero differential pressure at each cross section by placing the Preston tube in a bucket filled with still water. The Preston tube was back-flushed between measurements to make sure it was clear of any debris.

4.2.1 Post Processing

Post processing of ADV data was conducted utilizing WinADV software, a program developed by the USBR that statistically summarizes data collected. Data were filtered by a phase-space threshold despiking method proposed by Goring and Nikora (2002), which was adopted by the USBR into the WinADV program (Wahl 2002). Furthermore, data were filtered by examination of the sound-to-noise ratio (SNR) and correlations (COR). Data with SNRs below 15, or a correlation less than 70, were rejected from analysis as suggested by Sontek (2001). Near-bed measurements with SNRs larger than those in the rest of the water column were rejected due to the likelihood of bed interference as depicted in Figure 4.5 (Sontek 2001).
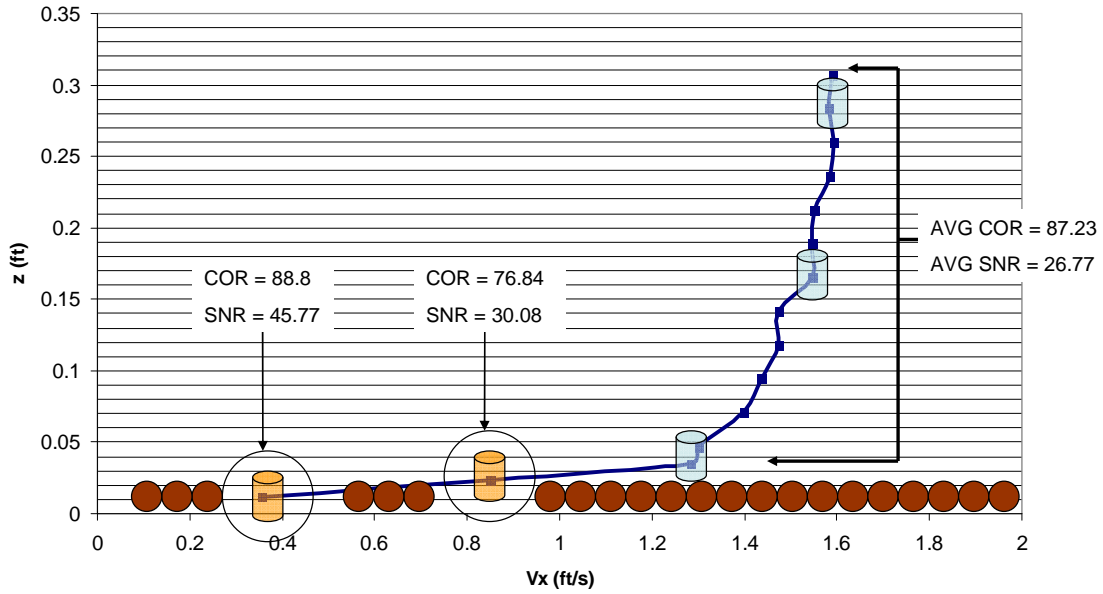
Figure 4.5: SNR for Near-bed ADV Measurements

ADV data were used for analysis of the logarithmic profiles as well as Reynolds stresses. McLelland and Nicholas (2000) examined Reynolds shear stresses measured by use of an ADV at various sampling rates including 25 Hz and found errors in measurements to be small.

5 DATA ANALYSIS

Data analysis consisted of calculating shear stress at all locations and discharges by the logarithmic law, Reynolds stresses, Preston tube, TKE, and reach-averaged boundary shear estimates (calculated shear stresses by method are tabulated in Appendix B). Distributions of results are presented spatially for each method along with detailed descriptions of calculation procedures used.

5.1   Reach-averaged Shear Stress (HEC-RAS)

A HEC-RAS model was created for the native topography model for calibration purposes by Walker (2008). The model is used herein to reference approach conditions to each bend as well as compare hydraulic outputs to measured data. Use of this model in determining shear stress in bends is unfounded due to the 1-D flow assumption, and because of its wide use (Gordon *et al*. 2004), provides purpose for this study. HEC-RAS uses a standard step backwater calculation procedure for steady flow runs to determine water-surface elevations as well as cross-sectional averaged shear stresses (USACE 2008). Cross-sectional averaged shear stresses are calculated by Equation 5.1:

$$\tau_o = \gamma R_h S_f \qquad \qquad \textbf{Equation 5.1}$$

where

τ_o = boundary shear stress $[\mathrm{ML^{-1}T^{-2}}]$;

γ = specific weight of water $[\mathrm{ML^{-2}T^{-2}}]$;

R_h = hydraulic radius $[\mathrm{L}]$; and

S_f = friction slope [dimensionless].

Boundary conditions were set as the downstream measured flow depth as the flow is subcritical. A representative view of the HEC-RAS model is given in Figure 5.1.
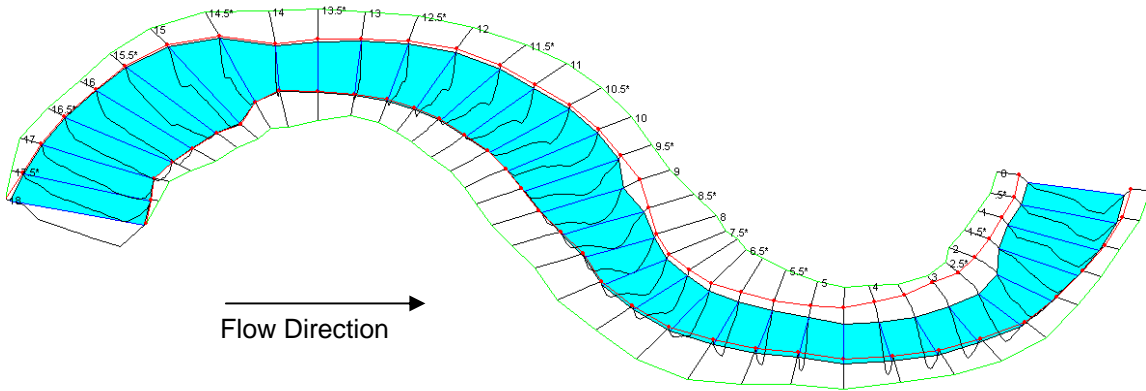
Figure 5.1: Representation of HEC-RAS Model with a 16-cfs Flow Rate

Calculated energy grade lines from measured data deviated from HEC-RAS output as seen in Figure 5.2, Figure 5.3, and Figure 5.4. Obvious errors can be seen due to increases in energy resulting in negative friction slopes, a result that is not physically possible.
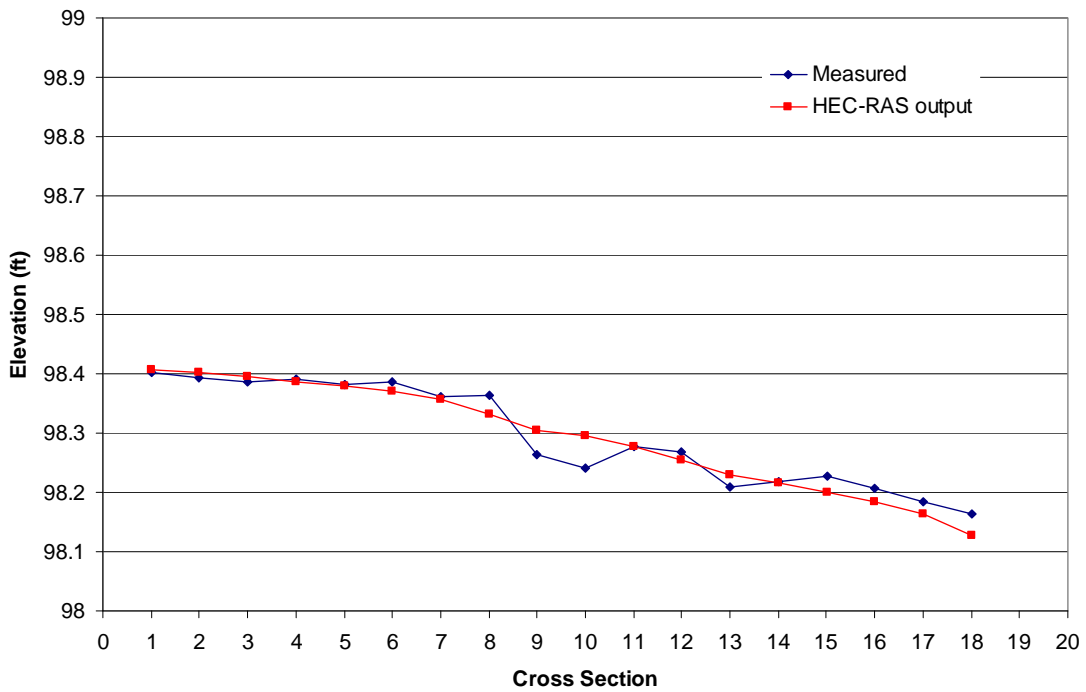
Figure 5.2: Energy Grade Line Comparison for 8 cfs
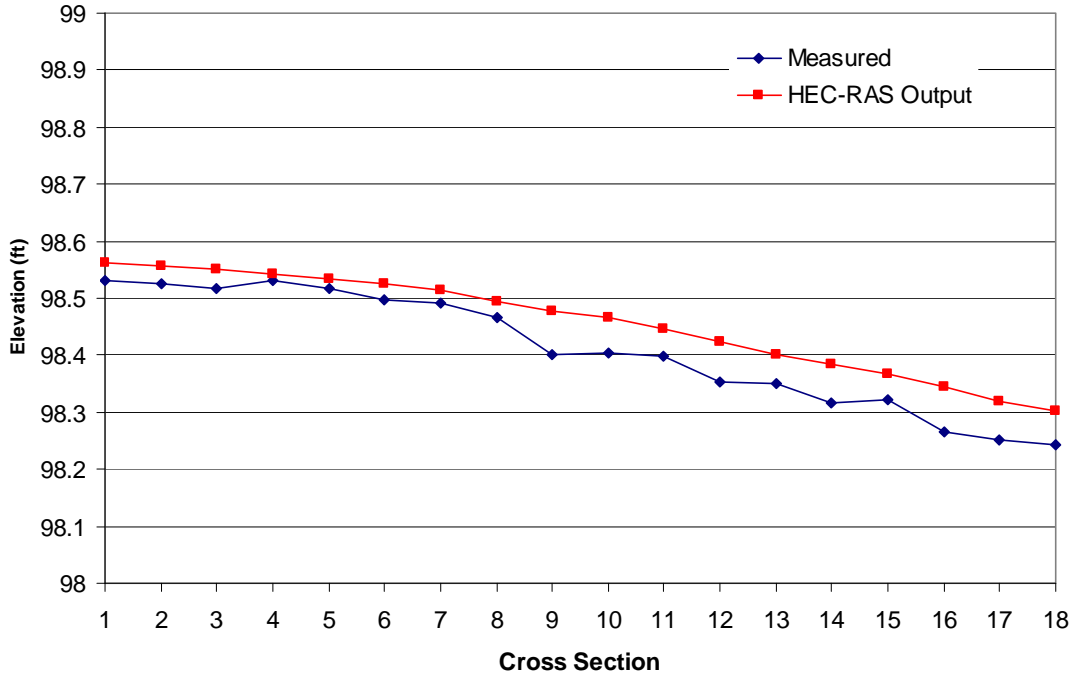
Figure 5.3: Energy Grade Line Comparison for 12 cfs
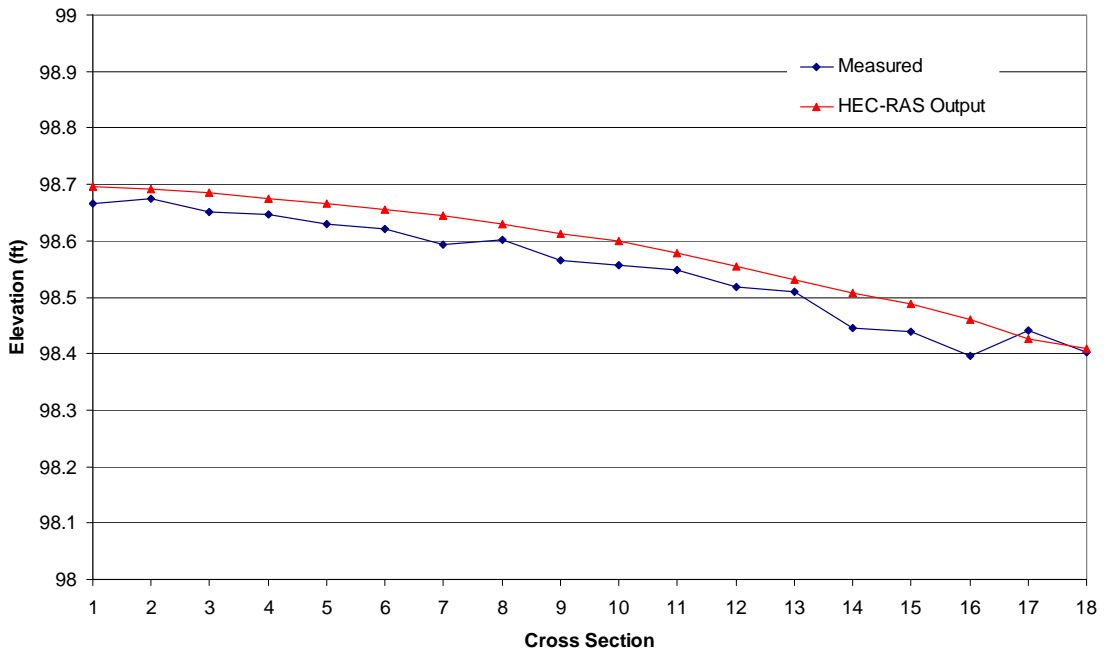
Figure 5.4: Energy Grade Line Comparison for 16 cfs

Shear stress distributions were generated with ArcGIS using HEC-RAS output for each of the three discharges as seen in Figure 5.5. It is once again noted that HEC-RAS outputs cross-sectional averaged shear stress values for steady flow simulations.
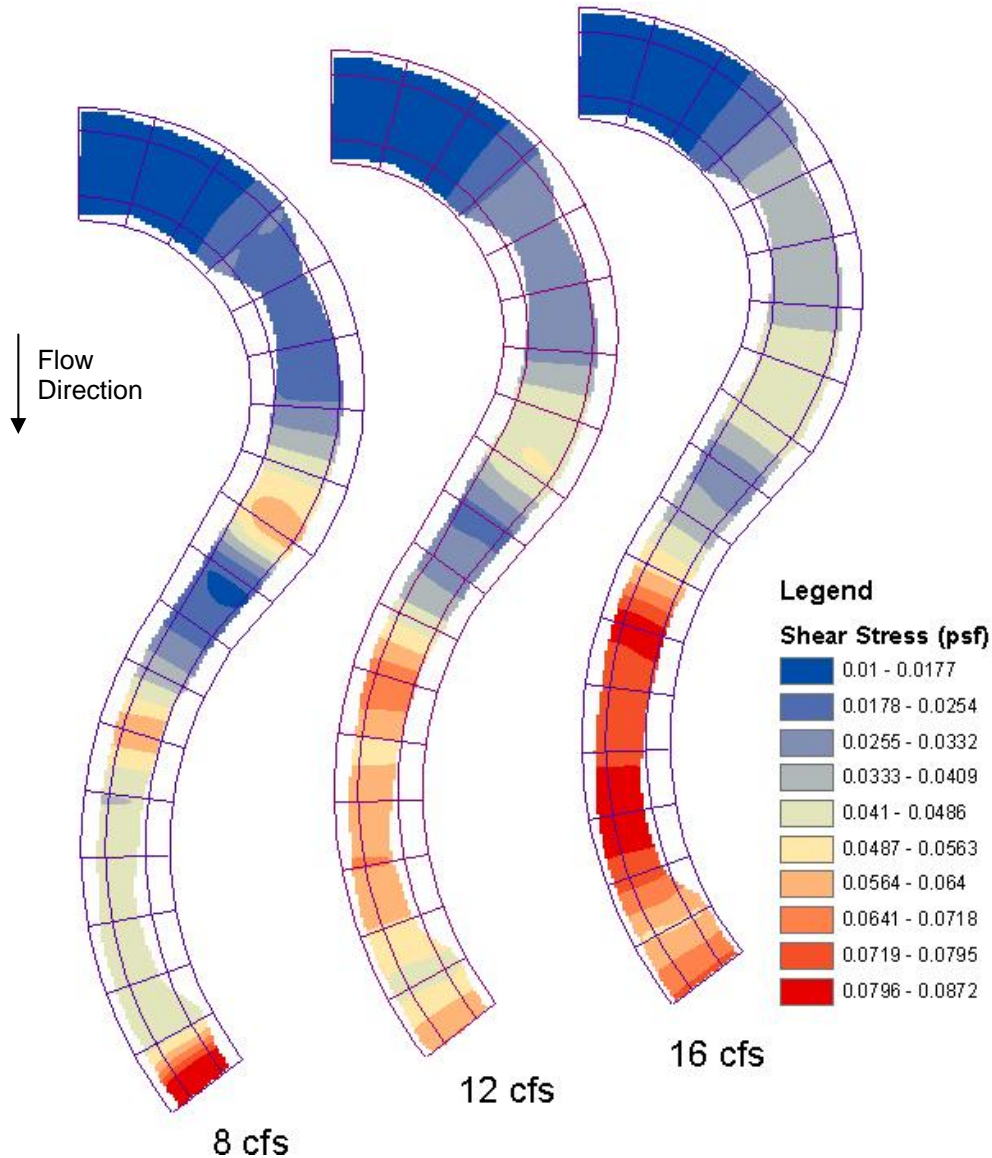
Figure 5.5: HEC-RAS Shear Stress Distribution per Discharge

5.2   Preston Tube

Differential pressure measurements taken on the bed surface with a Preston tube were converted to shear stress by a calibration equation determined in a straight 4-ft wide flume (Sclafani 2008). Calibration results were presented in Figure 3.6 and the resulting equation

relating differential pressure at the bed to shear stress was presented in Equation 3.2. Negative pressure measurements were discarded as the Preston tube is not capable of measuring differential pressures in opposite or perpendicular directions of flow. Negative values occurred in areas where recirculation was present, which accounted for 14% of data-collection locations. Distributions of shear stress values are presented in Figure 5.6 for each discharge.
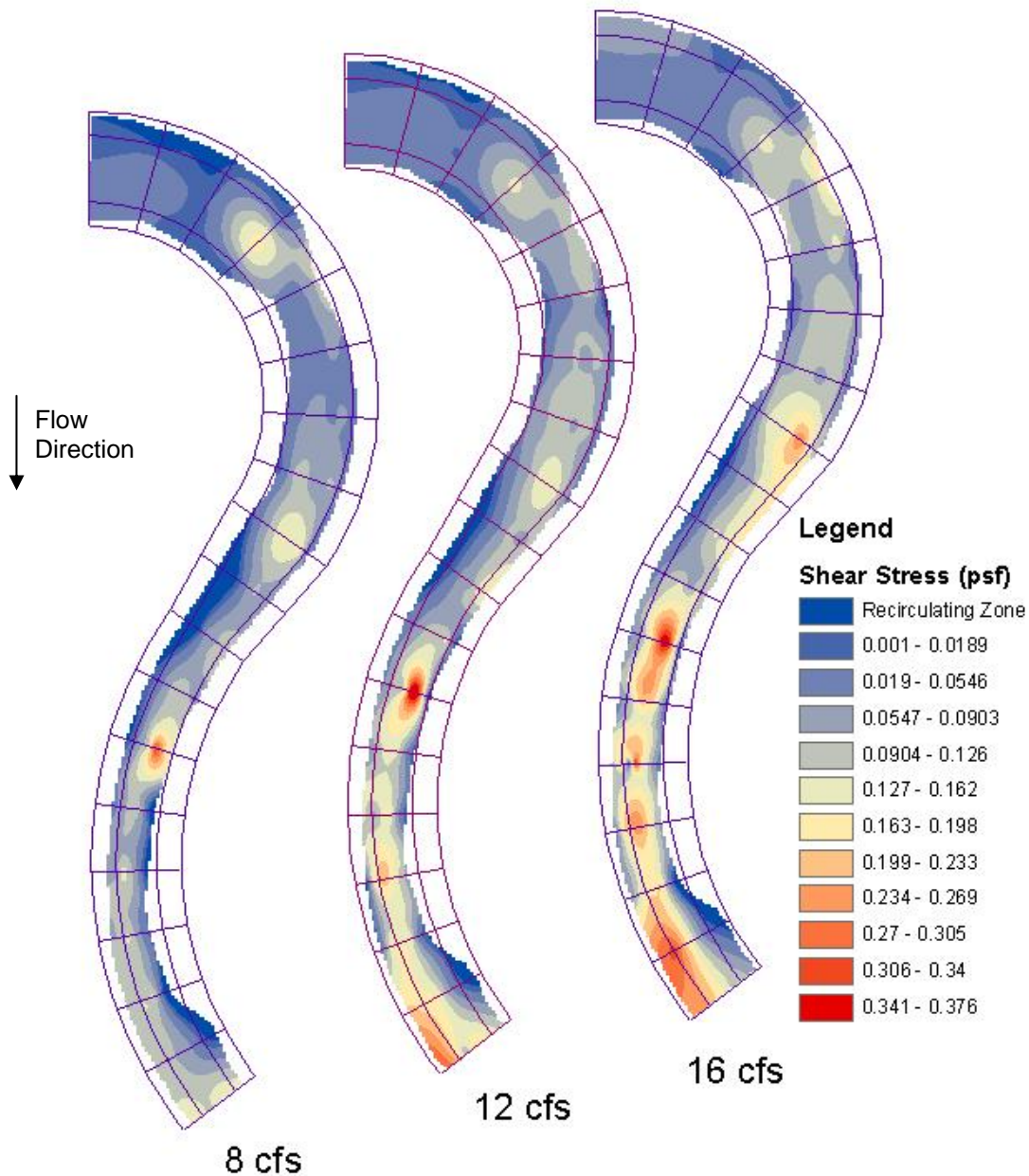
Figure 5.6: Preston Tube Shear Stress Distributions per Discharge

5.3 Law of the Wall

The law of the wall relates velocity gradient to bed shear by mixing length theory. Height of the viscous sublayer dictates where the logarithmic zone begins, which is related to grain roughness height and flow conditions. Median grain size for the native topography channel was 0.02083 ft, which is classified as fine gravel (Julien 1998). In general, gravel- and cobble-bed streams are hydraulically rough (Julien 1998). Hydraulically rough conditions were confirmed by Equation 2.10 and Equation 2.11, where the grain Reynolds number (Re_*) and laminar sublayer (δ) were computed as 120 and 0.002 ft for a location in the approach flow, respectively. Due to the size of the viscous sublayer it can be assumed, for all practical purposes, that velocity measurements were not able to be taken in this region. The sampling volume of the ADV is approximately fourteen times larger than the viscous sublayer.

Procedures used for estimating u_* and thus τ_o proposed by Bergeron and Abrahams (1992) were used in estimating shear stress values based on Equation 2.8. Bergeron and Abrahams (1992) stated that an estimate of the shear velocity can be obtained by regressing v_x and ln(z) with depth being the independent variable. The resulting equation for linear regression is given by Equation 5.2 and the estimated shear velocity by Equation 5.3 (Bergeron and Abrahams 1992). Shear velocity was then converted to shear stress by Equation 2.9:

$$v_x = m \ln z + c \qquad\qquad \textbf{Equation 5.2}$$

$$u_* = km \qquad\qquad \textbf{Equation 5.3}$$

where

    v_x = component of velocity in *x*-direction [LT^{-1}];

    m = regression slope;

    z = vertical distance from the boundary [L];

    c = intercept;

    u_* = shear velocity [LT^{-1}]; and

    k = von Kármán constant (0.41) [dimensionless].

Applicability of the logarithmic zone was found, in some instances, to extend beyond a relative depth of 0.2, which is similar to findings by Baird (2004). Therefore, velocity measurements below a relative depth of 0.2 were used for regression with exceptions where it was determined the logarithmic zone extended further in the water column. Figure 5.7 through

Figure 5.12 provide regression examples of logarithmic profiles for a location in each bend for each test discharge.

$$y = 0.2045x + 1.7895$$
$$R^2 = 0.9913$$

Shear velocity:
$$u_* = m \cdot k = 0.2045 \cdot 0.412 = 0.084 \text{ ft/s}$$
Boundary shear stress:
$$\tau_0 = \rho \cdot u_*^2 = 1.94 \text{ slugs/ft}^3 \cdot 0.084^2 \text{ ft}^2/\text{s}^2 = 0.0138 \text{ psf}$$
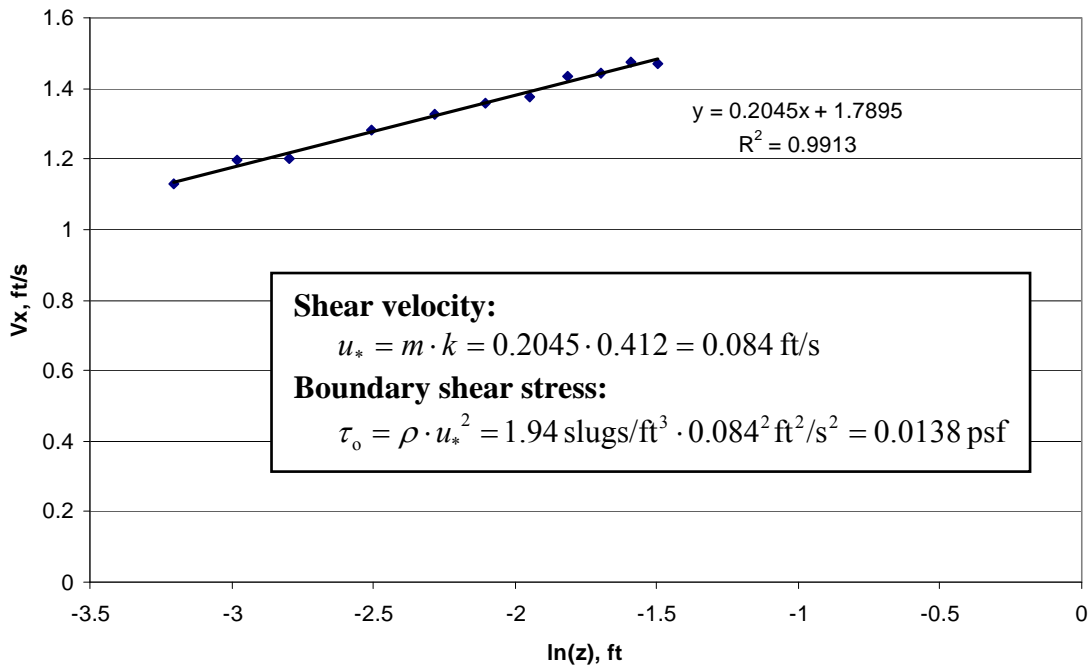
Figure 5.7: Regression of Logarithmic Profile for 8 cfs at Cross Section 6, Location e

$$y = 0.5342x + 3.1568$$
$$R^2 = 0.98$$

Shear velocity:
$$u_* = m \cdot k = 0.5342 \cdot 0.412 = 0.22 \text{ ft/s}$$
Boundary shear stress:
$$\tau_0 = \rho \cdot u_*^2 = 1.94 \text{ slugs/ft}^3 \cdot 0.22^2 \text{ ft}^2/\text{s}^2 = 0.094 \text{ psf}$$
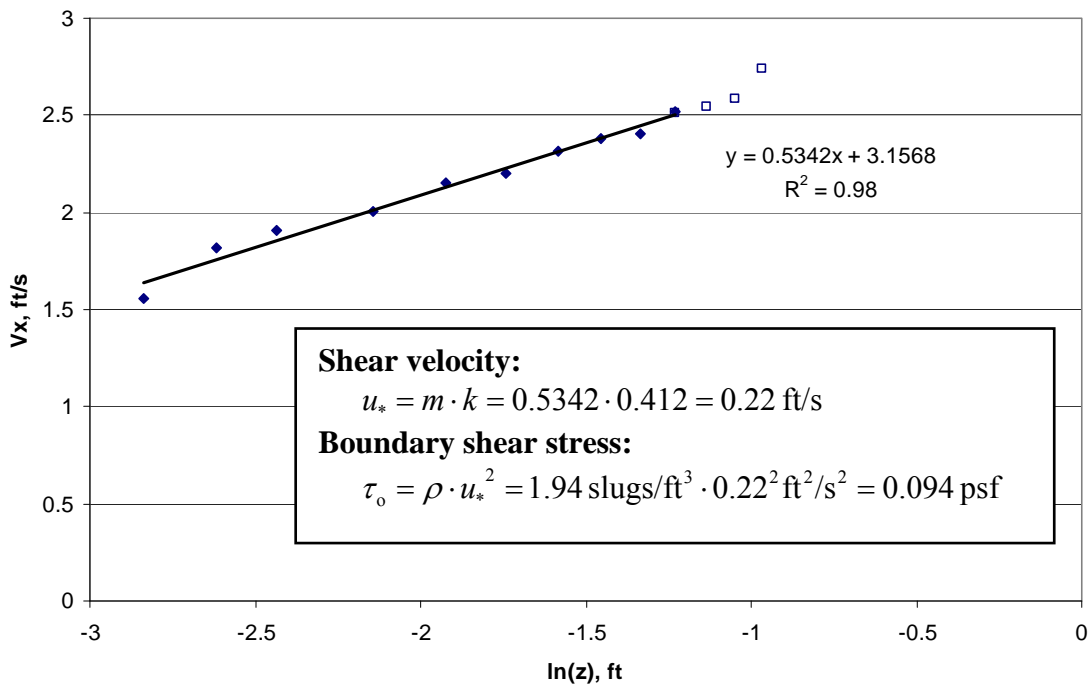
Figure 5.8: Regression of Logarithmic Profile for 8 cfs at Cross Section 11, Location b

$$y = 0.5874x + 3.1183$$
$$R^2 = 0.956$$

Shear velocity:
$$u_* = m \cdot k = 0.5874 \cdot 0.412 = 0.242 \text{ ft/s}$$
Boundary shear stress:
$$\tau_o = \rho \cdot u_*^2 = 1.94 \text{ slugs/ft}^3 \cdot 0.242^2 \text{ ft}^2/\text{s}^2 = 0.114 \text{ psf}$$
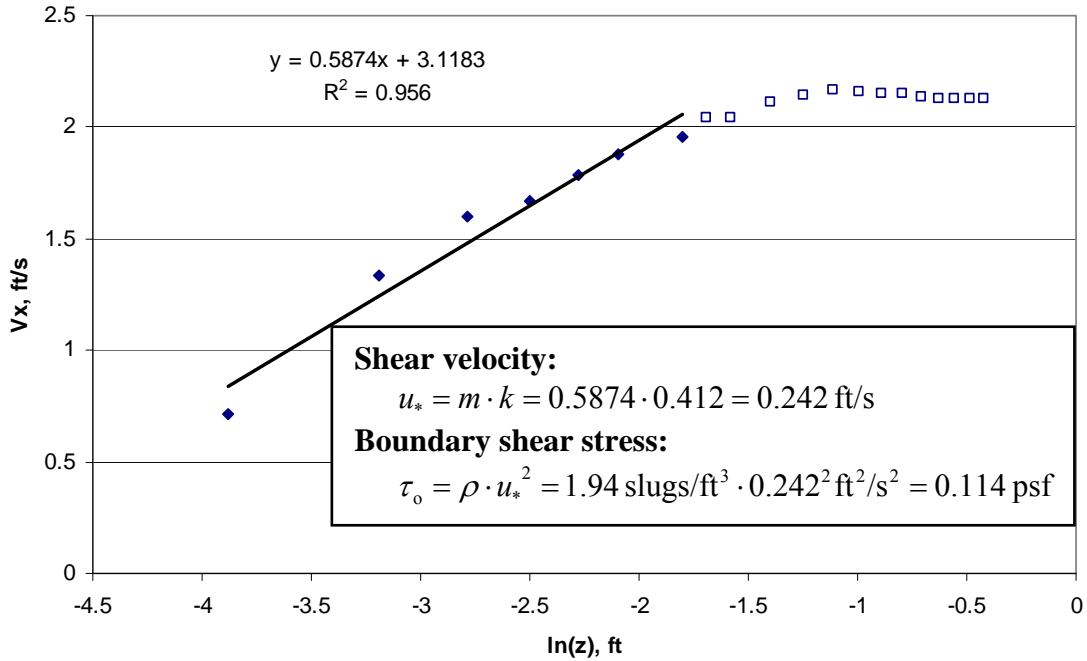
Figure 5.9: Regression of Logarithmic Profile for 12 cfs at Cross Section 5, Location d

$$y = 0.3109x + 2.7164$$
$$R^2 = 0.9494$$

Shear velocity:
$$u_* = m \cdot k = 0.3109 \cdot 0.412 = 0.128 \text{ ft/s}$$
Boundary shear stress:
$$\tau_o = \rho \cdot u_*^2 = 1.94 \text{ slugs/ft}^3 \cdot 0.128^2 \text{ ft}^2/\text{s}^2 = 0.0318 \text{ psf}$$
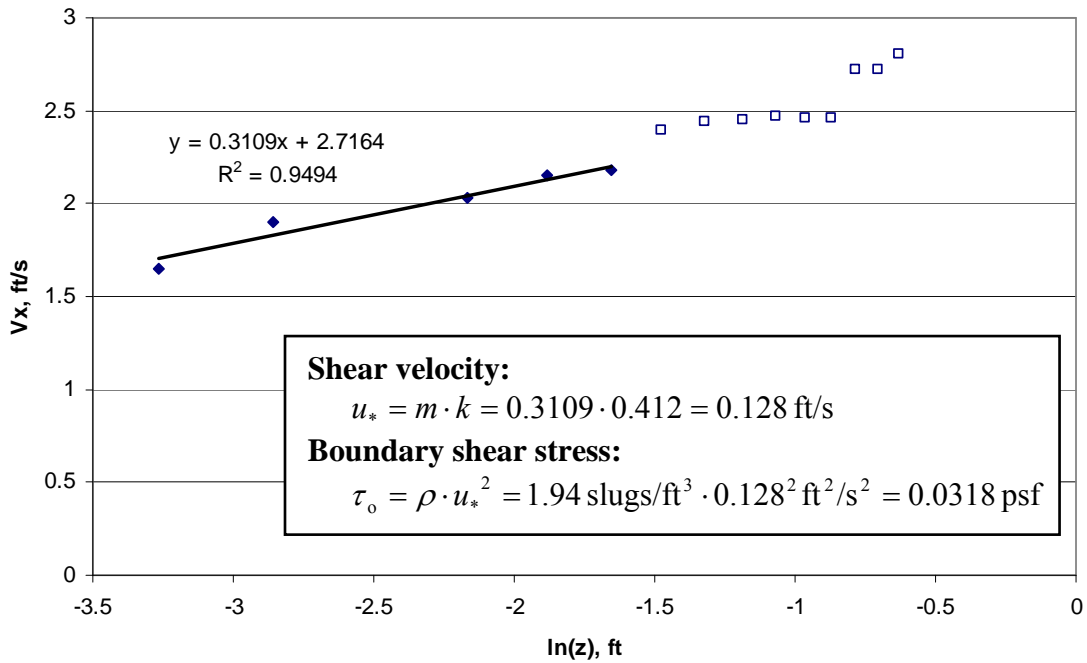
Figure 5.10: Regression of Logarithmic Profile for 12 cfs at Cross Section 15, Location c
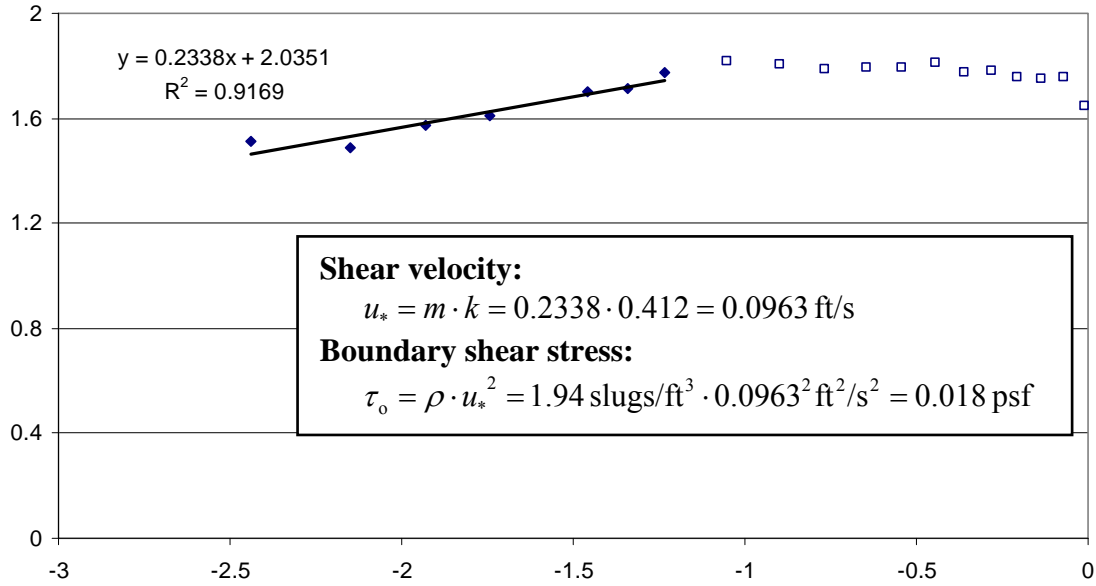
Figure 5.11: Regression of Logarithmic Profile for 16 cfs at Cross Section 6, Location b
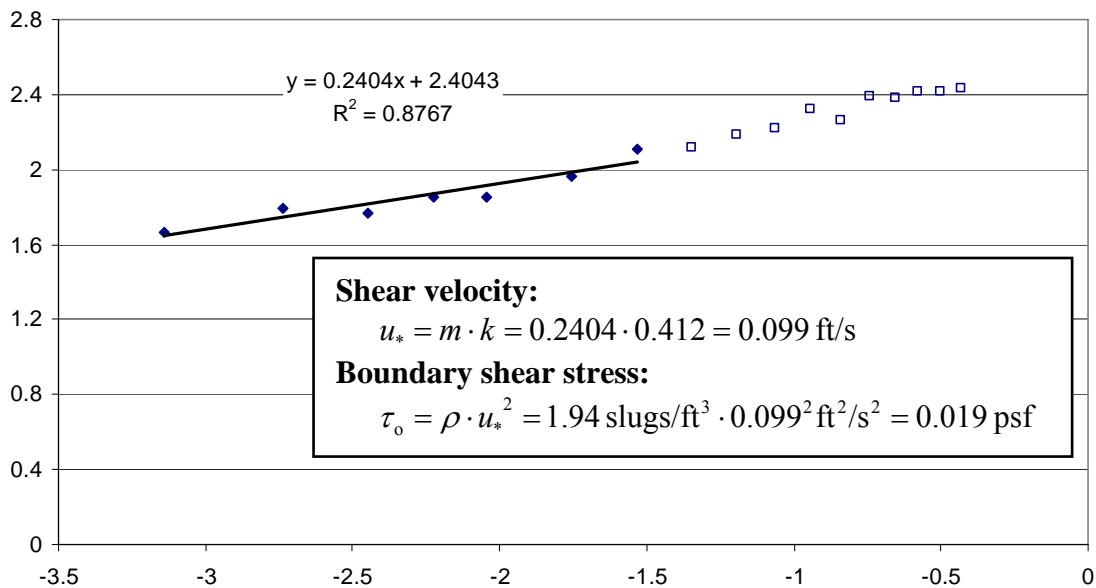
Figure 5.12: Regression of Logarithmic Profile for 16 cfs at Cross Section 14, Location c

Velocity profiles in recirculating zones did not exhibit a logarithmic profile, which accounted for 14% of data-collection locations. It is important to note that in implementing this method, it is assumed that transverse velocities did not affect primary velocity distributions.

Average coefficient of agreement from regression analysis was 0.9406. Figure 5.13 illustrates the resulting shear stress distribution for each discharge.
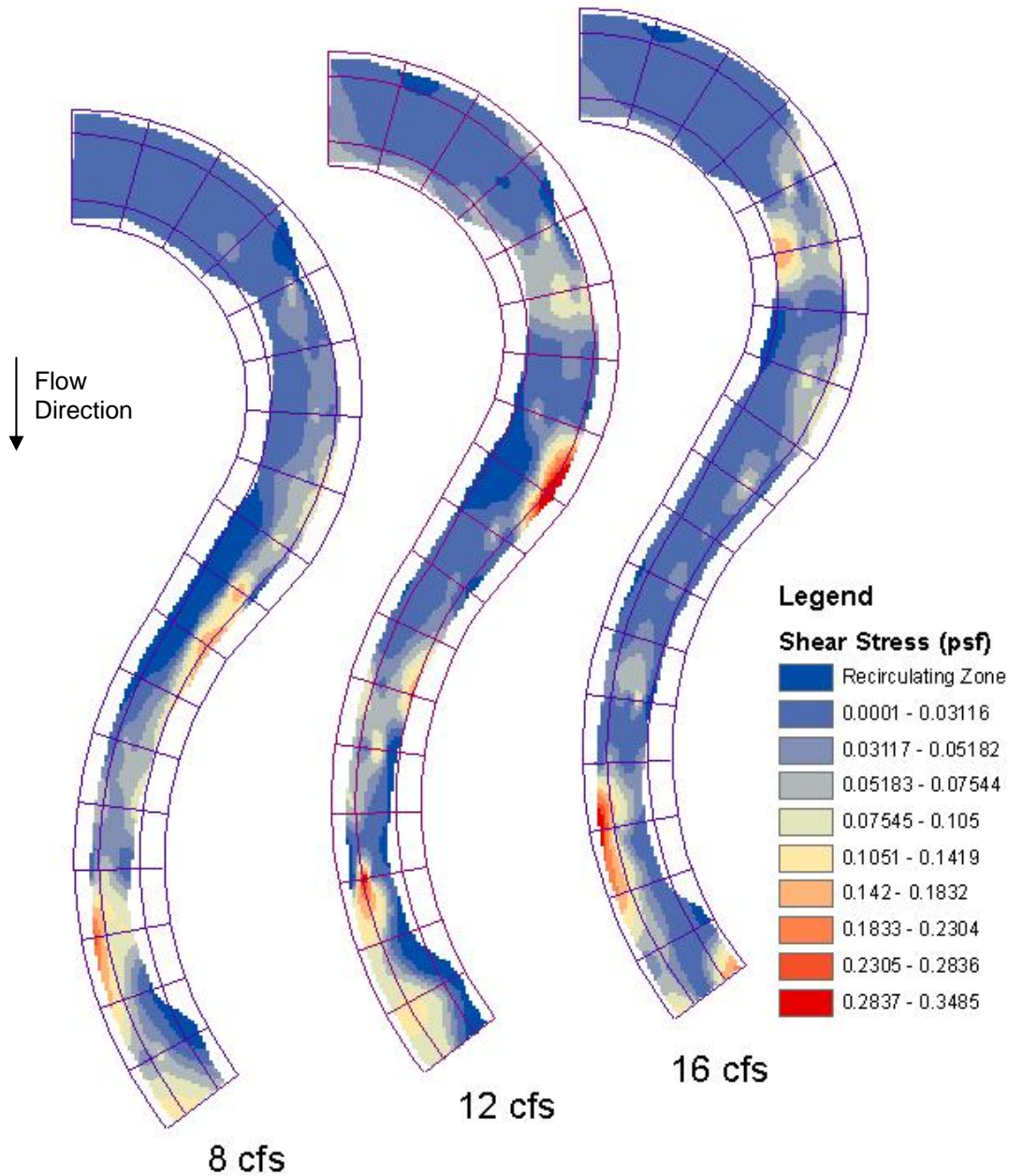
Figure 5.13: Law of the Wall Shear Stress Distributions per Discharge

5.4 Reynolds Stresses

Bed shear stresses were determined by the method utilized by Huthnance *et al*. (2002) and Tilston (2005), where velocity fluctuations acting on the vertical plane in the downstream

and transverse directions are used to determine a resultant bed shear stress as seen in Equation 2.30. Tilston (2005) notes the method is susceptible to error when velocity fluctuations are opposite that of the primary flow direction due to the use of the Pythagorean Theorem. Analysis conducted herein focuses on magnitude and not direction of the resultant shear and magnitudes of shear stresses in recirculating zones were assumed negligible.

Two analysis techniques were implemented to obtain bed shear stress values: 1) a single near-bed point and 2) an extrapolation technique. Extrapolation of correlated measurements in the water column has been found to provide a good estimate of the expected increase in bed shear stress with bed roughness (Biron *et al.* 2004).

5.4.1 Near-bed Point

Near-bed point Reynolds shear stress values obtained with an ADV were used to estimate shear stress at the boundary. Biron *et al.* (2004) found maximum Reynolds stress values at a relative depth of 0.1, which was used for this study after analysis of data collected. Analysis of maximum primary Reynolds stress ($-\rho\overline{u'w'}$) resulted in 48% of data locations with a maximum at or below a relative depth of 0.1 and 91.7% at or below a relative depth of 0.2, as illustrated in Figure 5.14. Given a relative depth of 0.1 is closest to the mean, the location was accepted as a standard location for analysis. When ADV data were insufficient for a relative depth of 0.1, the closest reliable data were used. Shear stress distributions for each discharge are given in Figure 5.15.
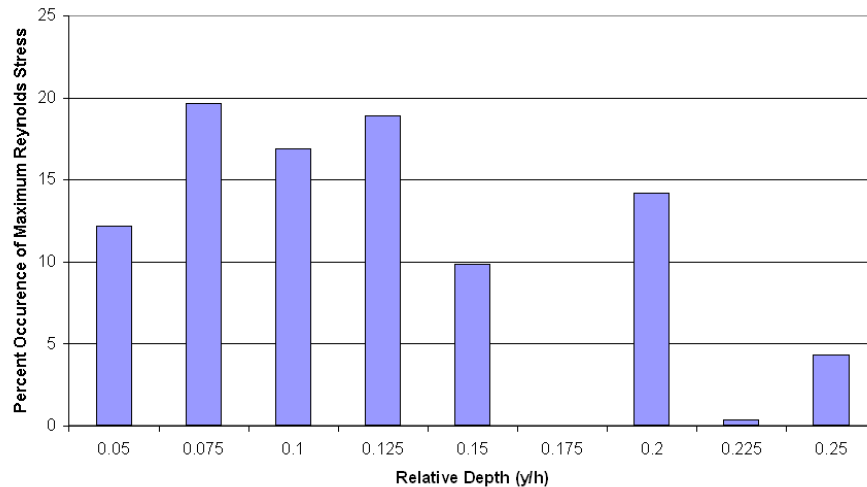
Figure 5.14: Percent Occurrence of Maximum Reynolds Stress $-\rho\overline{u'w'}$ per Measured Relative Depth

Flow Direction

Legend

Shear Stress (psf)

■	Recirculating Zone
■	0.001 - 0.00341
■	0.00342 - 0.00781
■	0.00782 - 0.0125
■	0.0126 - 0.0186
■	0.0187 - 0.0251
■	0.0252 - 0.0318
■	0.0319 - 0.0386
■	0.0387 - 0.0457
■	0.0458 - 0.0626

16 cfs

12 cfs

8 cfs
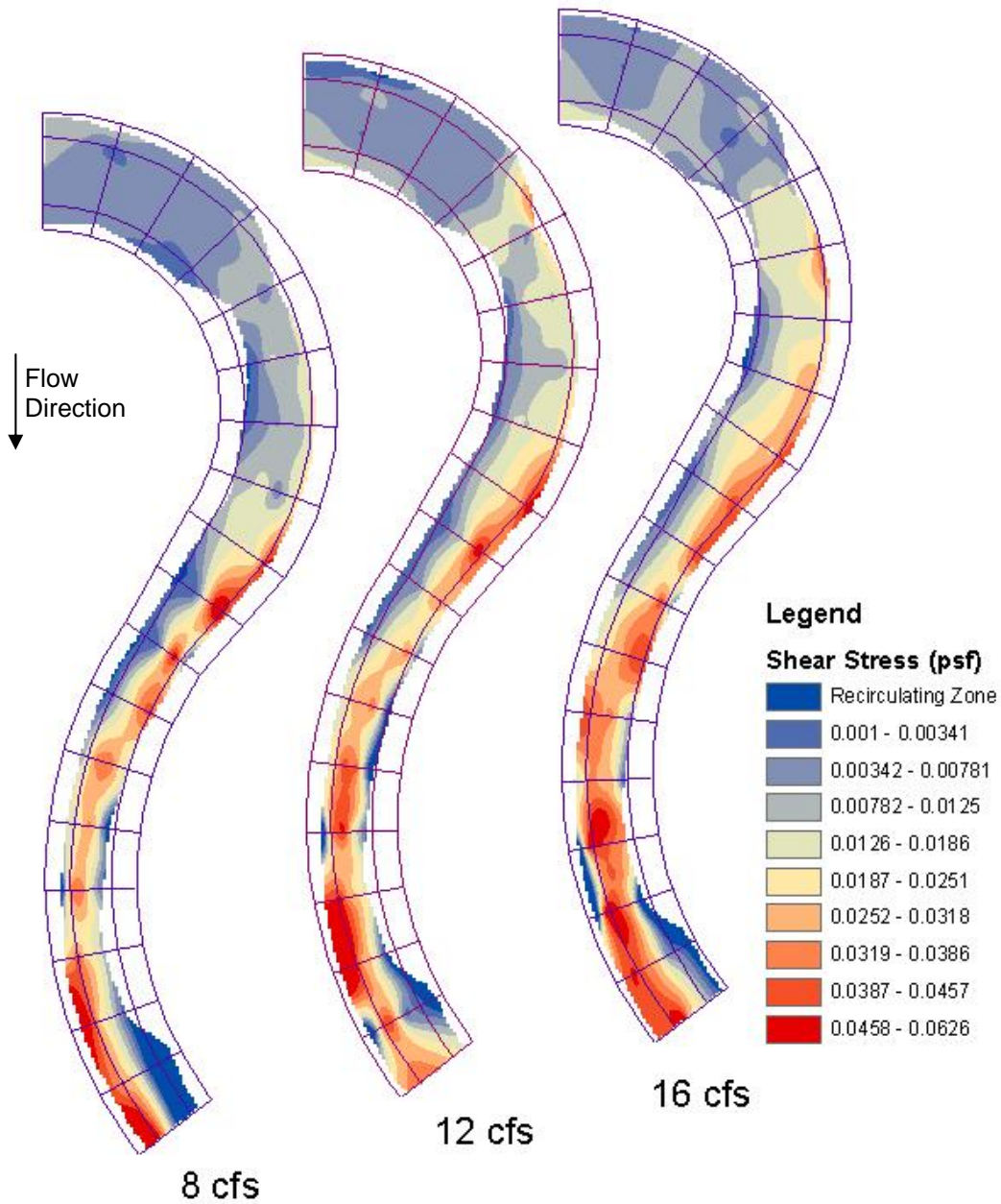
Figure 5.15: Shear Stress Distribution by Single Near-bed Value

5.4.2 Extrapolation

Extrapolation of points from trends discerned throughout the water column is well accepted for 2-D flows (Nikora and Goring (2000); see Section 2.3.4). While it is well noted that this method is sensitive to alignment errors (Nezu and Nakagawa 1993), the concept was used to see if trends existed in $\overline{u'w'}$ as well as $\overline{v'w'}$ despite the presence of secondary flows. Trends in

$\overline{u'w'}$ and $\overline{v'w'}$ were found for 73% and 48% of data-collection locations, respectively. Recirculating zones accounted for 14% of locations where trends in $\overline{u'w'}$ were not discernable. Figure 5.16 provides an example of extrapolation of the $\overline{u'w'}$ Reynolds stress component. Trends in $\overline{v'w'}$ were found, where secondary circulation existed as this component is related to the circulation cells (Blanckaert and Graf 2001). Due to the complex nature of the $\overline{v'w'}$ trends, linear interpolation was conducted for values below a relative depth of 0.5, as seen in Figure 5.17. The negative shear stress value seen in Figure 5.17 is due to the probes coordinate system and is accounted for in determining the resultant shear. Accelerating, decelerating (Song 1994), and secondary flows (Shiono and Muto 1998) were observed in $\overline{u'w'}$ trends and were accounted for by extrapolating trends in the lower portion of the water column to prevent skewing of results. The average coefficient of agreement for $\overline{u'w'}$ and $\overline{v'w'}$ were 0.815 and 0.71, respectively.
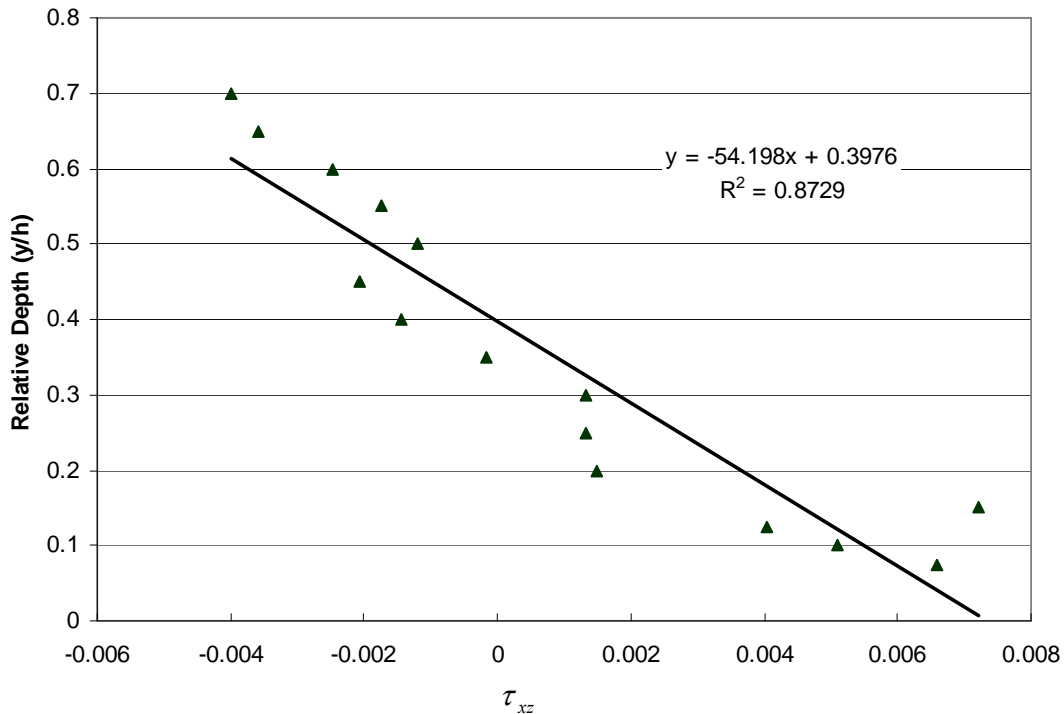
Figure 5.16: Extrapolation Technique for the $\overline{u'w'}$ Component (psf)
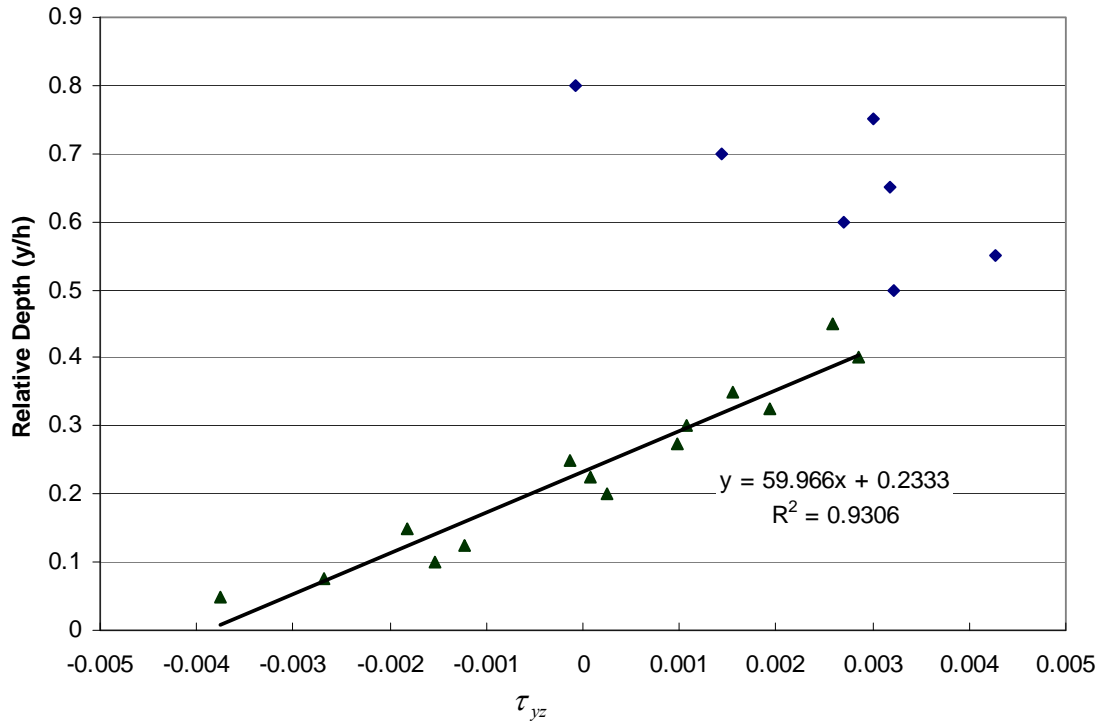
Figure 5.17: Extrapolation Technique Used for the $\overline{v'w'}$ Component (psf)

Shear stresses were calculated at locations where both components exhibited trends and extrapolations were conducted. Figure 5.18 presents resulting shear stress distribution using the extrapolation technique with identified applicable testing locations.
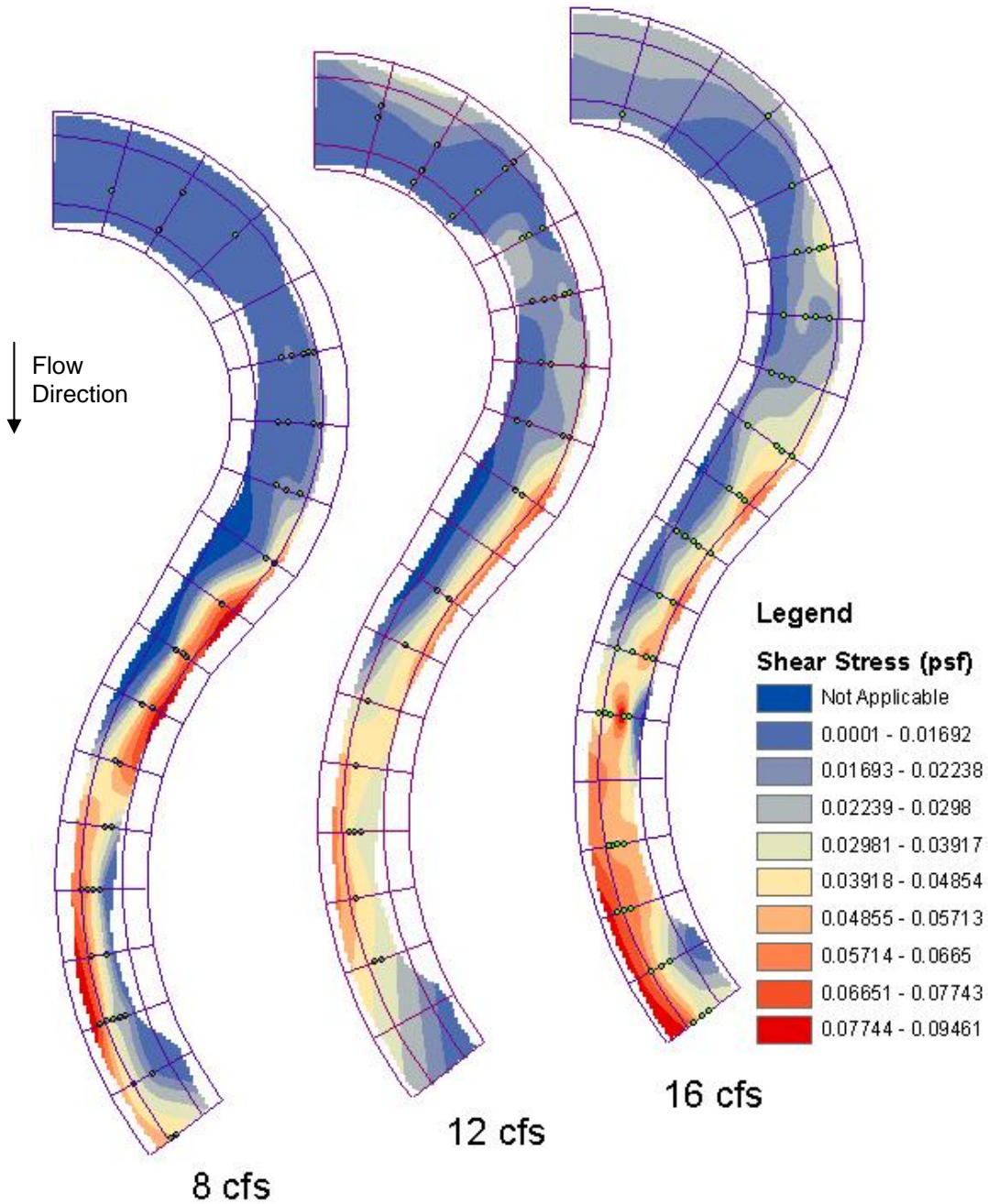
Figure 5.18: Shear Stress Distributions for Reynolds – Extrapolation Technique

Extrapolating profiles to the bed resulted in increases in shear stress compared to use of a near-bed point measurement. Increases were expected due to extrapolation accounting for increases in shear stress as a result of bed roughness as suggested by Biron *et al*. (2004). Comparisons between the resultant for near-bed and extrapolation techniques is presented in

Figure 5.19. Scatter can be attributed to the height of the roughness sublayer, which changes the height of maximum Reynolds stress.
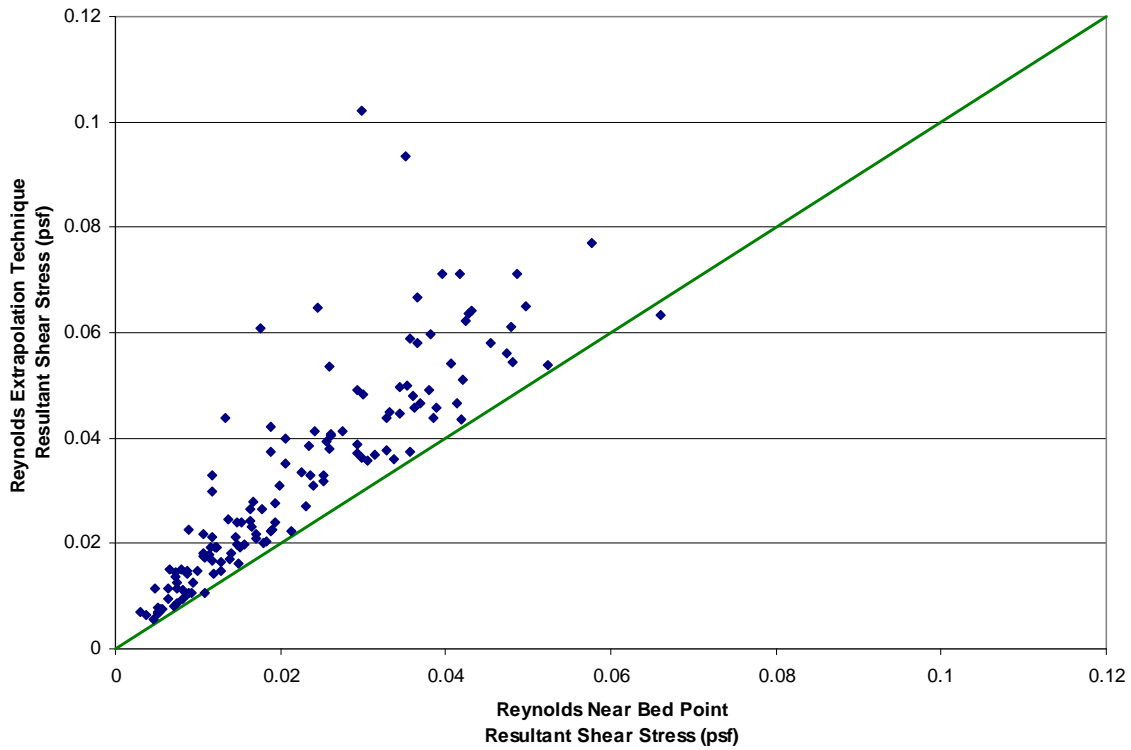
Figure 5.19: Comparison of Near-bed and Extrapolation Techniques for Reynolds Shear Stress Approximations

5.5   Turbulent Kinetic Energy

The TKE approach for estimating bed shear stress was evaluated for all discharges utilizing single near-bed point measurements. A relative depth of 0.1 was determined to provide the most accurate results for Biron *et al*. (2004) and was, therefore, used for this study. Near-bed ADV points used in the Reynolds near-bed procedure were used for the TKE method. Use of the TKE method assumes a proportionality constant used in oceanographic studies is applicable in a fluvial environment and that shear stresses can be determined from a near-bed value. Biron *et al*. (2004) found the method appropriate in complex flows, while suggesting verification of the proportionality constant and applicable relative depth.   Tilston (2005) found the method appropriate in field tests of shear stress of a meandering bend. Bed shear stresses using the TKE method were determined by Equation 2.34.   Results of the TKE energy method for each discharge are presented in Figure 5.20.

Flow
Direction

Legend

Shear Stress (psf)

■	Not Applicable
■	0.0001 - 0.001
■	0.001001 - 0.003279
■	0.00328 - 0.007769
■	0.00777 - 0.01338
■	0.01339 - 0.02012
■	0.02013 - 0.02797
■	0.02798 - 0.0392
■	0.03921 - 0.05715
■	0.05716 - 0.09868

16 cfs

12 cfs

8 cfs
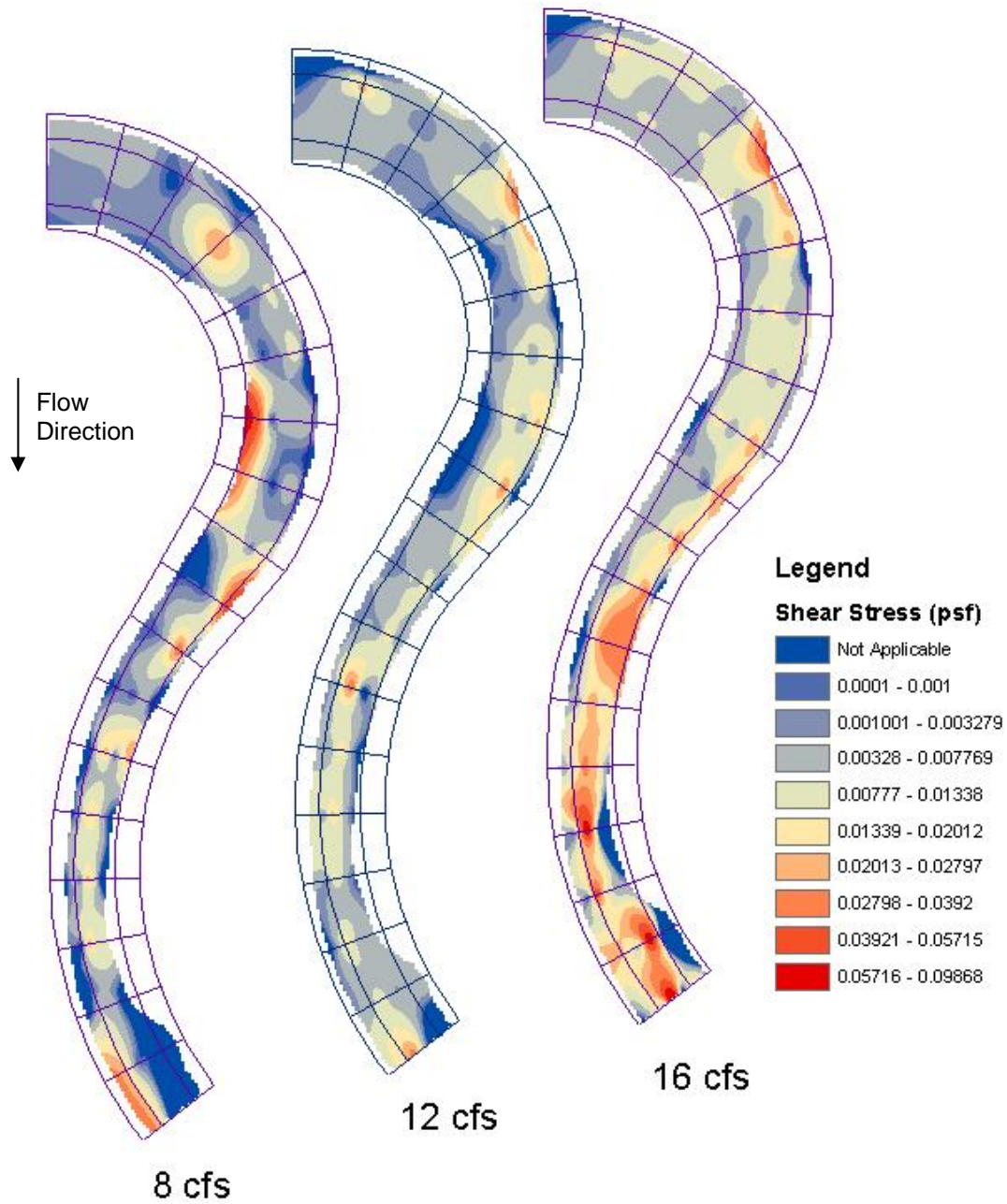
Figure 5.20: Shear Stress Distributions by the TKE Method

6 RESULTS

Comparisons of methods for estimating shear stress are presented followed by discussions of applicability and comparisons with distributions found by others. Differences in magnitude and distribution are presented by way of graphical comparison. Maximum values for each method and bend are compared to approach shear estimates to illustrate increases in shear stress due to secondary flows and native topographic features and are further compared to findings by others.

6.1 Method Comparisons and Discussion

Method comparisons demonstrate similarities in shear stress distributions and disagreement in resulting magnitudes. Figure 6.1 through Figure 6.3 present plan view comparisons of shear stress estimates by method with consistent scaling for each discharge tested. It should be noted that the Preston tube and law of the wall estimates are results from the primary shear component only. Boundary shear stress distributions by all methods except TKE follow a similar trend where shear stress is high on the outer banks downstream of the bend apex and on the inner bank at the bend entrance. Figure 2.10 was used as a guideline for comparison of expected shear stress distributions.

Flow
Direction

Legend

Shear Stress (psf)

	< 0.001
	0.001 - 0.0189
	0.019 - 0.0546
	0.0547 - 0.0903
	0.0904 - 0.126
	0.127 - 0.162
	0.163 - 0.198
	0.199 - 0.233
	0.234 - 0.269
	0.27 - 0.305
	0.306 - 0.34
	0.341 - 0.376

TKE   Reynolds (Near Bed Point)   Reynolds (Extrapolated)   Law of the Wall   Preston Tube
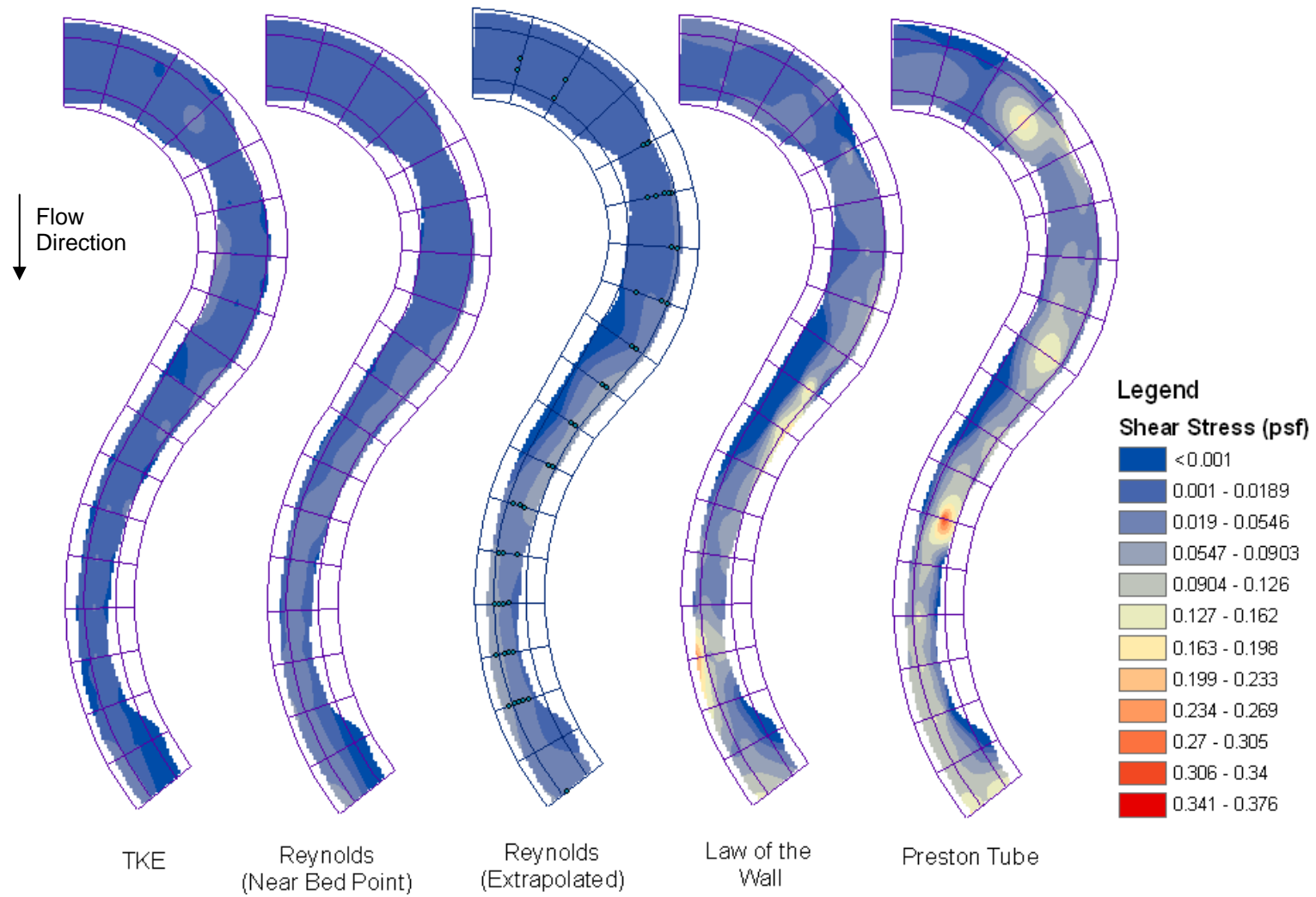
Figure 6.1: Method Comparisons in Plan View (8 cfs)

Flow Direction

TKE

Reynolds (Near Bed Point)

Reynolds (Extrapolated)

Law of the Wall

Preston Tube

Legend
Shear Stress (psf)

	< 0.00289
	0.00289 - 0.0298
	0.0299 - 0.0516
	0.0517 - 0.0752
	0.0753 - 0.0987
	0.0988 - 0.126
	0.127 - 0.154
	0.155 - 0.183
	0.184 - 0.213
	0.214 - 0.243
	0.244 - 0.275
	0.276 - 0.321
	0.322 - 0.376
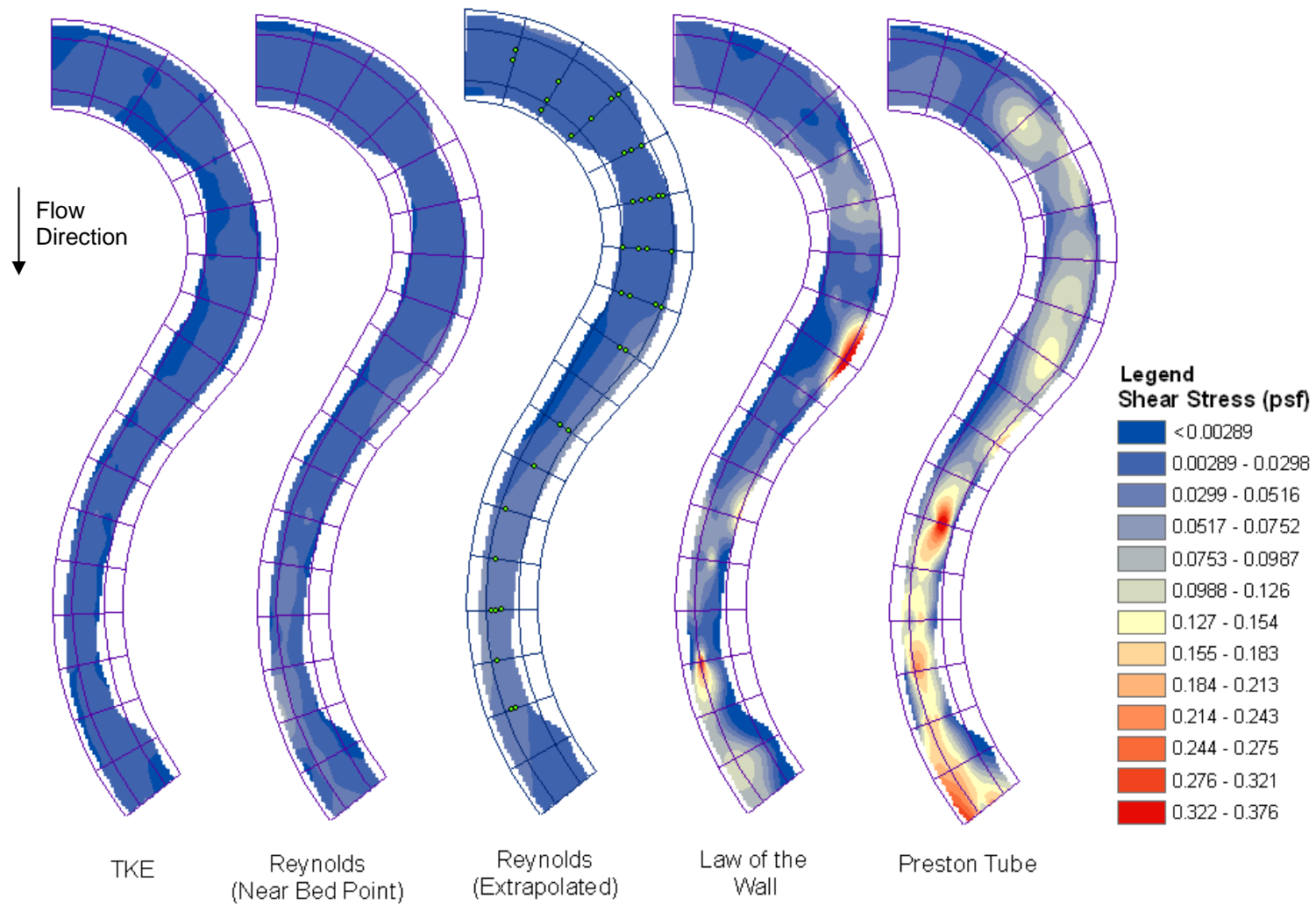
Figure 6.2: Method Comparisons in Plan View (12 cfs)

Flow
Direction

Legend
Shear Stress (psf)
< 0.001
0.001 - 0.0189
0.019 - 0.0546
0.0547 - 0.0903
0.0904 - 0.126
0.127 - 0.162
0.163 - 0.198
0.199 - 0.233
0.234 - 0.269
0.27 - 0.305
0.306 - 0.34
0.341 - 0.376

TKE   Reynolds (Near Bed Point)   Reynolds (Extrapolated)   Law of the Wall   Preston Tube
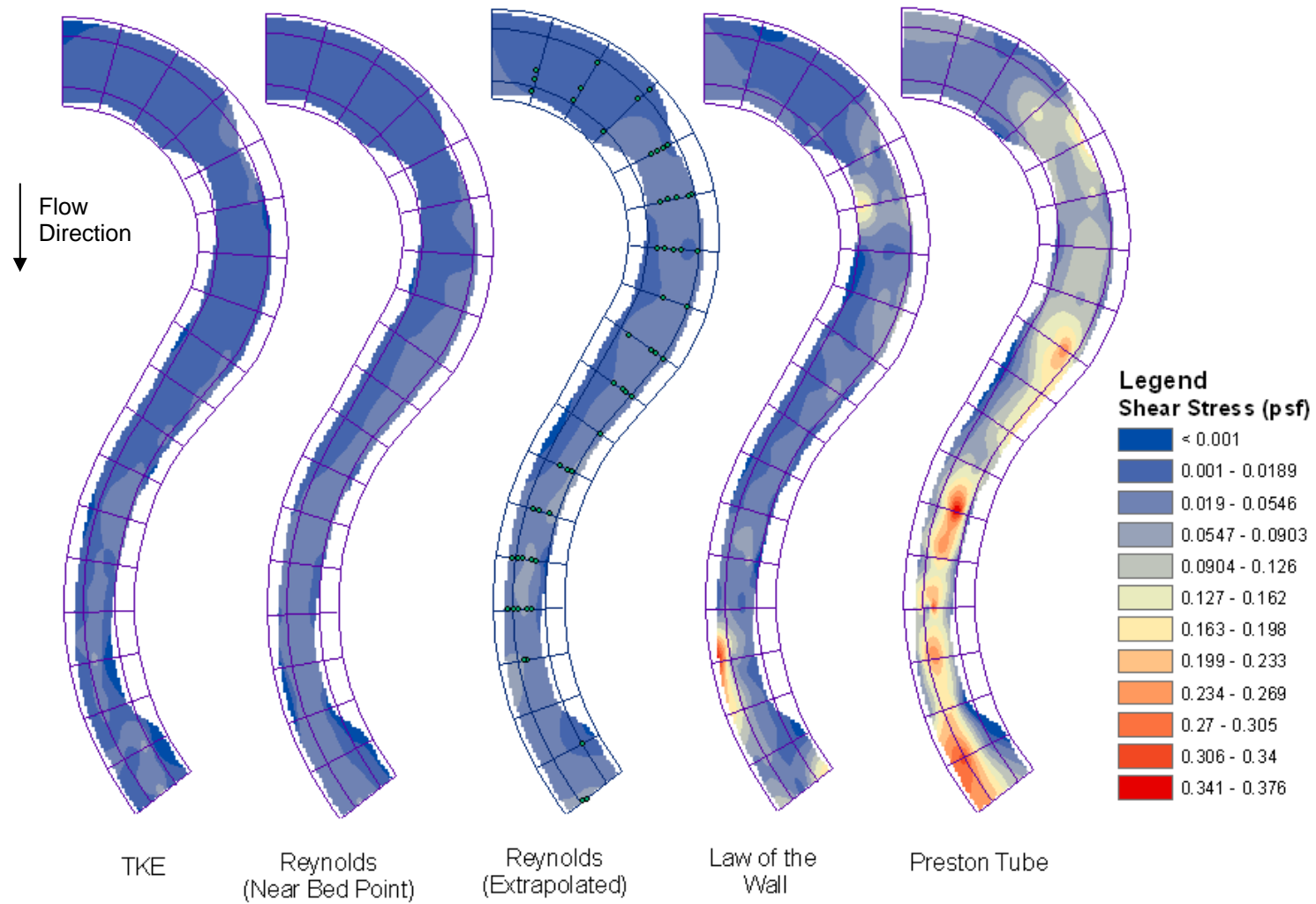
Figure 6.3: Method Comparisons in Plan View (16 cfs)

Disagreement between methods is primarily in the resulting magnitude of shear stress estimates. Figure 6.4 and Figure 6.5 illustrate maximum shear stress estimates per method for the upstream and downstream bends, respectively, without regard to shear components. Preston tube and law of the wall methods resulted in the highest maximum boundary shear stresses, while the TKE and near-bed point Reynolds methods were less than 1-D numerical model results. Differences can be attributed to sources of error and assumptions made for each method.
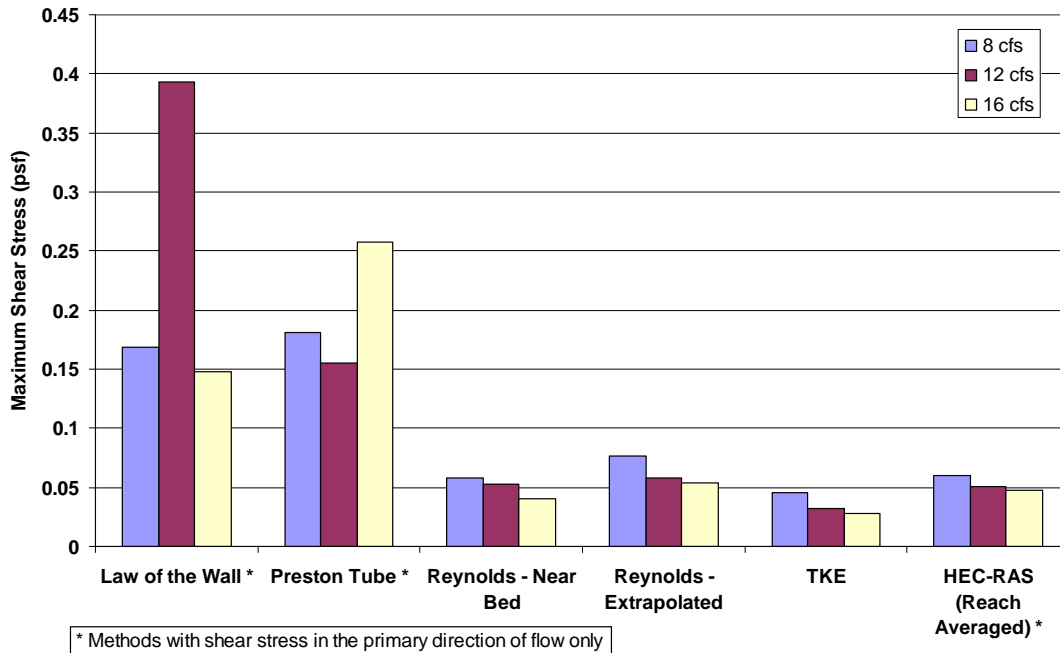
Figure 6.4: Upstream Bend Maximums per Method
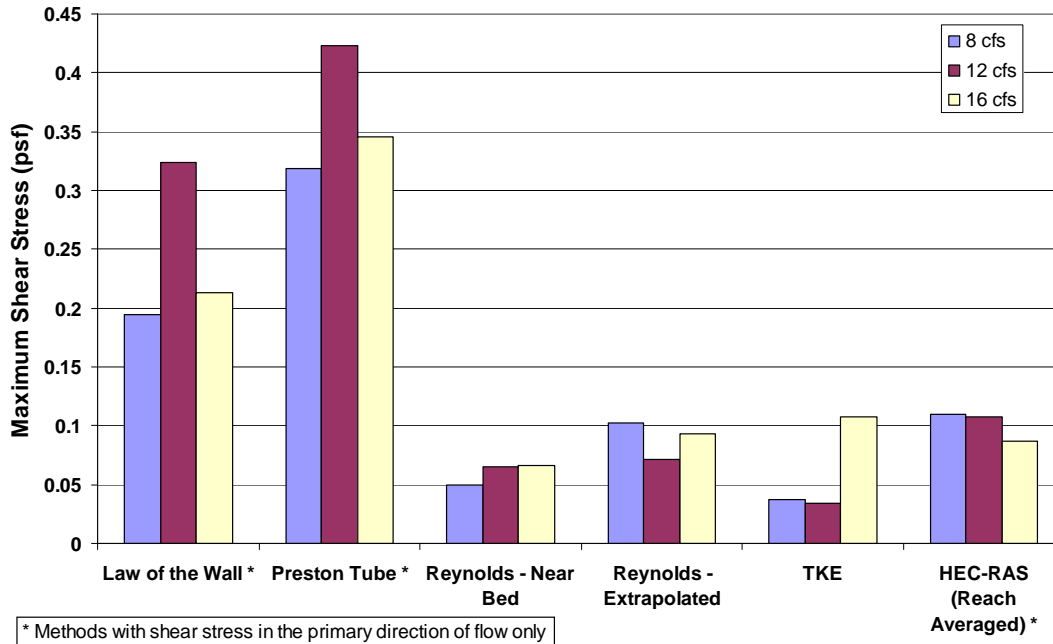
Figure 6.5: Downstream Bend Maximums per Method

Error associated with the law of the wall can be attributed to many possible sources of error. Subjectivity in determining applicable data for regression (Biron *et al*. 1998, Afzalimehr and Rennie 2009, Kendall and Koochesfahani 2008) and questionable application in complex flows (Yen 1965, Brown 1988, Knight and Shiono 1990, Biron *et al*. 2004, Tilston 2005, Wang and Cheng 2005) make application of the law of the wall questionable for this study. The location for maximum shear stress in the upstream bend for the 12-cfs discharge (Cross Section 8, Location a) was isolated for further review as the estimate appears questionable due to the marked localized increase in shear stress. Figure 6.6 illustrates the difference in shear stress estimates from addition or removal of the near-bed point resulting in significant differences in the estimation of shear stress. Analysis conducted was focused on data below a relative depth of 0.2. Shear stress estimates for including and excluding the near-bed point are 0.393 and 0.146 psf, respectively.
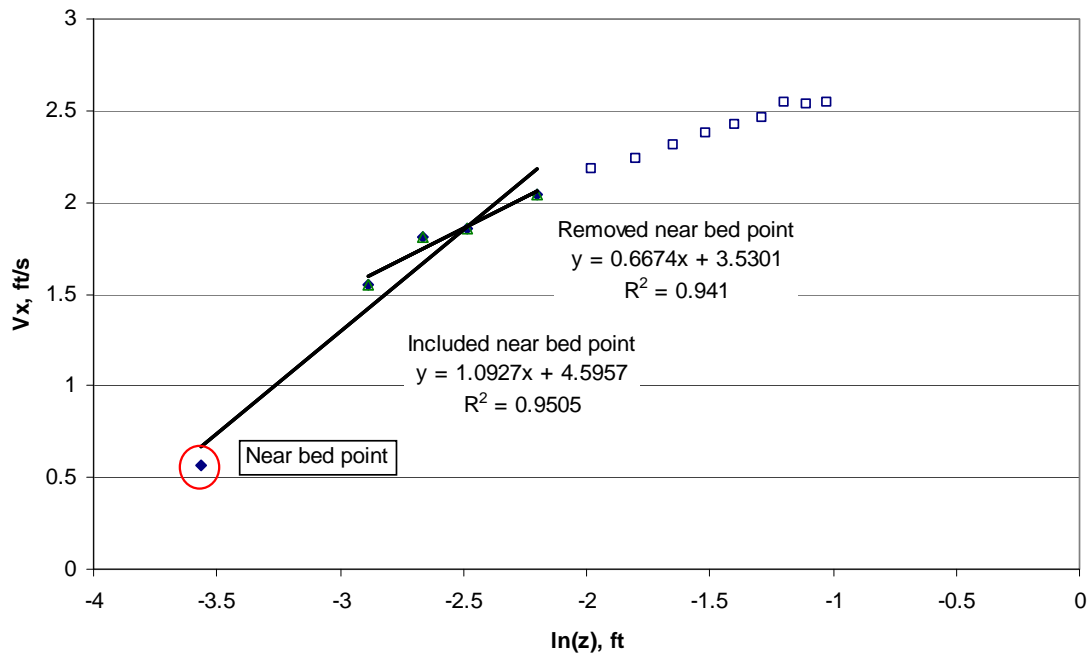
Figure 6.6: Comparison of Possible Shear Stress Estimates at a Location of Maximum Shear Stress (12 cfs, Cross Section 8, Location a)

Shear stress estimate errors from the Preston tube can be attributed to several sources. Local disturbances from individual roughness particles may be a source of error as the Preston tube's outer wall thickness is approximately 0.078 in. and roughness particles are approximately 0.25 in. Error due to roughness particles would have been present during development of the calibration equation, which illustrated an average percent error of 11.5%. Ippen *et al.* (1962) found error for their rough boundary test to be on the order of 15% by examination of data collected during calibration. Additionally, error may have been introduced by air bubbles in lines connecting the pressure transducer to the Preston tube. Air in connection tubing has been found to affect measurements and may have been present despite rigorous checks of the zero differential pressure. Alternatively, the Preston tube is well adapted for flows where misalignment errors are likely. Ippen *et al.* (1962) found a 15º misalignment contributed to an error of only 3.4%. Approximately 93% of velocities measured with the ADV in this study were less than 15º off alignment with the stream-wise direction. Despite possible sources of errors, the Preston tube does illustrate distributions consistent with Figure 2.10 with high shear on the convex bank at the bend entrance and concave bank downstream of the apex of the second bend.

Preston tube measurements were, in general, greater than estimates from the law of the wall in location comparisons as seen in Figure 6.7.
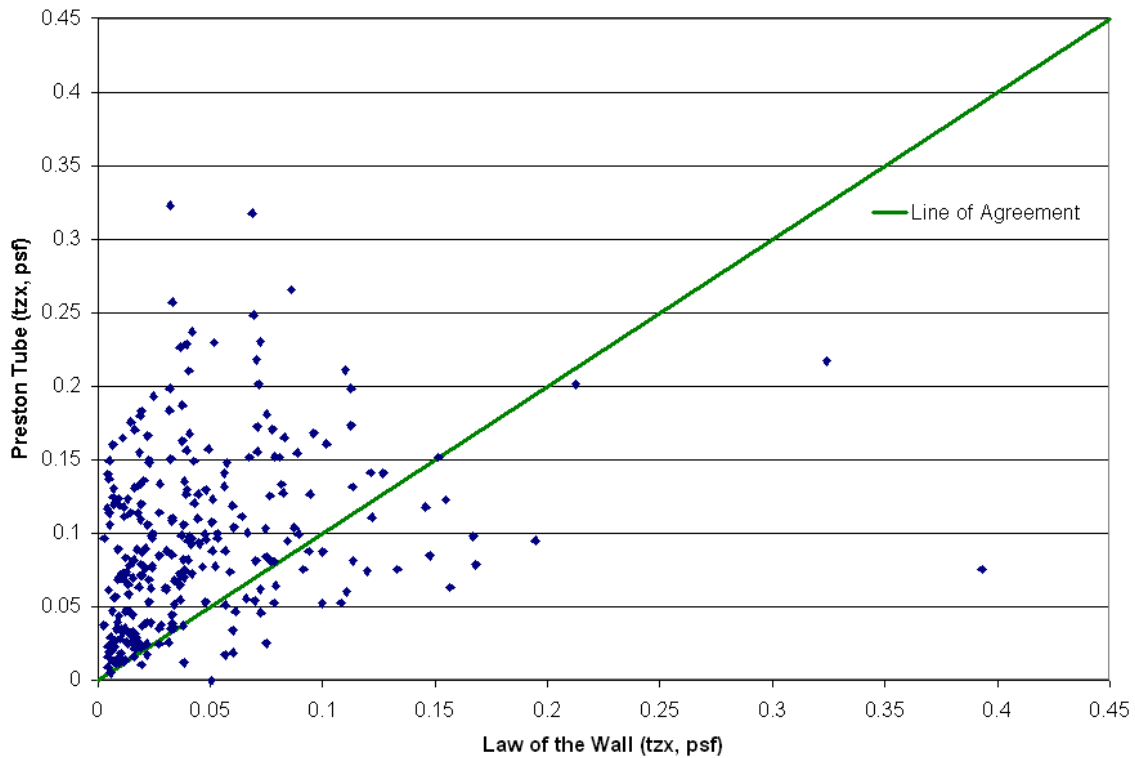
Figure 6.7: Comparison of Law of the Wall and Preston Tube Results

Reynolds near-bed and extrapolation techniques are limited in application in the presence of secondary flows. Near-bed point measurements resulted in shear stress estimates less than the extrapolation technique, which accounts for expected increases in shear stress (Biron *et al*. 2004). Additionally, the height of the roughness sublayer varied, possibly increasing or decreasing the resulting boundary shear stress for the near-bed point technique. Extrapolation, where trends existed for both components, tended to be in locations where secondary currents were present providing a limited database. Results from Reynolds stress methods were less than the Preston tube and law of the wall, which was contrary to an expected increase due to inclusion of transverse shear. Differences may be attributed to assumptions made for Reynolds stress techniques or possible sources of error associated with the Preston tube and law of the wall methods. Turbulent Reynolds stress methods illustrate shear stress distributions consistent with current design guidelines by the FHWA illustrated in Figure 2.10.

TKE results are inconsistent with distributions in Figure 2.10 and results from other methods examined in this study. Inconsistent high shear stress locations were on the inner banks downstream of the second bend apex for the 16-cfs testing configuration and on the inner bank to the first bend for the 8-cfs testing configuration as shown in Figure 5.20. Locations of discrepancy were locations of recirculation, where high turbulence existed but not in an effective direction. TKE also yielded maximum shear stress values smaller than any other method, as seen in Figure 6.4 and Figure 6.5. Distributions were reasonable for the 12-cfs testing configuration as seen in comparison with Reynolds shear stress distribution presented in Figure 6.8. Questionable application of TKE in fluvial environments and low shear stress results suggest the need for reevaluation of the proportionality constant as well as the proper applicable relative depth as suggested by Biron *et al*. (2004).
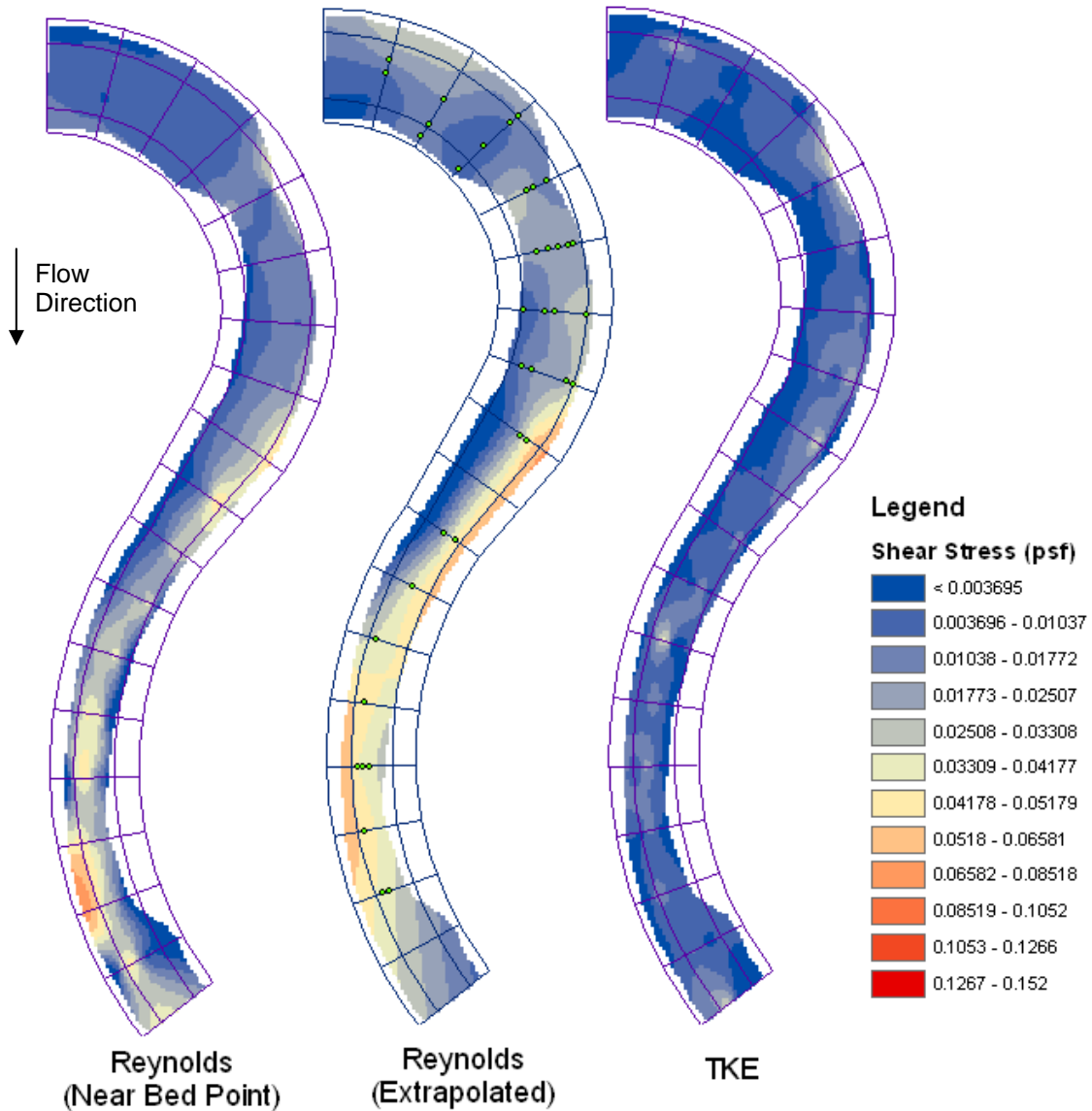
Figure 6.8: Comparisons between Reynolds and TKE Methods (12 cfs)

6.2 Comparison of Bend Maximums

Ippen *et al*. (1962) quantified the relationship between relative curvature (R_c/T_w) and increases in shear stress found in trapezoidal bends with respect to the approach shear stress. Since Ippen *et al*. (1962), other researchers have also provided results supplementing this work, which have been used as a basis for providing practitioners guidelines for increasing erosion countermeasures in bends (USACE 1970). To supplement this work, increases in shear stress found in this study were calculated and compared to findings by others.

87

Relative increases in shear stress were determined for each method and bend. Ratios of maximum shear stress in the bend (τ_m) to approach shear stresses by each method are presented in Table 6.1. Approach shear stress estimates ($\overline{\tau}_{app}$) were determined with results for each method to provide consistency in expected increases and remove method bias. Determination of approach shear stress was similar to that of Ippen and Drinker (1962) who determined approach shear by Equation 6.1. Additionally, adjoining representative cross sections were averaged to reduce impact of possible individual estimate errors. Cross Sections 1 and 2 were averaged for the upstream bend and Cross Sections 10 and 11 for the downstream bend for approach shear stress estimates presented in Table 6.2. Reynolds extrapolation and law of the wall results were removed from analysis due to insufficient results in approach sections:

$$\overline{\tau}_o = \left(\frac{1}{P_w} \int_{P_w} \tau_o dP \right)$$
Equation 6.1

where

$\overline{\tau}_o$ = mean measured shear stress [$ML^{-1}T^{-2}$];

P_w = wetted perimeter [L];

τ_o = measured shear stress [$ML^{-1}T^{-2}$]; and

dP = differential pressure measured from Preston tube [L].

Table 6.1: Relative Shear Stress and Relative Curvatures for Each Bend and Discharge

Discharge (cfs)	Method	Upstream τ_{max}/τ_{app}	Downstream τ_{max}/τ_{app}	Upstream R_c/T_w	Downstream R_c/T_w
8	Preston Tube	11.6	3.4	3.9	8.0
8	Reynolds – Near-bed	12.9	2.2	3.9	8.0
8	TKE	16.6	4.5	3.9	8.0
8	HEC-RAS	7.5	3.7	3.9	8.0
12	Preston Tube	6.6	5.3	3.8	7.7
12	Reynolds – Near-bed	7.9	3.5	3.8	7.7
12	TKE	6.0	5.4	3.8	7.7
12	HEC-RAS	4.8	2.9	3.8	7.7
16	Preston Tube	11.0	4.3	3.7	7.3
16	Reynolds – Near-bed	6.1	3.5	3.7	7.3
16	TKE	5.2	17.0	3.7	7.3
16	HEC-RAS	3.7	1.9	3.7	7.3

Average approach shear ($\overline{\tau}_{app}$) was determined from Cross Sections 1 and 2 for the upstream bend and Cross Sections 10 and 11 for the downstream bend.

Table 6.2: Averaged Approach Shear Stress Estimates for Each Method

Discharge (cfs)	Method	Upstream $\overline{\tau}_{app}$ (psf)	Downstream $\overline{\tau}_{app}$ (psf)
8	Preston Tube	0.0155	0.0937
8	Reynolds – Near-bed	0.0045	0.0223
8	TKE	0.0028	0.0083
8	HEC-RAS	0.008	0.030
12	Preston Tube	0.0233	0.0801
12	Reynolds – Near-bed	0.0066	0.0186
12	TKE	0.0055	0.0064
12	HEC-RAS	0.011	0.037
16	Preston Tube	0.0311	0.1213
16	Reynolds – Near-bed	0.0076	0.0252
16	TKE	0.0080	0.0171
16	HEC-RAS	0.013	0.045

A comparison of results to findings by others is given in Figure 6.9 with the law of the wall, TKE, and Reynolds methods removed due to limitations identified in Section 6.1. The marked increase of relative shear stress in this study is attributed, in large part, to native topographic features that were not present in previous investigations (USBR 1964, Ippen *et al.* 1960, 1962, Yen 1965, Sin 2010).
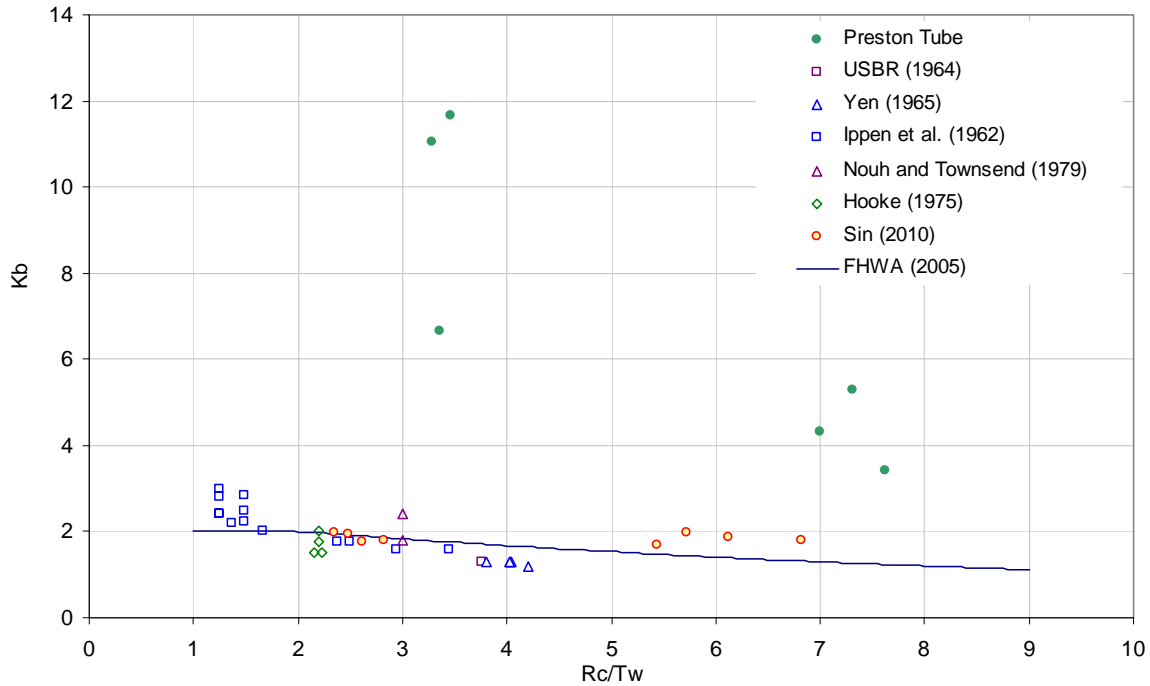
Figure 6.9: Comparison of Shear Stress Increases for Each Bend ($\tau_{max} / \overline{\tau}_{app}$)

Regression utilizing Preston tube measurements was conducted to determine an equation that may be applicable for design purposes and an upper envelope equation is given to provide a probable maximum, as seen in Figure 6.10. Equation 6.2 and Equation 6.3 provide the regression and upper envelope equations, respectively:

$$K_b = 26.1 \left(\frac{R_c}{T_w} \right)^{-0.88} \qquad \textbf{Equation 6.2}$$

$$K_b = 43.2 \left(\frac{R_c}{T_w} \right)^{-1.06} \qquad \textbf{Equation 6.3}$$

where

K_b = relative shear stress [dimensionless];

R_c = radius of curvature [L]; and

T_w = channel top width [L].
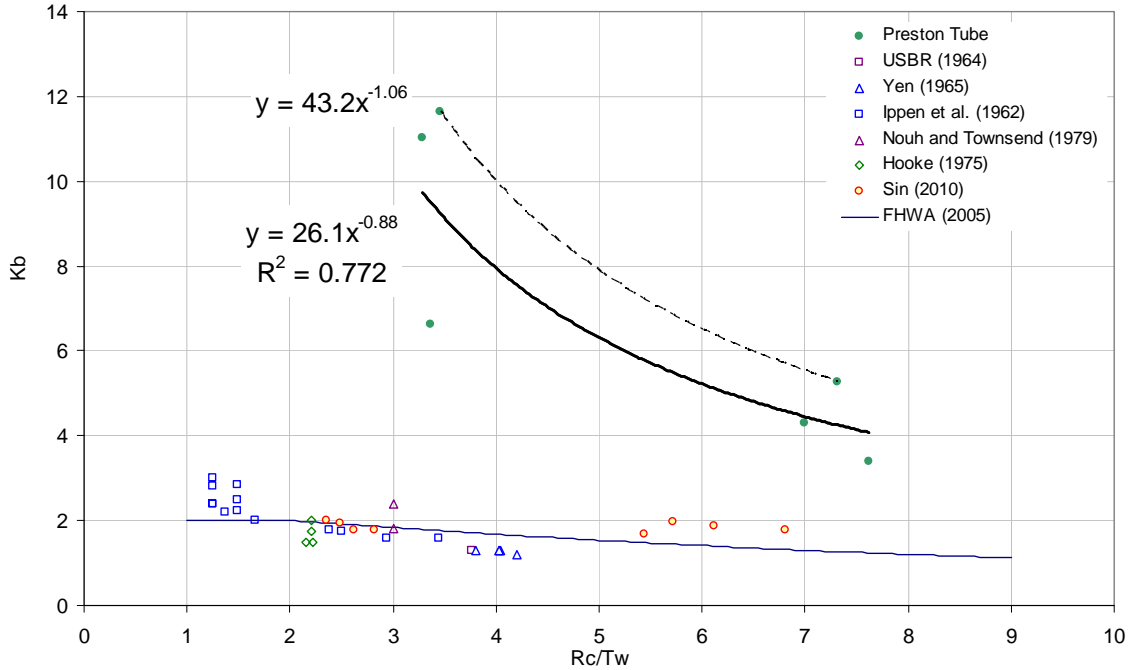
Figure 6.10: K_b **Determined with Approach Estimates from the Preston Tube**

Findings presented in Figure 6.10 suggest a large difference between increases in shear stress from a bend with native topographic features and a bend with a constant trapezoidal cross section. Equation 2.4 provided by the FHWA (2005) for determining increases in shear stress due to bends with trapezoidal cross sections depicted in Figure 6.10 was used to determine the possible percent increase caused by natural topographic features. Equation 6.3, the upper envelope equation, was used for comparison. Figure 6.11 presents the percent increase in K_b from trapezoidal to natural topographic features calculated by Equation 6.4:

$$\varepsilon = \frac{K_{b,NT} - K_{b,TRAP}}{K_{b,TRAP}} \cdot 100 \qquad \textbf{Equation 6.4}$$

where

ε = percent increase;

$K_{b,NT}$ = shear stress multiplier for natural topography [dimensionless]; and

$K_{b,TRAP}$ = shear stress multiplier for trapezoidal channels [dimensionless].

91
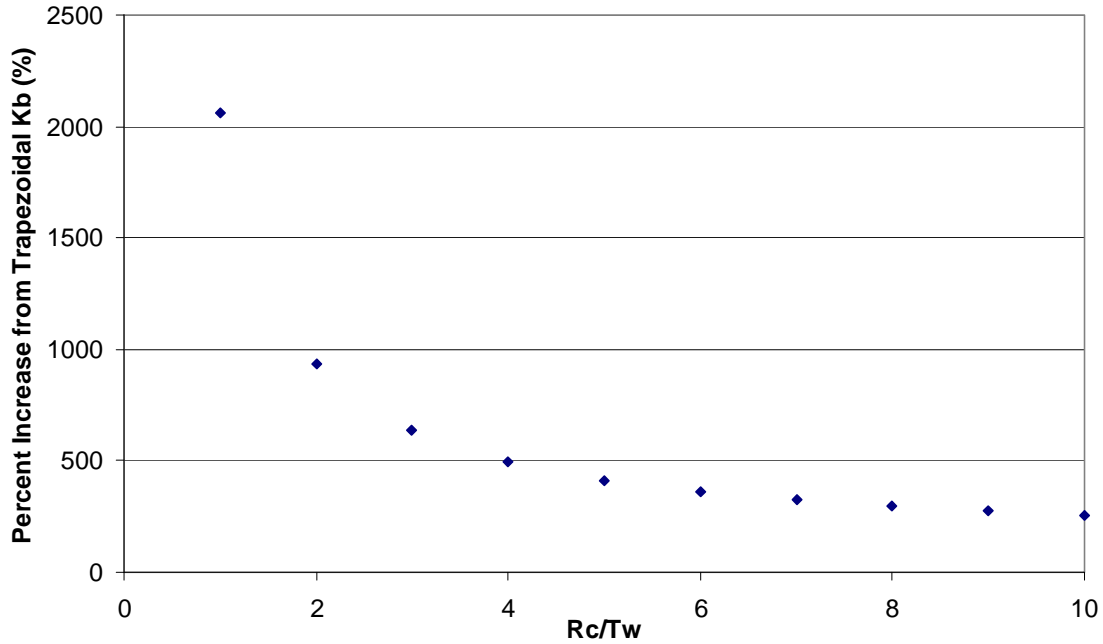
Figure 6.11: Percent Increase in K_b from Prismatic to Native Topography

6.2.1 Comparisons to HEC-RAS

Relative shear stress (K_b) was determined utilizing approach estimates from HEC-RAS to present possible increases from 1-D approximations. Table 6.3 provides results for each method where approach estimates from HEC-RAS were used. Maximum HEC-RAS results in bends account for changes in topography as well as differences in lengths for the right bank, left bank, and channel centerline but does not calculate increases due to secondary flows. Therefore, approach estimates from HEC-RAS are considered comparative to straight channel approximations often used in practice.

Table 6.3: Relative Shear Stress with HEC-RAS Approach Estimates

Discharge (cfs)	Method	Bend	$\bar{\tau}_{appHEC-RAS}$ (psf)	R_c/T_w	$\tau_{max}/\tau_{appHEC-RAS}$
8	Law of the Wall	Upstream	0.008	3.5	21.1
8	Preston Tube	Upstream	0.008	3.5	22.7
8	Reynolds – Near-bed	Upstream	0.008	3.5	7.2
8	Reynolds – Extrapolated	Upstream	0.008	3.5	9.7
8	TKE	Upstream	0.008	3.5	5.8
8	HEC-RAS	Upstream	0.008	3.5	7.5
8	Law of the Wall	Downstream	0.030	7.6	6.6
8	Preston Tube	Downstream	0.030	7.6	10.8
8	Reynolds – Near-bed	Downstream	0.030	7.6	1.7
8	Reynolds – Extrapolated	Downstream	0.030	7.6	3.5
8	TKE	Downstream	0.030	7.6	1.3
8	HEC-RAS	Downstream	0.030	7.6	3.7
12	Law of the Wall	Upstream	0.011	3.4	37.2
12	Preston Tube	Upstream	0.011	3.4	14.7
12	Reynolds – Near-bed	Upstream	0.011	3.4	5.0
12	Reynolds – Extrapolated	Upstream	0.011	3.4	5.5
12	TKE	Upstream	0.011	3.4	3.1
12	HEC-RAS	Upstream	0.011	3.4	4.8
12	Law of the Wall	Downstream	0.037	7.3	8.8
12	Preston Tube	Downstream	0.037	7.3	11.5
12	Reynolds – Near-bed	Downstream	0.037	7.3	1.8
12	Reynolds – Extrapolated	Downstream	0.037	7.3	1.9
12	TKE	Downstream	0.037	7.3	0.9
12	HEC-RAS	Downstream	0.037	7.3	2.9
16	Law of the Wall	Upstream	0.013	3.3	11.5
16	Preston Tube	Upstream	0.013	3.3	20.0
16	Reynolds – Near-bed	Upstream	0.013	3.3	3.2
16	Reynolds – Extrapolated	Upstream	0.013	3.3	4.2
16	TKE	Upstream	0.013	3.3	2.2
16	HEC-RAS	Upstream	0.013	3.3	3.7
16	Law of the Wall	Downstream	0.045	7.0	4.7
16	Preston Tube	Downstream	0.045	7.0	7.6
16	Reynolds – Near-bed	Downstream	0.045	7.0	1.5
16	Reynolds – Extrapolated	Downstream	0.045	7.0	2.1
16	TKE	Downstream	0.045	7.0	2.4
16	HEC-RAS	Downstream	0.045	7.0	1.9

Preston tube data presented in Table 6.3 were used for regression to determine increases in shear stress compared to 1-D approach approximations. Estimates from other methods were excluded due to limitations identified in Section 6.1. Relationships presented assume Preston

tube results represent accurate estimates of shear stress. Equation 6.5 and Equation 6.6 provide the regression and upper envelope equations, respectively:

$$K_{bHEC-RAS} = 50.2 \left(\frac{R_c}{T_w} \right)^{-0.82}$$
Equation 6.5

$$K_{bHEC-RAS} = 70.6 \left(\frac{R_c}{T_w} \right)^{-0.91}$$
Equation 6.6

where

$K_{bHEC-RAS}$ = relative shear stress with approach estimates from HEC-RAS (Figure 6.12) [dimensionless];

R_c = radius of curvature [L]; and

T_w = channel top width [L].
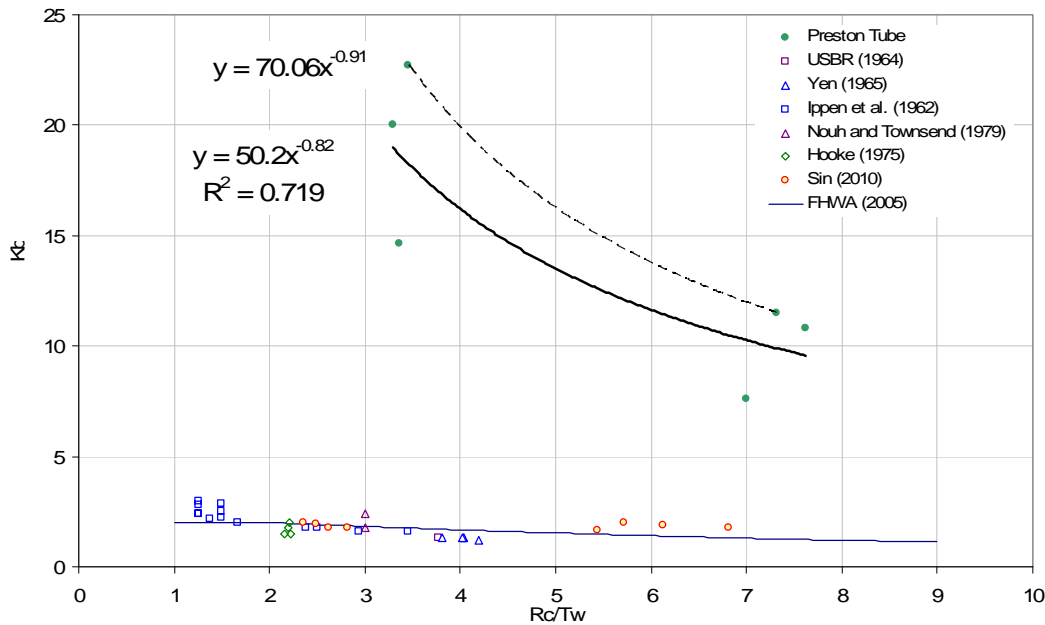
Figure 6.12: Relative Shear Stress with Approach Flow Shear from HEC-RAS

Ratios of maximum shear stress estimates per method to maximum HEC-RAS results in the bends are presented in Table 6.4 for each bend and discharge. Preston tube results exhibit expected increases as shear stress estimates in bends should be greater than results from a 1-D

model.   Figure 6.13 illustrates the ratio of Preston tube to 1-D model results with respect to relative curvature.

Table 6.4: Ratio of Maximum Shear Stress per Bend and Maximums from HEC-RAS

Discharge (cfs)	Bend	Law of the Wall / HEC-RAS	Preston Tube / HEC-RAS	Reynolds – Near-bed / HEC-RAS	Reynolds – Extrapolated / HEC-RAS	TKE / HEC-RAS
8	Upstream	2.82	3.04	0.97	1.29	0.77
8	Downstream	1.78	2.92	0.45	0.93	0.34
12	Upstream	7.77	3.06	1.04	1.15	0.64
12	Downstream	3.02	3.94	0.61	0.66	0.32
16	Upstream	3.08	5.36	0.85	1.13	0.59
16	Downstream	2.44	3.96	0.76	1.07	1.24
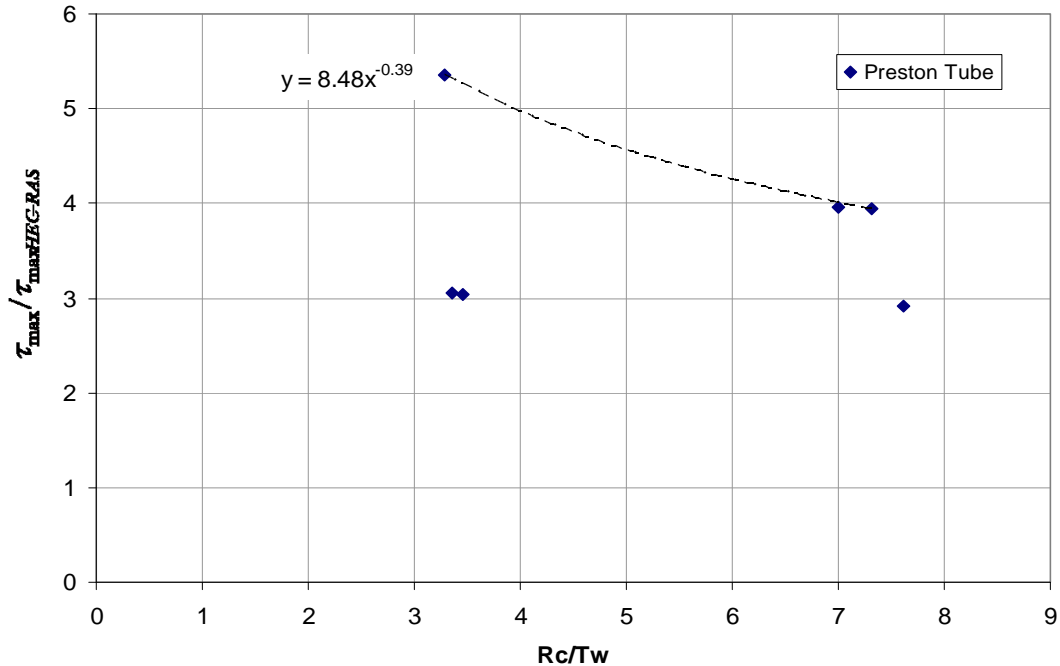
Figure 6.13: Comparison of Bend Maximums from HEC-RAS

6.2.2 Discussion of Shear Stress Increases

Shear stress increases resulting from native topographic features may be an important factor in relative migration rates of fluvial systems. Figure 6.14 presents relative migration rates from Hickin and Nanson (1984). It can be seen that maximum relative migration rates occur between a relative curvature of 2 and 4, the same location of maximum difference between

prismatic and natural topographic relative shear stresses. It is, therefore, suggested that scatter in the measured data by Hickin and Nanson (1984) can be attributed, in part, to topographic features of the channel and erosive or shear forces.
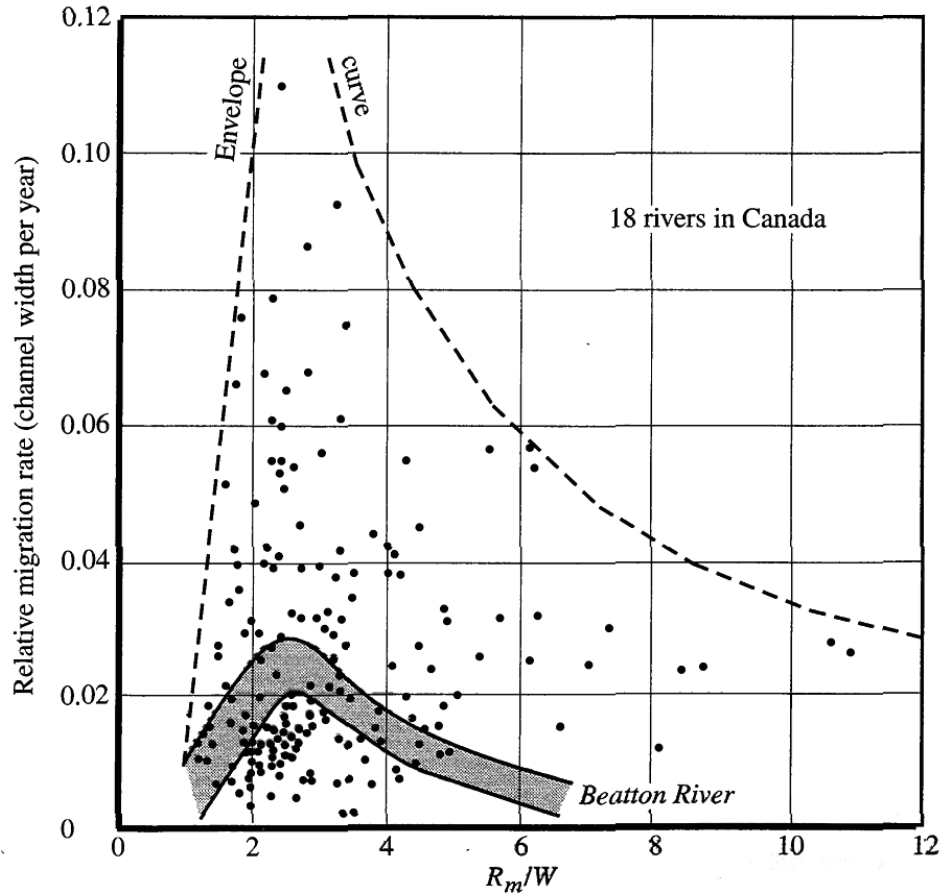
Figure 6.14: Relative Curvature and its Relation to Channel Migration Rates (Hickin and Nanson 1984)

6.3 Relative Velocities

Relative velocities were calculated in accordance with procedures for relative shear stress described in Section 6.2. Depth-averaged velocities were used for approach velocity estimates and maximum velocities were determined independent of depth. Table 6.5 presents a summary of measured and calculated velocities.

Table 6.5: Summary of Measured and Predicted Velocities

Discharge (cfs)	Bend	Measured Average Approach Velocity (ft/s)	HEC-RAS Average Approach Velocity (ft/s)	Maximum Measured Velocity in Bend (ft/s)	HEC-RAS Maximum Velocity in Bend (ft/s)	Relative Velocity – HEC-RAS	R_c/T_w
8	Upstream	0.93	0.85	3.07	2.08	3.62	3.46
8	Downstream	1.78	1.60	3.54	2.86	2.21	7.62
12	Upstream	1.10	1.01	3.02	1.98	2.99	3.36
12	Downstream	1.62	1.85	4.09	2.47	2.21	7.31
16	Upstream	1.08	1.14	2.86	2.08	2.51	3.29
16	Downstream	1.84	2.10	3.90	2.87	1.86	7.00

Figure 6.15 presents a comparison of measured and calculated approach velocity estimates with data provided in Table 6.5.

$$y = 1.0358x$$
$$R^2 = 0.8749$$
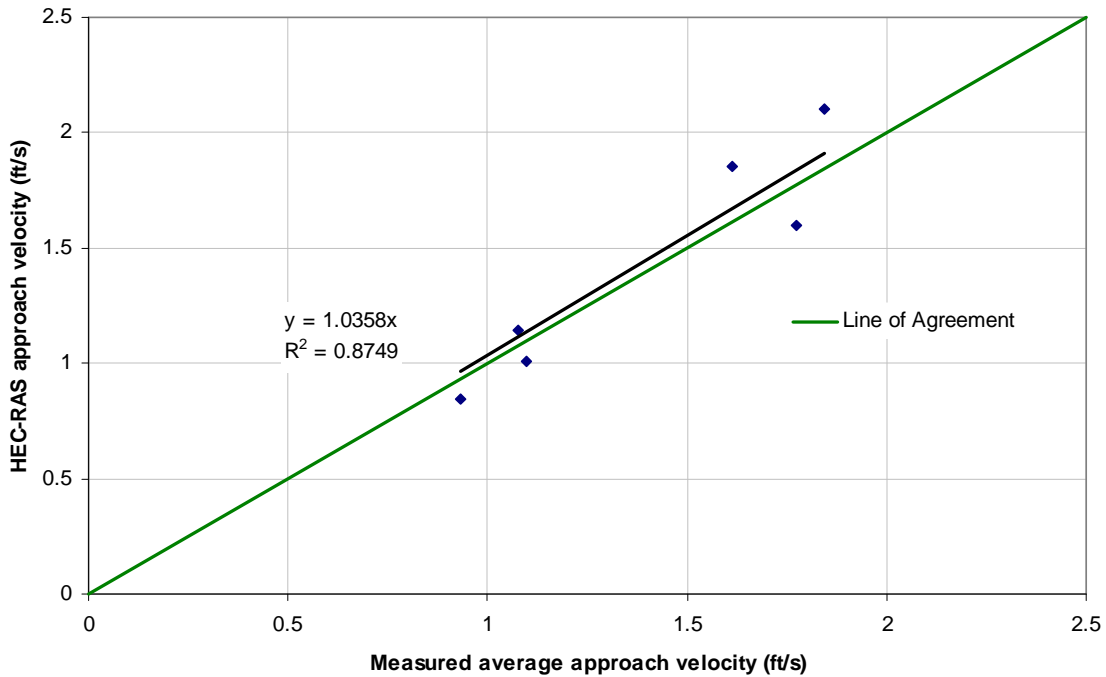
Figure 6.15: Comparison of Measured and HEC-RAS Average Approach Velocities

Velocity increases found in bends are correlated with relative curvature as presented in Figure 6.16, which provides results for relative velocities with approach estimates from HEC-RAS. Equation 6.7 and Equation 6.8 may be used to determine the increase in velocity found in bends with similar native topographic features given results from 1-D approach estimates:

$$V_b = 5.15\left(\frac{R_c}{T_w}\right)^{-0.45} \qquad\qquad \textbf{Equation 6.7}$$

$$V_b = 7.86\left(\frac{R_c}{T_w}\right)^{-0.62} \qquad\qquad \textbf{Equation 6.8}$$

where

V_b = velocity multiplier $\left(\dfrac{V_{max}}{V_{app}}\right)$ [dimensionless], where V_{max} = maximum velocity in

the bend [LT^{-1}] and V_{app} = average approach velocity to the bend [LT^{-1}];

R_c = radius of curvature [L]; and

T_w = channel top width [L].
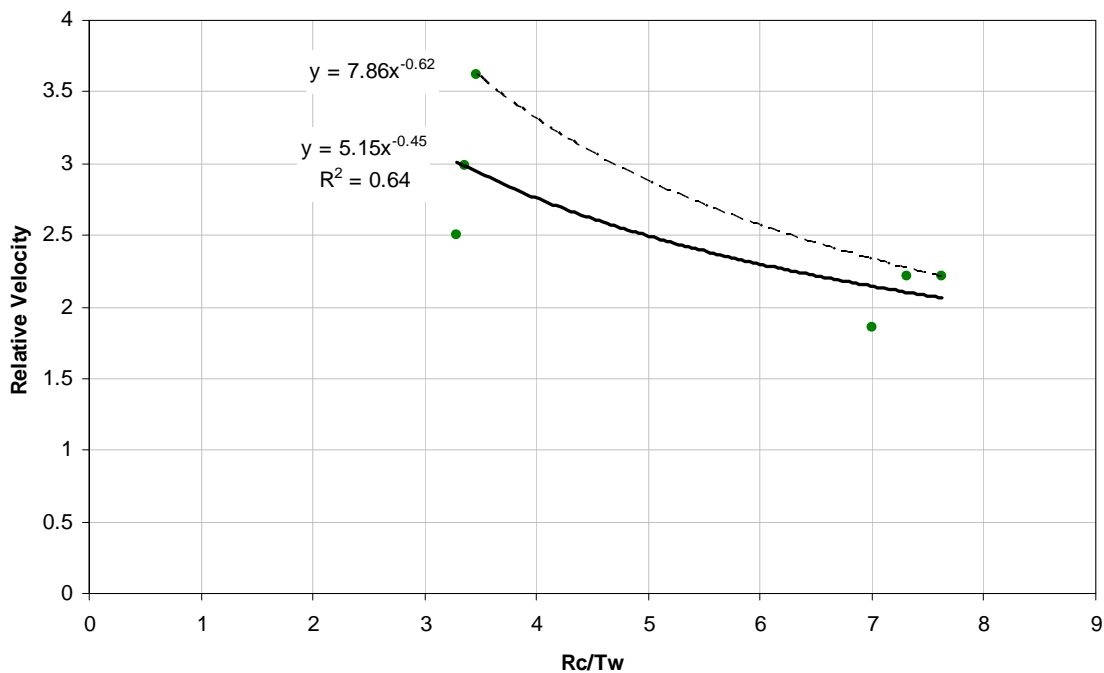
Figure 6.16: Relative Velocity Estimates with HEC-RAS Estimates in the Approach

Comparison of measured maximum velocity estimates in the bend and calculated estimates may be useful for practical application. Figure 6.17 presents the ratio of measured and calculated maximum velocities with respect to relative curvature. Ratios presented suggest a multiplier of 1.5 to 1.7 may be applied to 1-D model results for all ranges of relative curvature.
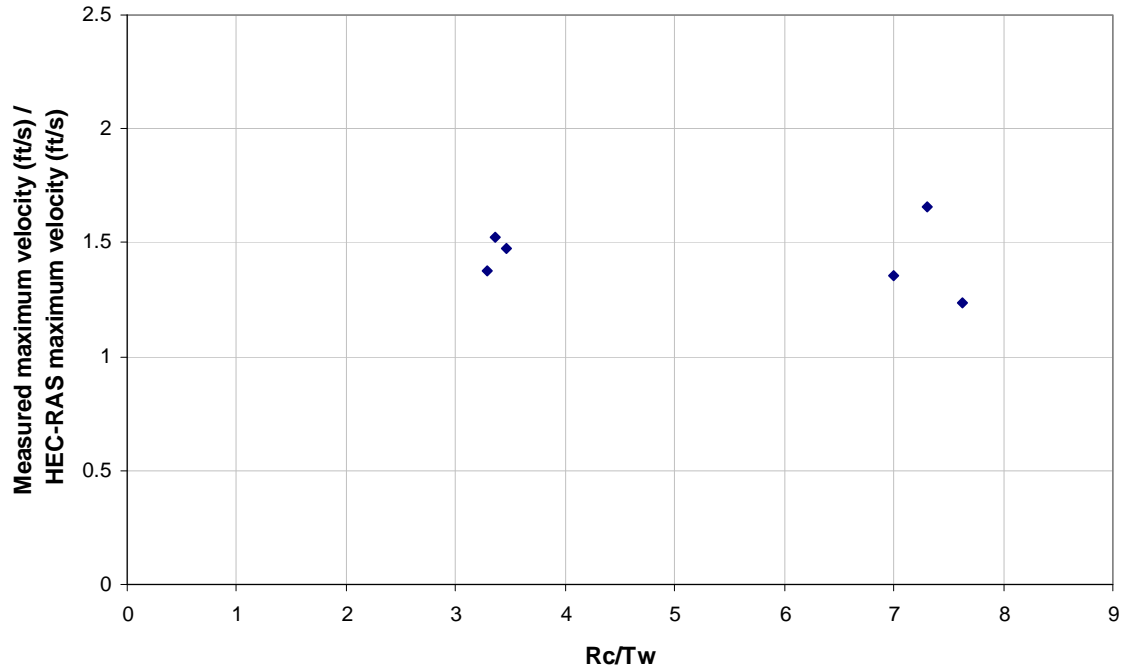
Figure 6.17: Relative Increases in Maximum Velocity from HEC-RAS Results

6.4 Limitations

Several limitations exist for K_b and V_b equations presented. Channel geometry and approach conditions may not be transposable to other systems and channel adjustments were not simulated as the bed of the model was immobile. Preston tube results may not account for the total shear stress acting in the transverse direction. Equations for K_b utilizing approach estimates from HEC-RAS assume Preston tube estimates are accurate. Velocity equations and relationships presented are dependent on channel geometry and may not be transposable to other systems. Data were obtained using an ADV with a sampling rate of 25 Hz which is suitable for quantifying mean velocities. Multipliers associated with HEC-RAS results are dependent on the detail of bend geometry implemented in the program. Use of the K_b and or V_b equations presented assumes the aforementioned limitations are satisfactory.

7 CONCLUSIONS AND RECOMMENDATIONS

7.1 Overview

The research presented has explored local shear stress approximations by methods available in two bends with highly 3-D flow fields. Strengths and weaknesses of each method were explored. Distributions of the results have been displayed with comparisons between discharges, methods, and known characteristics of flow in bends and inferences were made. Practical applications were explored with the relative shear stress and velocity approximations, and limitations of equations developed were noted.

7.2 Conclusions

- Preston tube, law of the wall, and Reynolds methods exhibited consistent distributions with current design guidelines and findings by others with high shear on the inner bank at the bend entrance and on the outer bank downstream of the bend apex.

- Application of the law of the wall in bends is questionable due to the presence of the highly 3-D flow field. Additionally, determination of applicable data used for regression may result in significant differences in the estimation of shear stress.

- Turbulent kinetic energy shear stress estimates were low throughout the bend and distributions were inconsistent with results from other methods. Reevaluation of the proportionality constant and applicable relative depth in fluvial environments should be conducted.

- Reynolds bed shear stress approximations using a near-bed point were lower than HEC-RAS results in the bends, which was contrary to an expected increase due to inclusion of transverse shear. Additionally, a standard relative depth may not be applicable as the roughness sublayer varies.

- Extrapolation of Reynolds shear stresses to the bed resulted in shear stress estimates greater than Reynolds near-bed approximations but results were primarily limited to locations where secondary currents were prevalent.

- Preston tube results were greater than any other method but provided the only viable option for determining relative shear stress with respect to 1-D approach approximations.

- Relative shear stress (K_b) magnitudes were higher than findings by others, which were attributed to native topographic features that were not modeled in previous investigations.

- Relationships were determined for the increase in boundary shear stress found in bends with native topographic features utilizing Preston tube estimates. Equations are presented in Table 7.1.

Table 7.1: K_b Equations for Native Topographic Features

Mean Regression	Upper Envelope
$K_b = 26.1\left(\dfrac{R_c}{T_w}\right)^{-0.88}$	$K_b = 43.2\left(\dfrac{R_c}{T_w}\right)^{-1.06}$

where K_b = shear stress multiplier $\left(\dfrac{\tau_{max}}{\tau_{app}}\right)$ [dimensionless], where τ_{max} = maximum shear stress in the bend [ML^{-1}T^{-2}] and τ_{app} = approach shear stress to the bend at a maximum flow depth [ML^{-1}T^{-2}];

R_c = radius of curvature [L]; and

T_w = top width of the channel [L].

- Relationships were determined for the increase in boundary shear stress found in bends with native topographic features utilizing HEC-RAS approach and Preston tube bend maximum estimates. Equations are presented in Table 7.2.

Table 7.2: K_b Equations for Native Topographic Features

Mean Regression	Upper Envelope
$K_b = 50.2\left(\dfrac{R_c}{T_w}\right)^{-0.82}$	$K_b = 70.06\left(\dfrac{R_c}{T_w}\right)^{-0.91}$

where K_b =   shear stress multiplier $\left(\dfrac{\tau_{max}}{\tau_{app}}\right)$ [dimensionless], where τ_{max} = maximum

shear stress in the bend [ML^{-1}T^{-2}] and τ_{app} = approach shear stress to the

bend at a maximum flow depth [ML^{-1}T^{-2}];

R_c =   radius of curvature [L]; and

T_w =   top width of the channel [L].

- Relationships for velocity increases in bends with native topographic features given approach velocity estimates from a 1-D numerical model were developed and are presented in Table 7.3.

**Table 7.3: Equations for Predicting Velocity Increase in Bends
with Native Topographic Features**

Mean Regression	Upper Envelope
$V_b = 5.15\left(\dfrac{R_c}{T_w}\right)^{-0.45}$	$V_b = 7.86\left(\dfrac{R_c}{T_w}\right)^{-0.62}$

where V_b =   velocity multiplier $\left(\dfrac{V_{max}}{V_{app}}\right)$ [dimensionless], where V_{max} = maximum

velocity in the bend [LT^{-1}] and V_{app} = average approach velocity to the

bend [LT^{-1}];

R_c =   radius of curvature [L]; and

T_w =   top width of the channel [L].

- Limitations to K_b and V_b equations are noted and should be taken into consideration before application in practice.
- A shear stress multiplier equation was developed for 1-D model results by comparison of bend maximums with Preston tube results. Equation 7.1 represents the upper envelope of results.

$$\frac{\tau_{max}}{\tau_{max\,HEC-RAS}} = 8.48 \left(\frac{R_c}{T_w} \right)^{-0.39}$$

Equation 7.1

where

τ_{max} = maximum shear stress in bend from Preston tube $[ML^{-1}T^{-2}]$;

$\tau_{max\,HEC-RAS}$ = maximum shear stress in bend from HEC-RAS $[ML^{-1}T^{-2}]$;

R_c = radius of curvature [L]; and

T_w = channel top width [L].

- A velocity multiplier of 1.5 to 1.7 was determined for 1-D numerical model results with detailed bend topographic features.

7.3 Recommendations for Future Research

The completed research suggests native topographic features have a large influence on shear stress in bends. Further investigation into quantifying maximum shear stress incorporating the effects of geometry should be conducted. Irregular geometry descriptors, such as shape terms, may be correlated with the marked increase in relative shear stress. If correlations do exist, the term or terms, should be incorporated with determining shear stress multipliers. Further investigation into the possibility of application of the turbulent kinetic energy approach in fluvial environments should be conducted by examination of the proportionality constant and applicable relative depth.

8 REFERENCES

Ackerman, J.D., Cottrell, C.M., Ethier, C.R., Allen, D.G., and Spelt, J.K. (1994). Preston-static tubes for the measurement of wall shear stress. *Journal of Fluids Engineering* 116:645-649.

Ackerman, J.D. and Hoover, T.M. (2001). Measurement of local bed shear stress in streams using a Preston-static Tube. *Limnology and Oceanography* 46(8):2080-2087.

Afzalimehr, H. and Anctil, F. (2000). Accelerating shear velocity in gravel-bed channels. *Hydrological Sciences* 45(1):113-124.

Afzalimehr, H., Heidarpour, M., and Salimi, A. (2006). Flow resistance in a compound gravel-bed bend. *Sadahana* 31(6):731-741.

Afzalimehr, H. and Rennie, C.D. (2009). Determination of bed shear stress in gravel-bed rivers using boundary-layer parameters. *Hydrological Sciences* 54(1):147-159.

Anwar, H.O. (1986). Turbulent structure in a river bend. *Journal of Hydraulic Engineering* 112(8):657-669.

Baird, D.C. (2004). Turbulent Flow and Suspended Sediment Transport in a Mobile, Sand Bed Channel with Riprap Side Slopes. Dissertation, University of New Mexico, Albuquerque, NM.

Bathurst, J.C. (1979). Distribution of boundary shear stress in rivers. In: Rhodes, D.D. and Williams, G.P. (Eds.), Adjustments of the Fluvial System, Kendall/Hunt Publishing Company.

Bergeron, N.E. and Abrahams, A.D. (1992). Estimating shear velocity and roughness length from velocity profiles. *Water Resources Research* 28(8):2155-2158.

Biron, P.M., Lane, S.N., Roy, A.G., Bradbrook, K.F., and Richards, K.F. (1998). Sensitivity of bed shear stress estimated from vertical velocity profiles: the problem of sampling resolution. *Earth Surface Processes and Landforms* 23:133-139.

Biron, P.M., Robson, C., Lapointe, M.F., and Gaskin, S.J. (2004). Comparing different methods of bed shear stress estimates in simple and complex flow fields. *Earth Surface Processes and Landforms* 29:1403-1415.

Blanckaert, K. and Graf, W.H. (2001). Mean flow and turbulence in open-channel bend. *Journal of Hydraulic Engineering* 127(10):835-846.

Blanckaert, K. and de Vriend, H.J. (2004). Secondary flows in sharp open-channel bends. *Journal of Fluid Mechanics* 498:353-380.

Brown, R.E. (1988). Boundary Shear Stress in Meandering Laboratory Channels with Rectangular and Naturally Varying Cross Sections. Thesis, University of Texas at Austin, Austin, TX.

Cardoso, A.H., Graf, W.H., and Gust, G. (1989). Uniform flow in a smooth channel. *Journal of Hydraulic Research* 27(5).

Chen, G. and Shen, H.S. (1984). River curvature-width ratio effect on shear stress. In: Elliott, C.M. (Ed.), Proceedings Conference on Rivers, New Orleans, LA, October 24-26, 1983, pp. 687-699.

Chow, V.T. (1959). Open Channel Hydraulics. McGraw Hill, 680 p.

Coles, D.E. (1956). The law of the wake in the turbulent boundary layer. *Journal of Fluid Mechanics* 1:191-226.

Darrow, J. (2004). Effects of Bendway Weir Characteristics on Resulting Flow Conditions. M.S. Thesis, Colorado State University, Department of Civil Engineering, Fort Collins, CO.

Davinroy, R.D., Rapp, R.J., and Myhre, R.E. (1998). Hydroacoustic study of fishes in bendway weir fields of the Middle Mississippi River. In: Proceedings of the 1998 Wetlands Engineering and River Restoration Conference, Denver, CO, March 22-27.

Derrick, D.L. (1998). Four years later, Harland Creek Bendway Weir/Willow Post Bank Stabilization Demonstration Project. In: Proceedings of the 1998 International Water Resources Engineering Conference, Part 1 (of 2), August 3-7, Memphis, TN.

Dey, S. and Barbhuiya, A.K. (2005). Flow field at a vertical wall abutment. Technical Notes, *Journal of Hydraulic Engineering* 131(12):1126-1135.

Dey, S. and Lambert, M.F. (2005). Reynolds stress and bed shear in nonuniform unsteady open-channel flow. *Journal of Hydraulic Engineering* 131(7):610-614.

Dietrich, W.E. (1987). Mechanics of flow and sediment transport in river bends. In: Richards, K.S. (Ed.), River Channels: Environment and Process, Blackwell, Oxford, pp. 179-227.

Duan, J.G. (2009). Mean flow and turbulence around a laboratory spur dike. *Journal of Hydraulic Engineering* 135(10):803-811, DOI: 10.1061/(ASCE)HY.1943-7900. 0000077.

Federal Highway Administration (2005). Design of Roadside Channels with Flexible Linings. *Hydraulic Engineering Circular No. 15* (*HEC-15*), *Publication No. FHWA-NHI-05-114,*

U. S. Department of Transportation, Federal Highway Administration, Third Edition, September.

Fernandez Luque, R.F. and van Beek, R. (1976). Erosion and transport of bed-load sediment. *Journal of Hydraulic Resources* 14:127-144.

Finnemore, E.J. and Franzini, J.B. (2002). <u>Fluid Mechanics with Engineering Applications</u>. Tenth Edition, McGraw Hill Book Company, New York, NY.

Gates, T.K. (2008). CE612 Open Channel Flow Class Notes. Colorado State University, Department of Civil and Environmental Engineering, Fort Collins, CO.

Ghosh, S.N. and Roy, N. (1970). Boundary shear distribution in open channel flow. *Proceedings of the American Society of Civil Engineers*, *Journal of Hydraulics Division* 96(HY4):967-993.

Gordon, N.D., Finlayson, B.L., McMahon, T.A., and Gippel, C.J. (2004). <u>Stream Hydrology: An Introduction for Ecologists</u>. John Wiley and Sons, Ltd.

Goring, G.D. and Nikora, V.I. (2002). Despiking acoustic Doppler velocimeter data. *Journal of Hydraulic Engineering* 128(1):117-126.

Graf, W.H. and Song, T. (1995). Bed shear stress in non-uniform and unsteady open-channel flow. *Journal of Hydraulic Research* 33(5):699-704.

Heathershaw, A.D. (1979). The turbulent structure of the bottom boundary layer in a tidal current. *Geophysical Journal of the Royal Astronomical Society* 58:395-430.

Heintz, M.L. (2002). Investigation of Bendway Weir Spacing. M.S. Thesis, Colorado State University, Department of Civil Engineering, Fort Collins, CO.

Henderson, F.M. (1966). <u>Open Channel Flow</u>. MacMillan, New York, NY, 522 p.

Hickin, E.J. and Nanson, G.C. (1984). Lateral migration rates of river bends. *Journal of Hydraulic Engineering* 110:1557-1567.

Hinze, J.O. (1959). <u>Turbulence: An Introduction to its Mechanism and Theory</u>. McGraw Hill Book Company, Inc., The Maple Press Company, York, PA.

Hooke, LeB., R. (1975). Distribution of sediment transport and shear stress in a meander bend. *Journal of Geology* 83(5):543:565.

Hsu, E.Y. (1955). The Measurement of Local Turbulent Skin Friction by Means of Surface Pitot Tubes. Report No. 957, David W. Taylor Model Basin, August.

Huthnance, J.M., Humphery, J.D., Knight, P.J., Chatwin, G., Thomsen, L., and White, M. (2002). Near-bed turbulence measurements, stress estimates and sediment mobility at the continental shelf edge. *Progress in Oceanography* 52(2002):171-194.

Hwang, L.-S. and Laursen, E.M. (1963). Shear measurement technique for rough surfaces. *Proceedings of the American Society of Civil Engineers*, *Journal of Hydraulics Division* 89(HY2):19-37.

Ippen, A.T., Drinker, P.A., Jobin, W.R., and Noutsopoulos, G.K. (1960). The Distribution of Boundary Shear Stresses in Curved Trapezoidal Channels. Technical Report No. 43, Department of Civil and Sanitary Engineering, Massachusetts Institute of Technology, October.

Ippen, A.T. and Drinker, P.A. (1962). Boundary shear stresses in curved trapezoidal channels. *American Society of Civil Engineers*, *Journal of the Hydraulics Division* HY5:143-179.

Ippen, A.T., Drinker, P.A., Jobin, W.R., and Shemdin, O.H. (1962). Stream Dynamics and Boundary Shear Distributions for Curved Trapezoidal Channels. Technical Report No. 47, Department of Civil and Sanitary Engineering, Massachusetts Institute of Technology, January.

Julien, P.Y. (1998). Erosion and Sedimentation. Cambridge University Press, New York, NY.

Kendall, A. and Koochesfahani, M. (2008). A method for estimating wall friction in turbulent wall-bounded flows. *Experiments in Fluids* 44:773-780.

Kim, S.-C., Friedrichs, C.T., Maa, P.-Y., and Wright, L.D. (2000). Estimating bottom stress in tidal boundary layer from acoustic Doppler velocimeter data. *Journal of Hydraulic Engineering* 126(6):399-406.

Kinzli, K. (2005). Effects of Bendway Weir Characteristics on Resulting Eddy and Channel Flow Conditions. M.S. Thesis, Colorado State University, Department of Civil Engineering, Fort Collins, CO.

Knight, D.W. and Shiono, K. (1990). Turbulence measurements in a shear layer region of a compound channel. *Journal of Hydraulic Research* 28(2):175-196.

Knighton, D. (1998). Fluvial Forms and Processes: A New Perspective. Oxford University Press Inc., New York, NY, 383 p.

Lane, E.W. (1955) Design of stable channels. *Transactions of the American Society of Civil Engineers* 120(1955):1234-1260.

Ludweig, H. and Tillman, W. (1950). Investigations of the Wall-shearing Stress in Turbulent Boundary Layers. Technical Memorandum 1285, National Advisory Committee for Aeronautics, May.

Markham, A.J. and Thorne, C.R. (1992). Geomorphology of gravel-bed river bends. In: Billi P., Hey, R.D., Thorne, C.R., and Tacconi, P. (Eds.), Dynamics of Gravel-Bed Rivers, John Wiley, Chichester, UK, pp. 433-456.

McLelland, S.J. and Nicholas, A.P. (2000). A new method for evaluating errors in high-frequency ADV measurements. *Hydrological Processes* 14:351-366.

Montes, S. (1998). Hydraulics of Open Channel Flow. American Society of Civil Engineers, Reston, VA.

Nezu, I. and Nakagawa, H. (1993). Turbulence in Open Channel Flow. International Association of Hydro-Environment Engineering and Research (IAHR) Monograph, A.A. Balkema, Rotterdam.

Nikora, V. and Goring, D. (2000). Flow turbulence over fixed and weakly mobile gravel beds. *Journal of Hydraulic Engineering* 126(9):679-690.

Nouh, M.A. and Townsend, R.D. (1979). Shear stress distribution in stable channel bends. *Proceedings of the American Society of Civil Engineers*, *Journal of Hydraulics Division* 105(HY10):1233-1245.

Preston, J.H. (1954). The determination of turbulent skin friction by means of Pitot tubes. *Journal of the Royal Aeronautical Society* 58:109-121.

Richard, G.A. (2001). Quantification and Prediction of Lateral Channel Adjustments Downstream from Cochiti Dam, Rio Grande, NM. Ph.D. Dissertation, Colorado State University, Department of Civil Engineering, Fort Collins, CO.

Richards, K. (1982). Rivers: Form and Process in Alluvial Channels. Routledge, 272 p.

Roy, A.G., Biron, P., and de Serres, B. (1996). On the necessity of applying rotation to instantaneous velocity measurements in river flows. *Earth Surface Processes and Landforms* (21):817-827.

Schlichting, H. (1968). Boundary Layer Theory. McGraw Hill Book Company, New York, NY.

Sclafani, P. (2008). Preston Tube Calibration. Open File Report, Colorado State University, Engineering Research Center, Fort Collins, CO, July.

Shields Jr., F.D., Knight, S.S., and Cooper, C.M. (1998). Addition of spurs to stone toe protection for warmwater fish habitat rehabilitation. *Journal of the American Water Resources Association* 34(6):1427-1436.

Shields, Jr., F.D., Simon, A., and Dabney, S.M. (2009). Streambank dewatering for increased stability. *Hydrological Processes* 23:1537-1547.

Shiono, K. and Muto, Y. (1998). Complex flow mechanisms in compound meandering channels with overbank flow. *Journal of Fluid Mechanics* 376:221-261.

Simon, A., Curini, A., Darby, S.E., and Langendeon, E.J. (2000). Bank and near-bank processes in an incised channel. *Geomorphology* 35:193-217.

Sin, K.-S. (2010). Methodology for Calculating Shear Stress in a Meandering Channel. M.S. Thesis, Colorado State University, Department of Civil and Environmental Engineering, Fort Collins, CO.

Song, T. (1994). Velocity and Turbulence Distribution in Open-channel Flow. PhD Dissertation, No. 1324, Ecole Polytechnique Federale, Lausanne, Switzerland.

Song, T. and Graf, W.H. (1994). Non-uniform open-channel flow over a rough bed. *Journal of Hydroscience and Hydraulic Engineering* 12(1):1-25.

Sontek (2001). Acoustic Doppler Velocimeter (Field) Technical Documentation. Sontek/YSI, Inc., San Diego, CA.

Soulsby, R.L. (1983). The bottom boundary layer of shelf seas. In: Johns, B. (Ed.), <u>Physical Oceanography of Coastal and Shelf Seas</u>, Elsevier Oceanography Series, 35, pp. 189-262.

Thompson, A. (1986). Secondary flows and the pool-riffle unit: a case study of the processes of meander development. *Earth Processes and Landforms* 11, 631-641.

Thomson, J. (1876). On the origin of windings of rivers in alluvial plains, with remarks on the flow of water round bends in pipes. *Proceedings of the Royal Society of London* 25:5-8.

Thorne, C.R. (1991). Bank erosion and meander migration of the Red and Mississippi Rivers, USA. In: <u>Hydrology for the Water Management of Large River Basins</u> (Proceedings of the Vienna Symposium, August), International Association of Hydrological Sciences (IAHS) Publication No. 201.

Tilston, M. (2005). Three-dimensional Flow Structure, Turbulence and Bank Erosion in a 180$^\mathrm{o}$ Meander Loop. Thesis, University of Montreal, Quebec, Canada.

U. S. Army Corps of Engineers (1970). Hydraulic Design Criteria: Sheet 703-1 Riprap Protection, Trapezoidal Channel, 60 Deg-bend, Boundary Shear Distribution. U.S. Army Engineer Waterways Experiment Station, Vicksburg, MS.

U. S. Army Corps of Engineers (2008). HEC-RAS River Analysis System, Hydraulic Reference Manual – Version 3.1. U.S. Army Corps of Engineers, Hydrologic Engineering Center, Davis, CA.

U. S. Bureau of Reclamation (1964). Progress Report I Boundary Shear Distribution around a Curve in a Laboratory Canal. Report No. Hyd-526, June.

U. S. Bureau of Reclamation (2000). Meander Bend Surveys, Geomorphic Data Analysis & Field Data Collection Report July 1999 through January 2000. Report submitted to the U.S. Department of the Interior, Bureau of Reclamation, Albuquerque, NM.

Wahl, T.L. (2002). Discussion of "Despiking acoustic Doppler velocimeter data" by Goring, D.G. and Nikora, V.I. *Journal of Hydraulic Engineering* 128(1):117-126.

Walker, K.W. (2008). Comparison of a Generalized Trapezoidal Hydraulic Model to a Native Topography Patterned Bed Surface Model of the Rio Grande. Plan B Report, Colorado State University, Department of Civil and Environmental Engineering, Fort Collins, CO.

Wang, Z.Q. and Cheng, N.S. (2005). Secondary flows over artificial bed strips. *Advances in Water Resources* 28(5):441-450.

Wilcox, D.C. (2007). Basic Fluid Mechanics. Third Edition, DCW Industries.

Yen, B.C. (1965). Characteristics of Subcritical Flow in a Meandering Channel. Ph.D Dissertation, University of Iowa, Department of Mechanics and Hydraulics, Iowa City, IA, June.

Young, G.K., Kenneth, G., Pearson, D.R., Stein, S.M., Krolak, J.S., and Atayee, A.T. (1996). HYDRAIN − Integrated Drainage Design Computer System: Version 6.0. FHWA-SA-96-064, Volume VI, HYCL, Washington, DC.

APPENDIX A

MODEL CROSS SECTIONS

(Cross sections were created from Light Detection and Ranging (LiDAR) data with the use of ArcGIS. Water-surface elevations were averaged across the seven data locations for each given cross section. Distances illustrated are increasing from river right to left.)
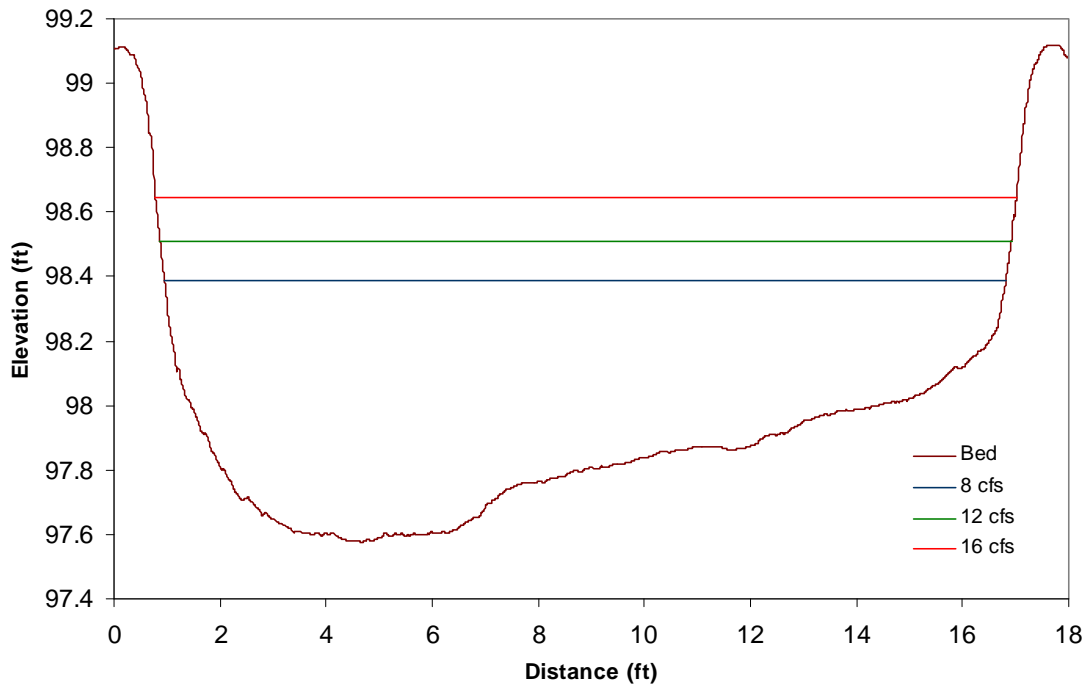
Figure A.1: Cross Section 1
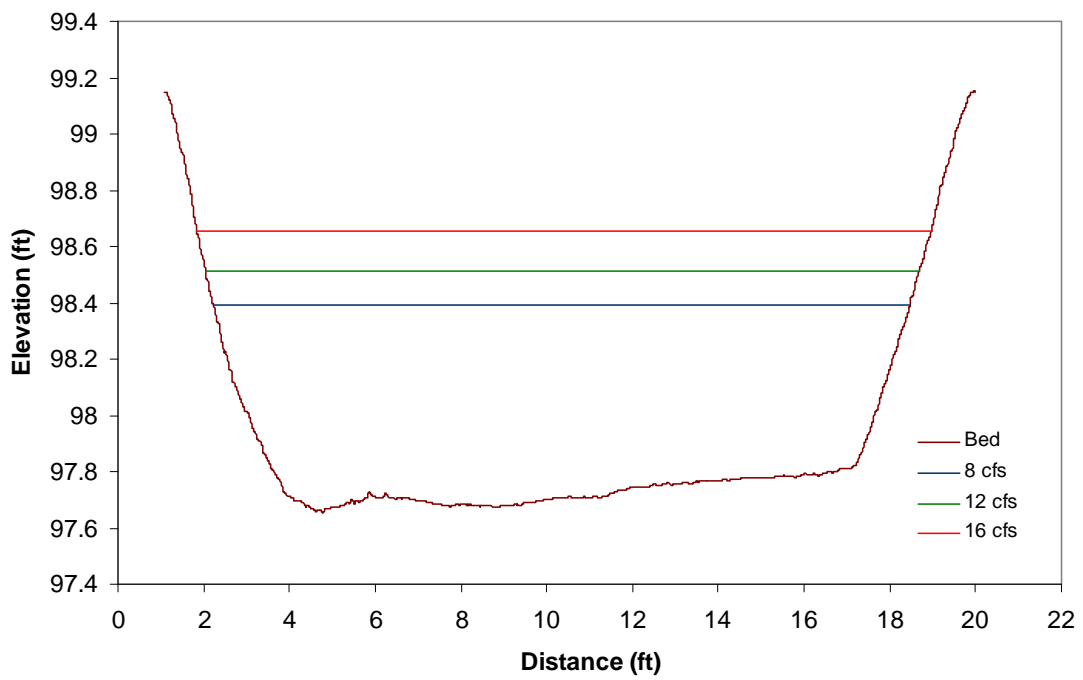
Figure A.2: Cross Section 2
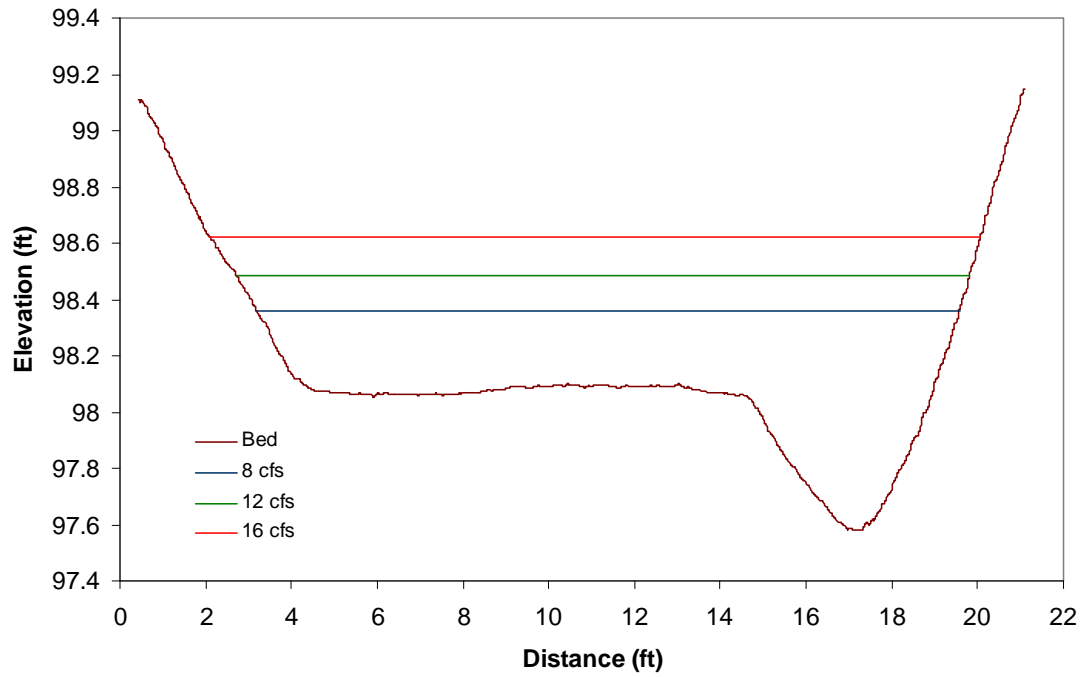
Figure A.3: Cross Section 3
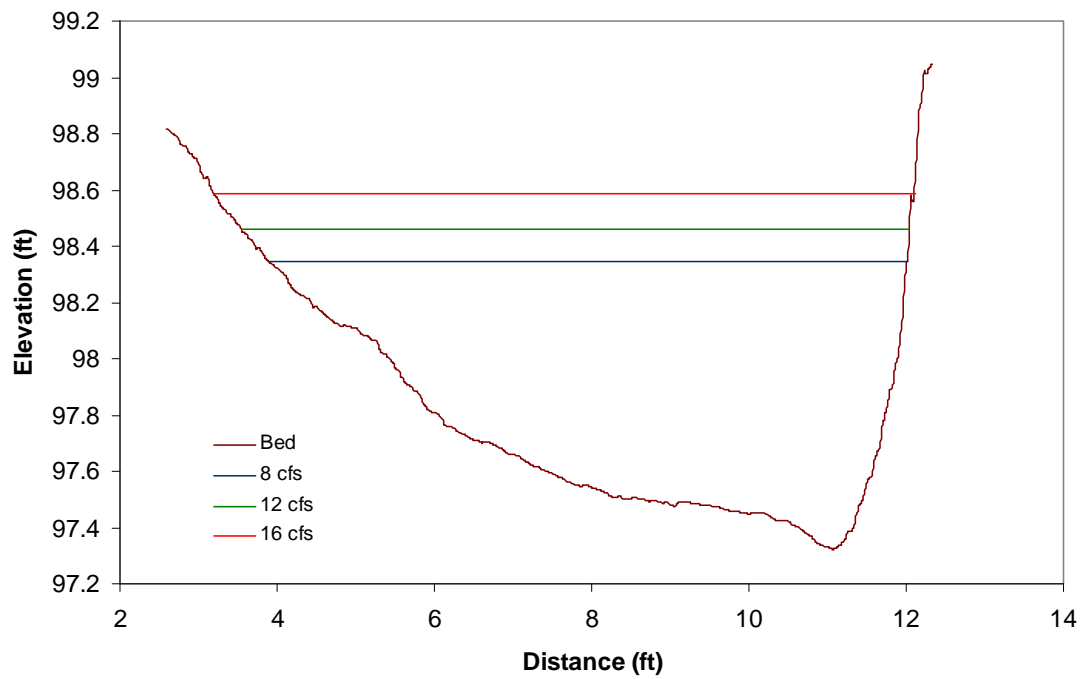
Figure A.4: Cross Section 4
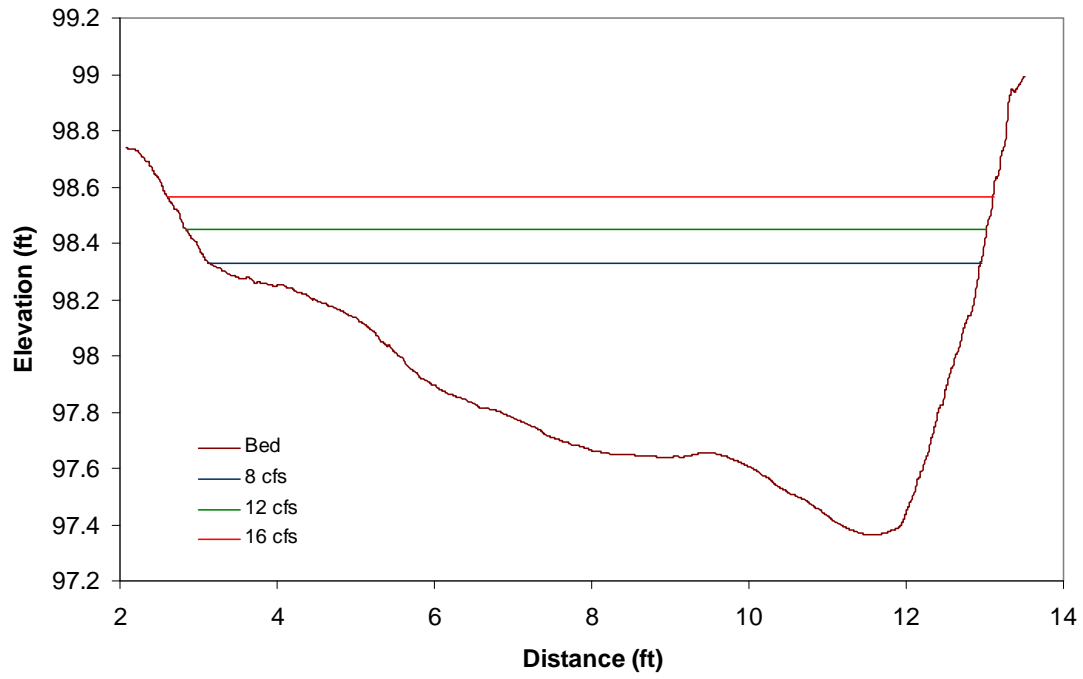
Figure A.5: Cross Section 5
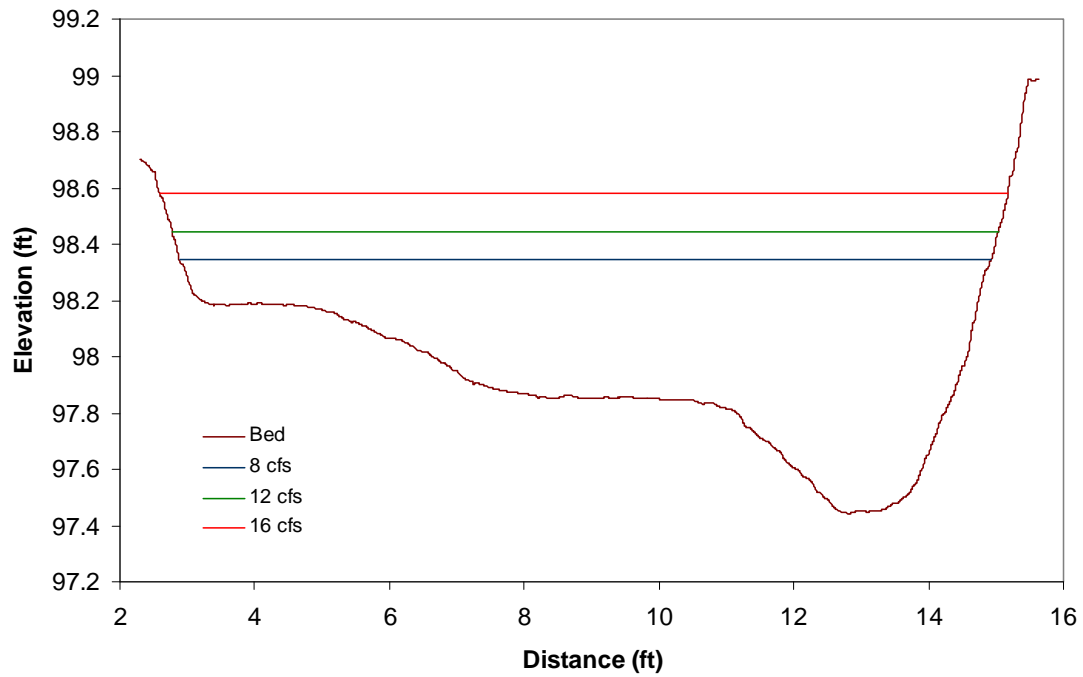
Figure A.6: Cross Section 6
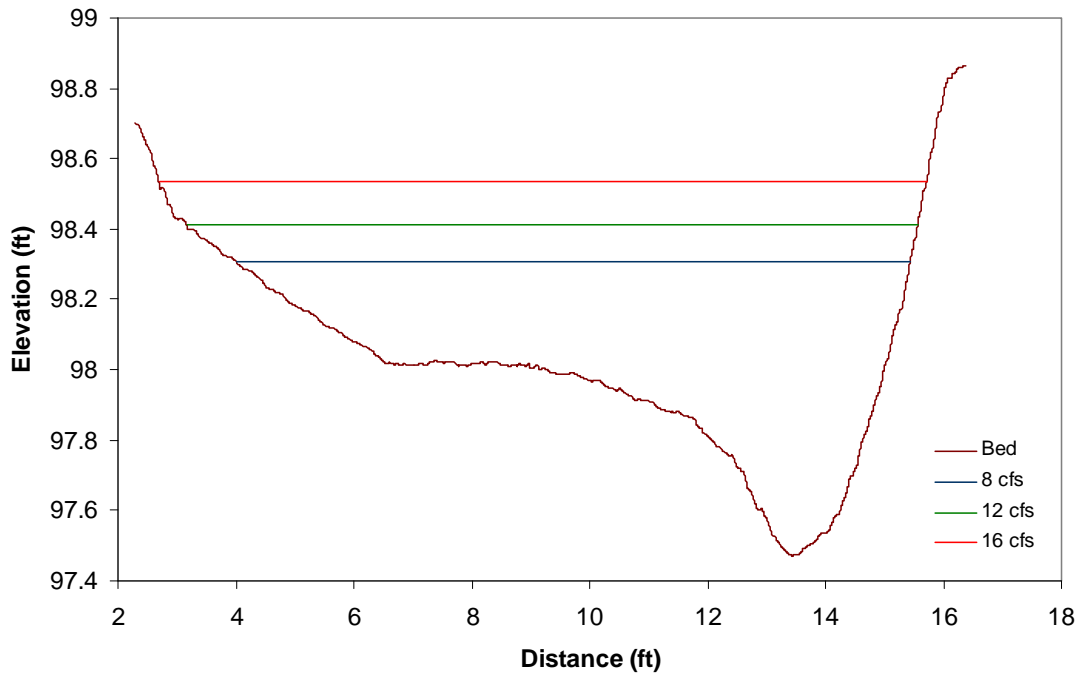
Figure A.7: Cross Section 7
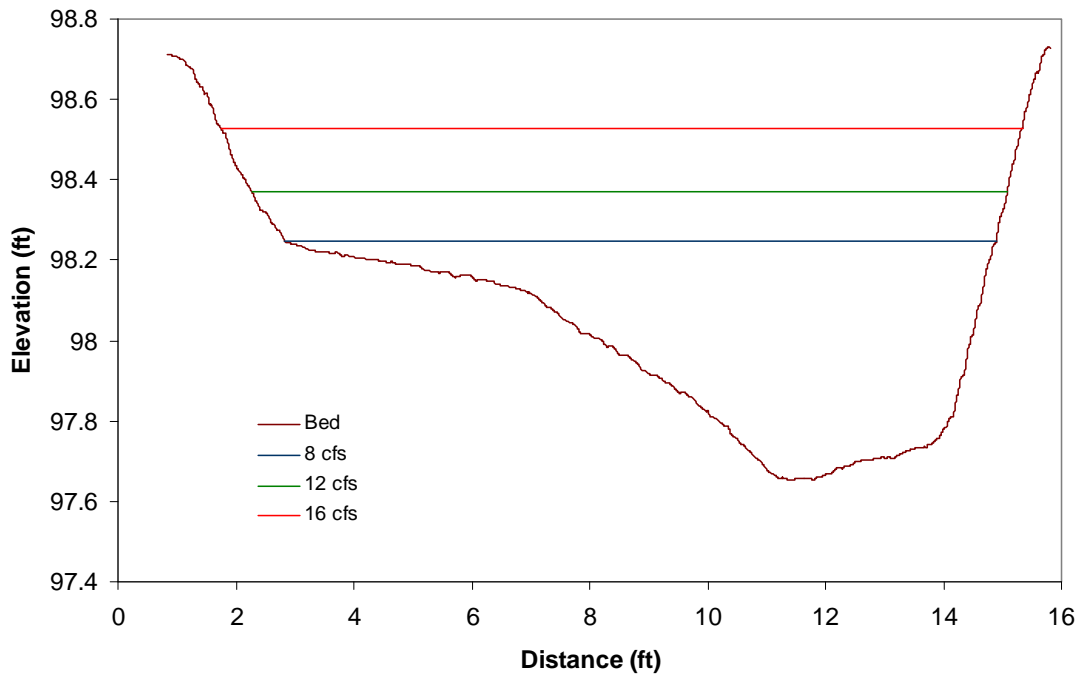
Figure A.8: Cross Section 8
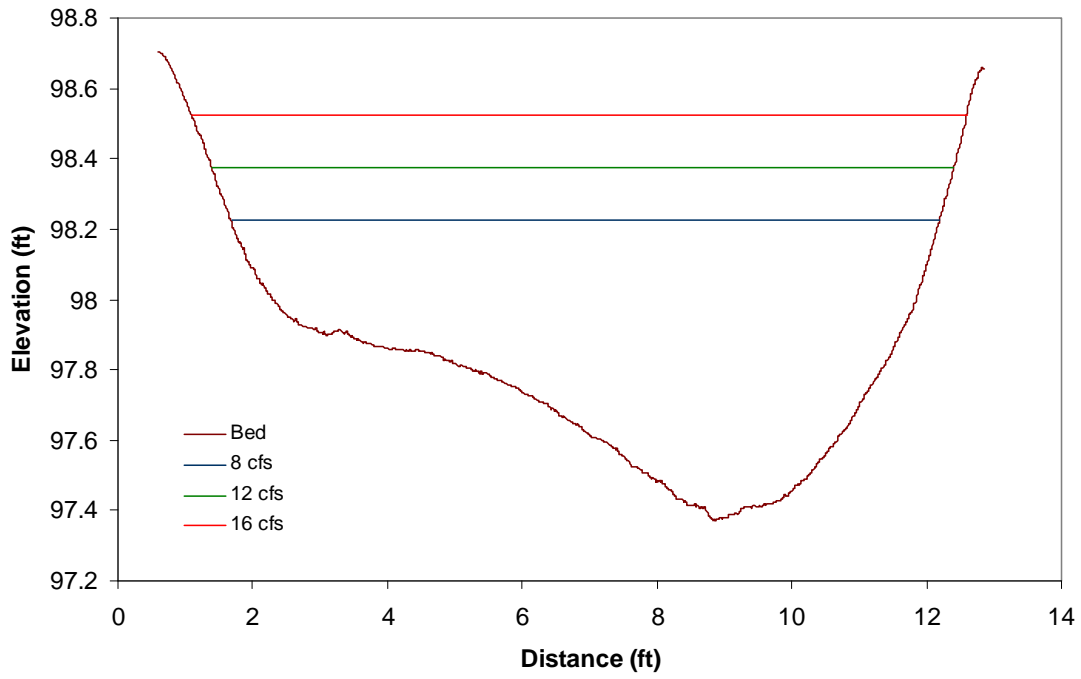
Figure A.9: Cross Section 9
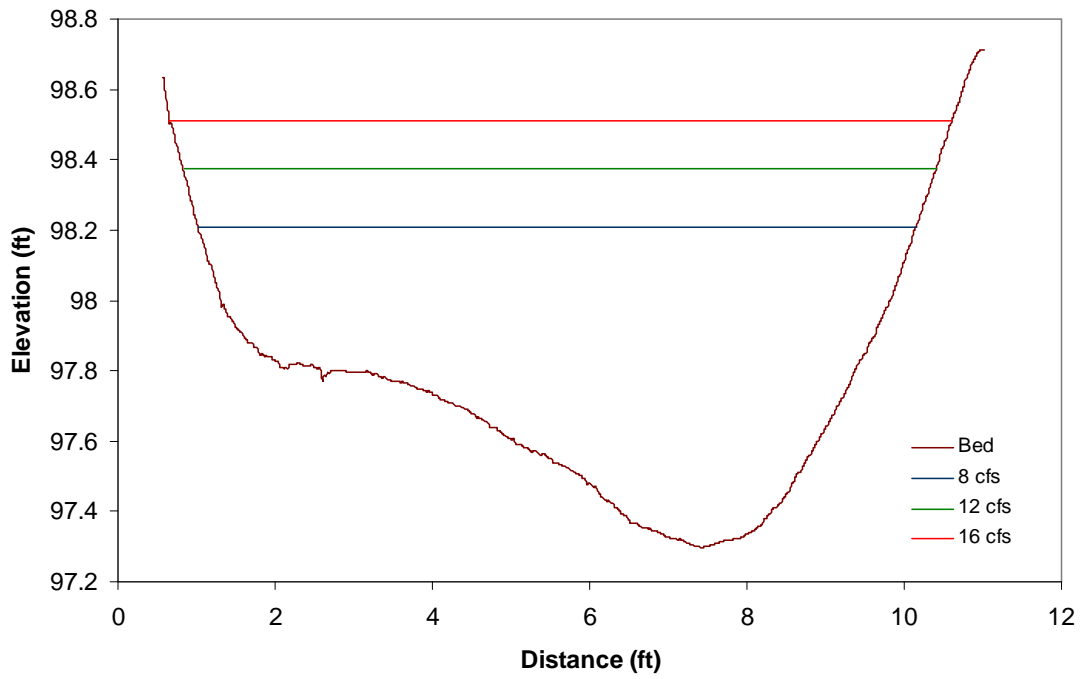
Figure A.10: Cross Section 10
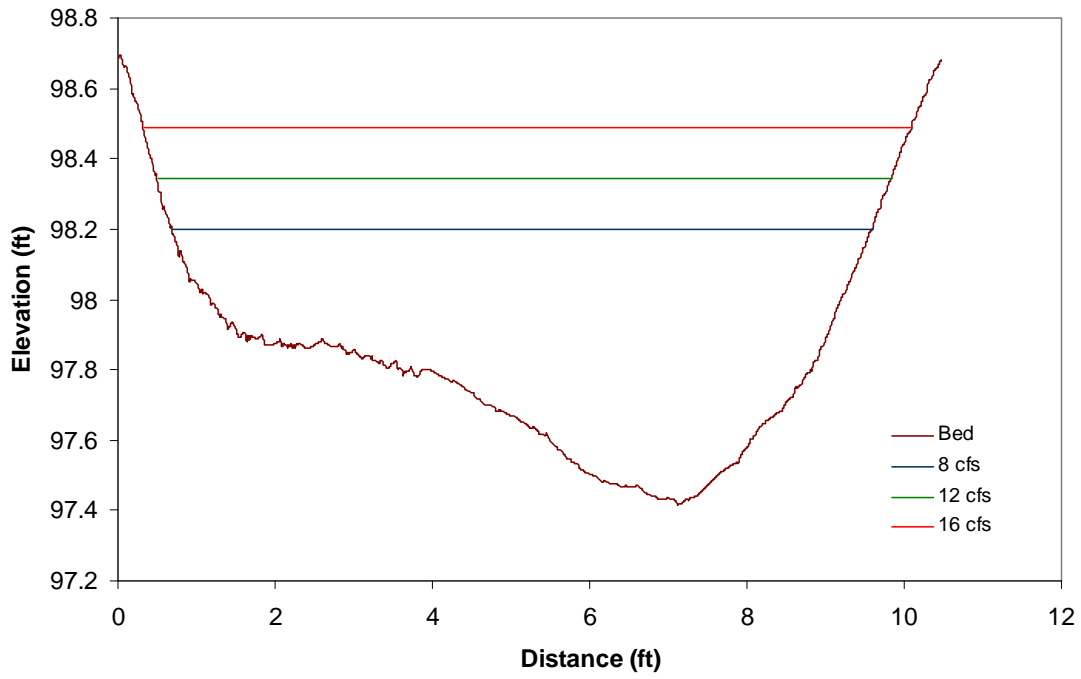
Figure A.11: Cross Section 11
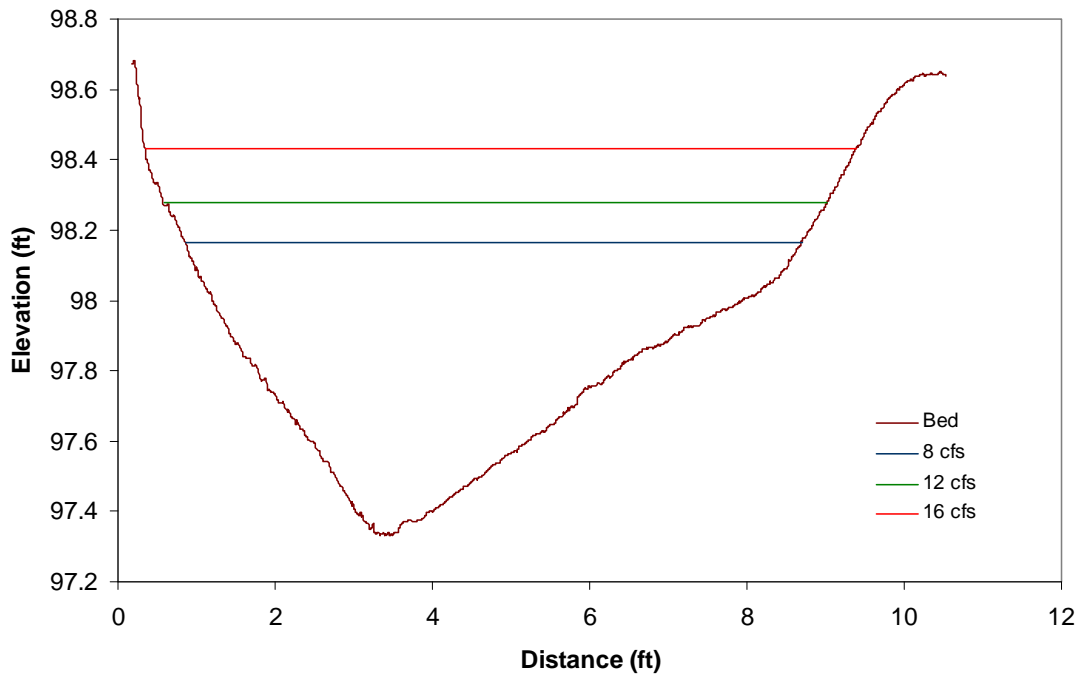
Figure A.12: Cross Section 12
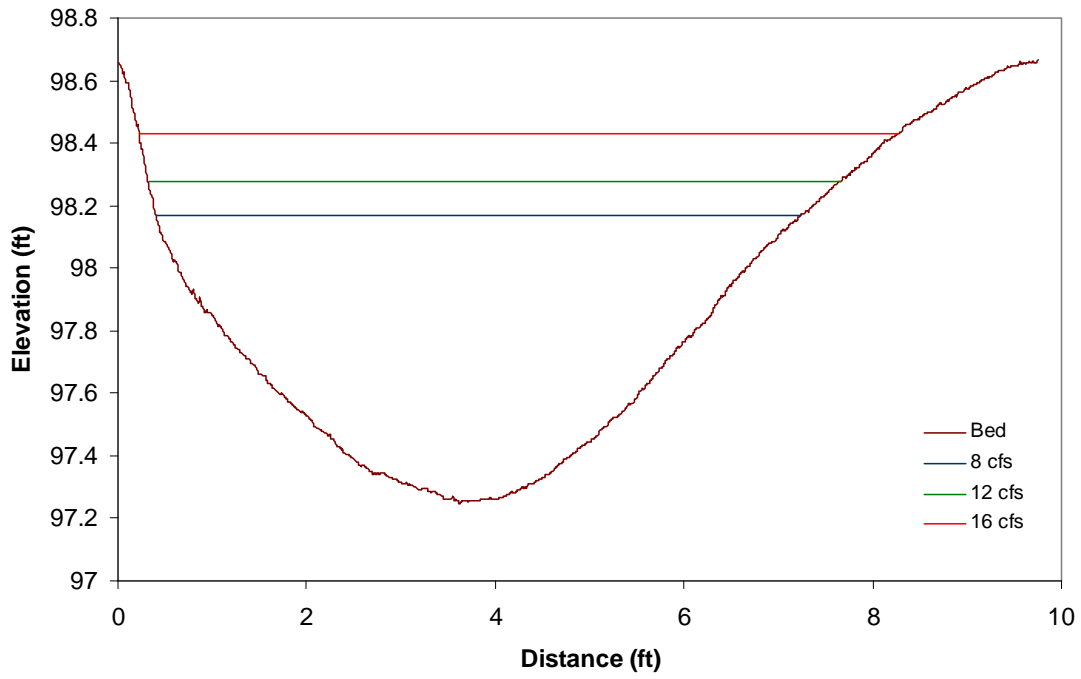
Figure A.13: Cross Section 13
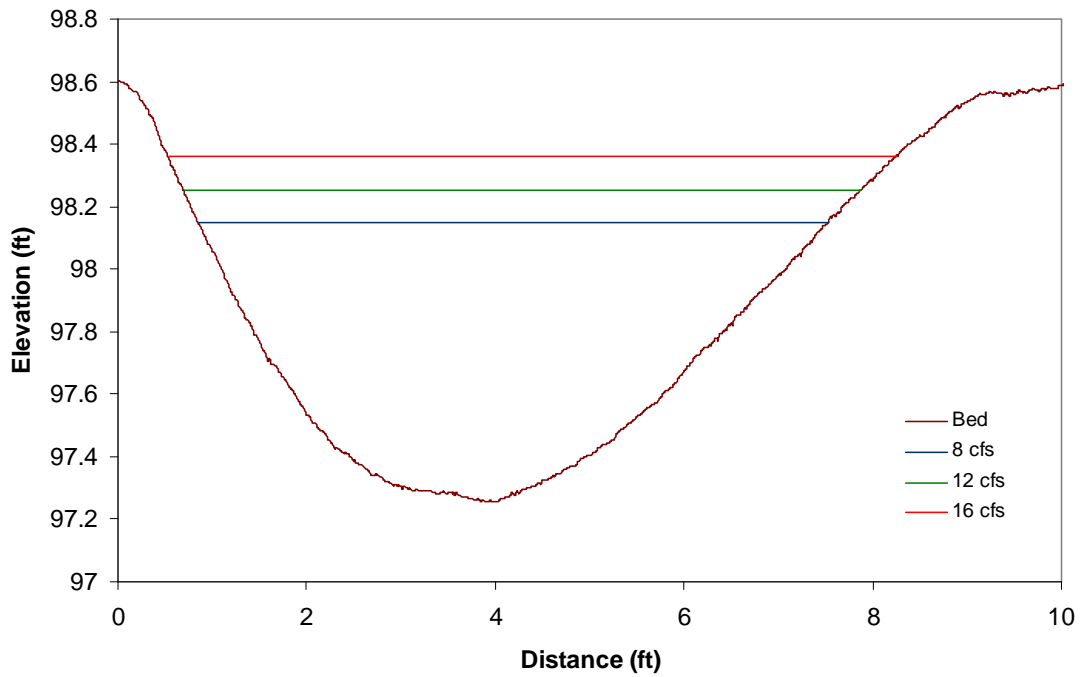
Figure A.14: Cross Section 14
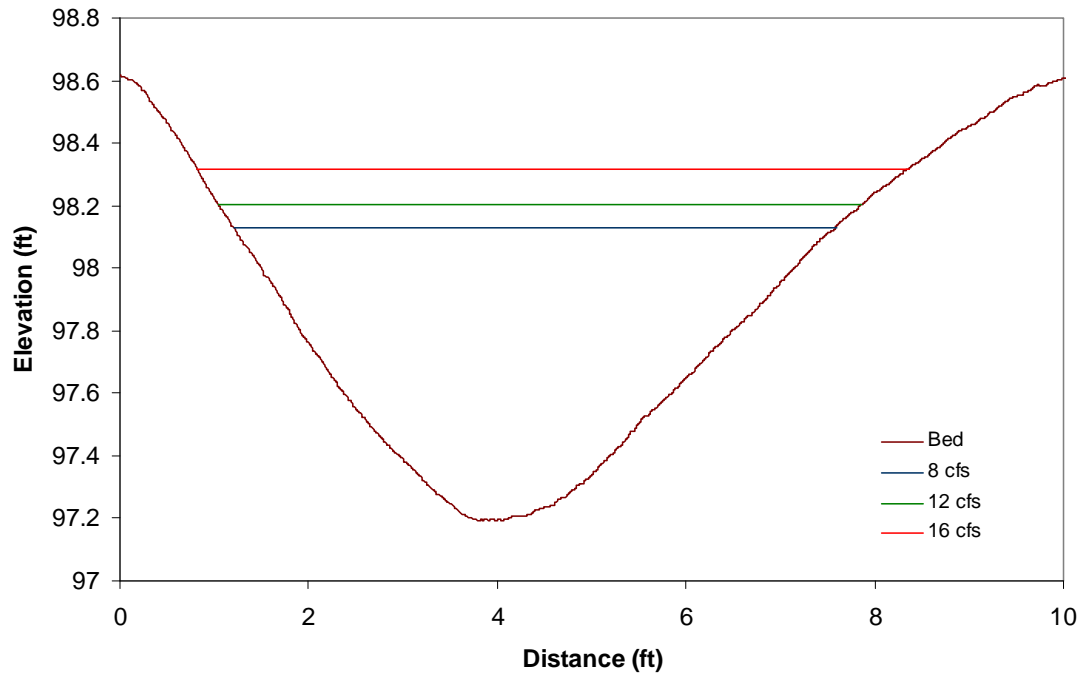
Figure A.15: Cross Section 15
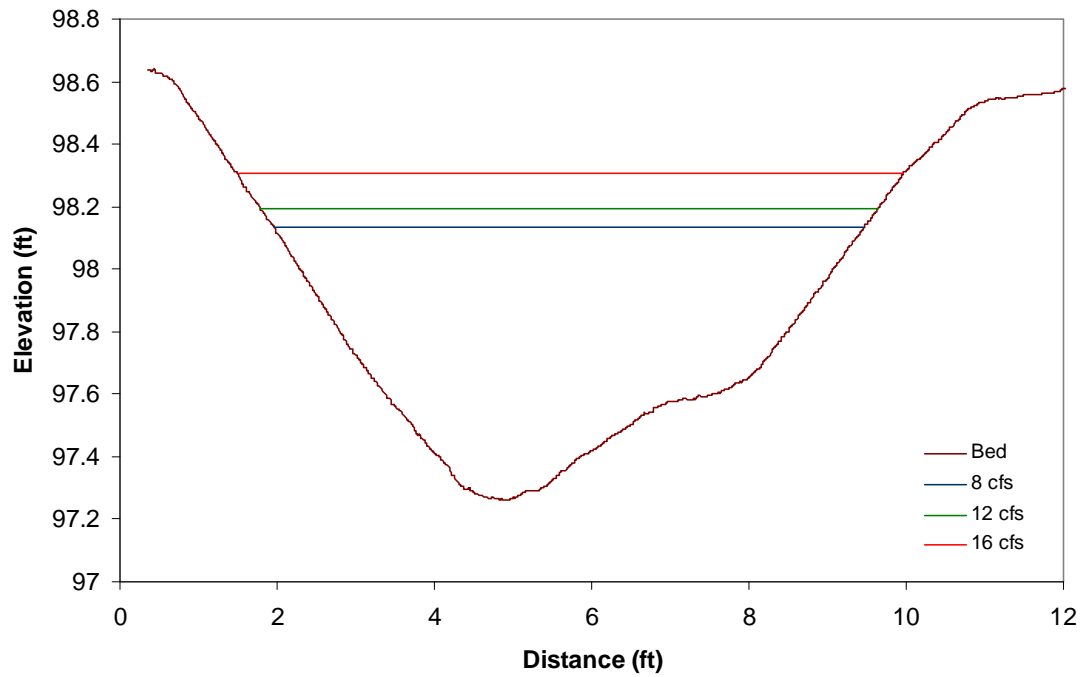
Figure A.16: Cross Section 16
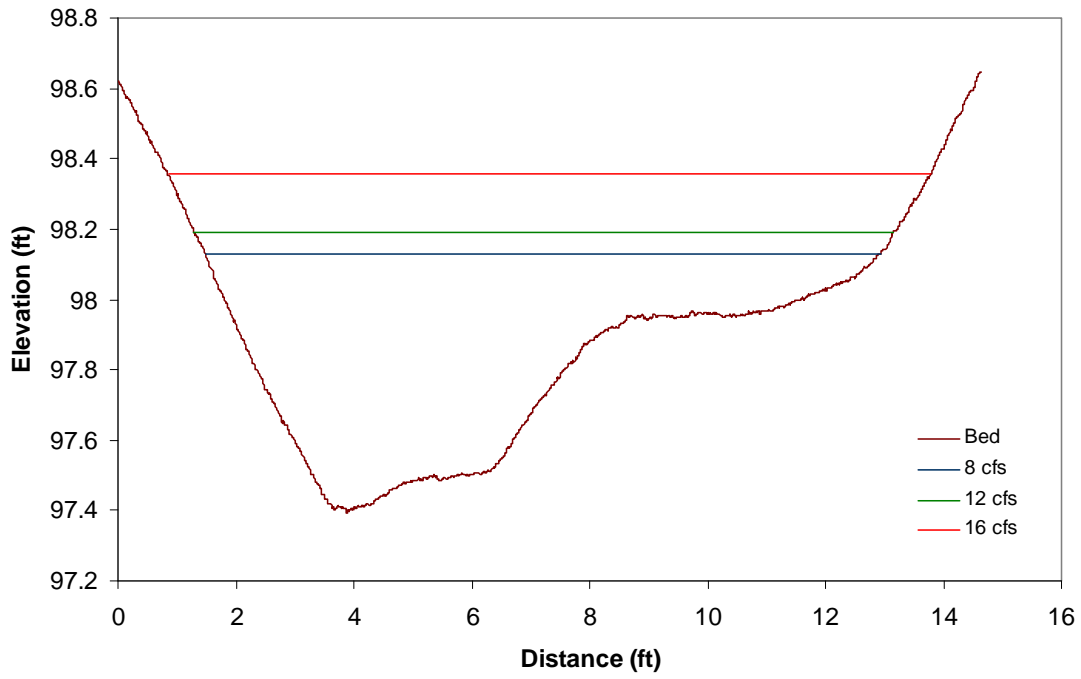
Figure A.17: Cross Section 17
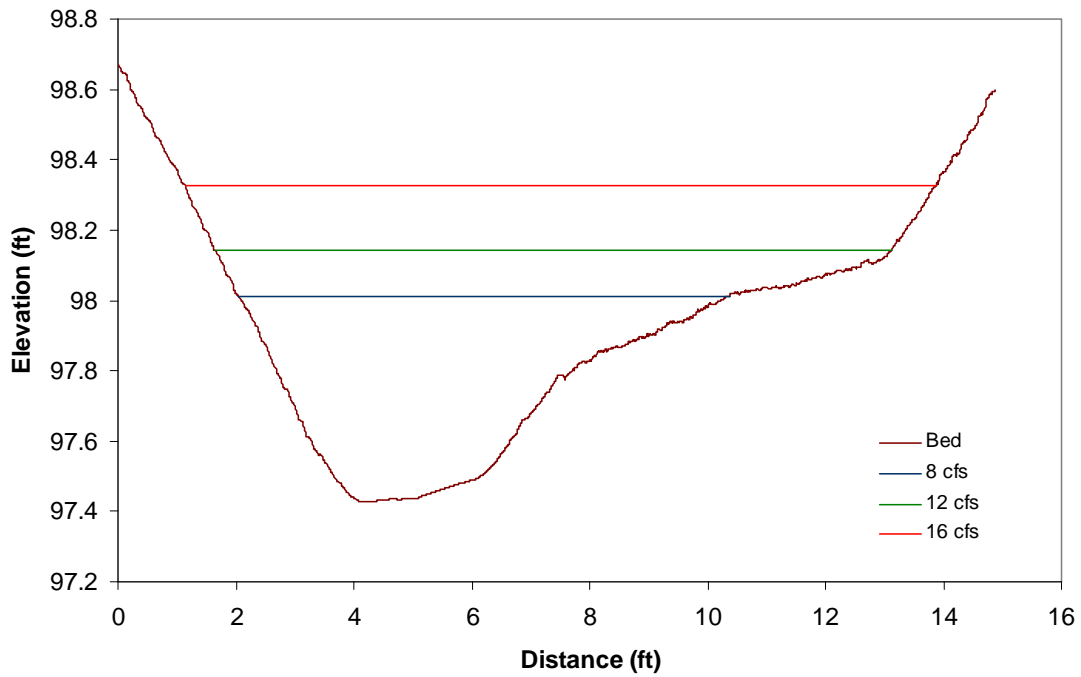
Figure A.18: Cross Section 18

APPENDIX B

CALCULATED SHEAR STRESS BY METHOD

(Values calculated for each location are given by method. The relative depths for near-bed points used in the Reynolds and TKE methods.)

Table B.1: Calculated Shear Stresses by Method

Q (cfs)	Cross-section Number	Location	Relative Depth (y/h) for TKE and Reynolds Methods	Method Law of the Wall (psf)	Preston Tube (psf)	Reynolds – Near-bed Point (psf)	Reynolds – Extrapolated (psf)	TKE (psf)
8	1	a	0.1	-	-	0.0083	-	0.0065
8	1	b	0.1	-	0.0040	0.0003	-	0.0056
8	1	c	0.1	0.0174	0.0293	0.0060	-	0.0035
8	1	d	0.1	0.0103	0.0347	0.0047	0.0054	0.0035
8	1	e	0.1	0.0175	0.0278	0.0055	0.0076	0.0019
8	1	f	0.1	0.0194	0.0224	0.0037	-	0.0040
8	1	g	0.1	0.0135	0.0251	0.0049	-	0.0020
8	2	a	0.1	-	0.0020	0.0036	-	0.0032
8	2	b	0.1	-	0.0099	0.0047	-	0.0005
8	2	c	0.1	0.0119	0.0132	0.0039	-	0.0004
8	2	d	0.1	0.0105	0.0186	0.0048	0.0115	0.0020
8	2	e	0.1	0.0082	0.0121	0.0037	-	0.0016
8	2	f	0.1	0.0221	0.0175	0.0051	0.0067	0.0027
8	2	g	0.1	-	0.0074	0.0030	-	0.0005
8	3	a	0.1	0.0196	0.0107	0.0076	-	0.0004
8	3	b	0.1	0.0219	0.0251	0.0106	-	0.0019
8	3	c	0.1	0.0237	0.0627	0.0062	-	0.0019
8	3	d	0.1	0.0051	0.1368	0.0039	-	0.0200
8	3	e	0.1	0.0395	0.1565	0.0076	-	0.0203
8	3	f	0.1	0.0167	0.0226	0.0015	-	0.0017
8	3	g	0.1	-	0.0054	0.0006	-	0.0004
8	4	a	0.1	0.0030	0.0965	0.0086	0.0103	0.0066
8	4	b	0.1	0.0364	0.0649	0.0073	0.0145	0.0072
8	4	c	0.1	0.0772	0.0815	0.0074	0.0126	0.0104
8	4	d	0.1	0.0199	0.0370	0.0077	-	0.0017
8	4	e	0.1	0.0112	0.0322	0.0103	-	0.0013
8	4	f	0.1	0.0094	0.0439	0.0106	-	0.0014
8	5	a	0.1	0.0338	0.0361	0.0156	0.0199	0.0006

Q (cfs)	Cross-section Number	Location	Relative Depth (*y/h*) for TKE and Reynolds Methods	Method				
				Law of the Wall (psf)	Preston Tube (psf)	Reynolds – Near-bed Point (psf)	Reynolds – Extrapolated (psf)	TKE (psf)
8	5	b	0.1	0.0367	0.0549	0.0099	0.0148	0.0117
8	5	c	0.1	0.0243	0.0768	0.0093	0.0107	0.0122
8	5	d	0.1	0.0333	0.0387	0.0107	0.0175	0.0038
8	5	e	0.1	0.0273	0.0352	0.0128	0.0147	0.0018
8	5	f	0.1	-	0.0358	0.0042	-	0.0003
8	6	a	0.1	0.0331	0.0446	0.0178	0.0265	0.0043
8	6	b	0.1	0.0304	0.0616	0.0094	0.0124	0.0075
8	6	c	0.1	0.0613	0.0468	0.0084	-	0.0054
8	6	d	0.1	0.0091	0.0688	0.0077	-	0.0058
8	6	e	0.1	0.0138	0.0587	0.0075	-	0.0015
8	6	f	0.1	-	0.0490	0.0037	-	0.0457
8	7	a	0.1	0.1107	0.0605	0.0206	0.0352	0.0017
8	7	b	0.1	0.0534	0.0999	0.0141	0.0180	0.0080
8	7	c	0.1	0.0660	0.0558	0.0052	-	0.0006
8	7	d	0.1	0.0411	0.0979	0.0155	-	0.0011
8	7	e	0.125	0.0330	0.1086	0.0128	0.0165	0.0103
8	8	a	0.125	0.0568	0.0513	0.0436	-	0.0122
8	8	b	0.125	0.0752	0.1810	0.0194	0.0277	0.0127
8	8	c	0.1	0.0945	0.1265	0.0187	0.0422	0.0016
8	8	d	0.1	0.0408	0.1677	0.0204	-	0.0075
8	9	a	0.1	0.0122	0.0679	0.0462	-	0.0459
8	9	b	0.1	0.1681	0.0788	0.0576	0.0770	0.0172
8	9	c	0.1	0.1669	0.0981	0.0427	0.0636	0.0065
8	9	d	0.1	0.0082	0.0349	0.0109	-	0.0001
8	9	e	0.075	-	-	0.0005	-	0.0004
8	9	f	0.075	-	-	0.0007	-	0.0003
8	10	a	0.1	-	0.1021	0.0095	-	0.0049
8	10	b	0.1	0.1548	0.1227	0.0496	0.0649	0.0373
8	10	c	0.1	0.1332	0.0755	0.0432	0.0641	0.0247
8	10	d	0.1	0.0274	0.0851	0.0198	-	0.0100

Q (cfs)	Cross-section Number	Location	Relative Depth (y/h) for TKE and Reynolds Methods	Method				
				Law of the Wall (psf)	Preston Tube (psf)	Reynolds – Near-bed Point (psf)	Reynolds – Extrapolated (psf)	TKE (psf)
8	10	e	0.1	-	0.0148	0.0022	-	0.0025
8	10	f	0.125	-	-	0.0004	-	0.0003
8	10	g	0.1	-	-	0.0001	-	0.0004
8	11	b	0.1	0.0940	0.0878	0.0396	0.0711	0.0003
8	11	c	0.1	0.0532	0.0965	0.0366	0.0666	0.0080
8	11	d	0.1	0.0333	0.1104	0.0214	-	0.0004
8	11	e	0.1	0.0195	0.0719	0.0135	-	0.0014
8	11	f	0.1	-	0.0251	0.0042	-	0.0004
8	12	b	0.1	-	0.2237	0.0251	-	0.0151
8	12	c	0.2	-	0.3191	0.0365	0.0581	0.0002
8	12	d	0.1	0.0481	0.1294	0.0344	0.0497	0.0219
8	12	e	0.1	0.0567	0.0880	0.0331	0.0449	0.0127
8	12	f	0.1	0.0283	0.0376	0.0186	-	0.0027
8	13	b	0.1	0.0751	0.0253	0.0088	0.0227	0.0023
8	13	c	0.1	0.0449	0.0938	0.0254	-	0.0083
8	13	d	0.1	0.0371	0.0985	0.0335	-	0.0207
8	13	e	0.1	0.0481	0.0961	0.0259	0.0535	0.0168
8	13	f	0.1	0.0588	0.0739	0.0175	0.0609	0.0054
8	13	g	0.1	0.0725	0.0461	0.0143	-	0.0004
8	14	b	0.1	-	0.0329	0.0112	-	0.0012
8	14	c	0.1	0.0330	0.0853	0.0193	0.0241	0.0130
8	14	d	0.1	0.0641	0.1115	0.0362	0.0458	0.0225
8	14	e	0.1	0.0789	0.1521	0.0381	0.0597	0.0002
8	14	f	0.1	0.0723	0.0620	0.0357	0.0590	0.0073
8	14	g	0.1	0.0228	0.0685	0.0029	-	0.0013
8	15	b	0.1	0.1082	0.0529	0.0182	0.0204	0.0111
8	15	c	0.1	0.1000	0.0876	0.0240	0.0311	0.0131
8	15	d	0.1	0.0818	0.1333	0.0234	0.0385	0.0249
8	15	e	0.1	0.0765	0.1254	0.0384	-	0.0050
8	15	f	0.1	0.1947	0.0950	0.0298	0.1020	0.0003

Q (cfs)	Cross-section Number	Location	Relative Depth (y/h) for TKE and Reynolds Methods	Method				
				Law of the Wall (psf)	Preston Tube (psf)	Reynolds – Near-bed Point (psf)	Reynolds – Extrapolated (psf)	TKE (psf)
8	16	b	0.1	0.0156	0.0334	0.0106	0.0218	0.0003
8	16	c	0.1	0.0394	0.1265	0.0188	0.0224	0.0058
8	16	d	0.1	0.0599	0.1187	0.0198	0.0310	0.0041
8	16	e	0.1	0.0825	0.1277	0.0360	0.0480	0.0088
8	16	f	0.2	0.1220	0.1109	0.0487	0.0711	0.0002
8	17	d	0.1	0.0389	0.0748	0.0107	-	0.0006
8	17	e	0.1	0.0786	0.0808	0.0250	-	0.0017
8	17	f	0.1	0.0512	0.1232	0.0297	-	0.0191
8	18	e	0.25	-	0.1162	0.0292	0.0491	0.0022
8	18	f	0.1	0.1269	0.1411	0.0481	-	0.0152
12	1	a	0.1	-	0.0007	0.0014	-	0.0021
12	1	b	0.1	0.0061	0.0246	0.0109	-	0.0234
12	1	c	0.1	0.0141	0.0325	0.0065	0.0150	0.0046
12	1	d	0.1	0.0123	0.0468	0.0071	0.0082	0.0055
12	1	e	0.2	0.0157	0.0287	0.0031	0.0070	0.0049
12	1	f	0.1	0.0122	0.0356	0.0051	0.0079	0.0073
12	1	g	0.1	0.0380	0.0374	0.0107	0.0173	0.0055
12	2	a	0.1	-	0.0090	0.0065	-	0.0080
12	2	b	0.1	0.0091	0.0121	0.0068	-	0.0023
12	2	c	0.1	0.0166	0.0215	0.0063	-	0.0016
12	2	d	0.15	0.0171	0.0264	0.0073	0.0136	0.0045
12	2	e	0.1	0.0160	0.0163	0.0076	-	0.0025
12	2	f	0.1	0.0099	0.0282	0.0064	0.0114	0.0025
12	2	g	0.1	0.0601	0.0188	0.0092	-	0.0021
12	3	a	0.1	0.0568	0.0175	0.0087	0.0147	0.0041
12	3	b	0.1	0.0273	0.0246	0.0089	-	0.0023
12	3	c	0.1	0.0242	0.0782	0.0081	0.0111	0.0071
12	3	d	0.1	0.0052	0.1138	0.0052	0.0069	0.0073
12	3	e	0.1	0.0093	0.1196	0.0051	-	0.0079
12	3	f	0.1	0.0602	0.0343	0.0067	-	0.0004

Q (cfs)	Cross-section Number	Location	Relative Depth (y/h) for TKE and Reynolds Methods	Method				
				Law of the Wall (psf)	Preston Tube (psf)	Reynolds – Near-bed Point (psf)	Reynolds – Extrapolated (psf)	TKE (psf)
12	3	g	0.1	0.0383	0.0123	0.0058	0.0075	0.0008
12	4	a	0.1	0.0042	0.1171	0.0212	0.0224	0.0209
12	4	b	0.1	0.0383	0.1062	0.0118	0.0142	0.0099
12	4	c	0.1	0.0875	0.1038	0.0074	0.0088	0.0170
12	4	d	0.1	0.0480	0.0535	0.0106	0.0180	0.0002
12	4	e	0.1	0.0184	0.0636	0.0117	0.0298	0.0086
12	4	f	0.1	0.0386	0.0700	0.0167	-	0.0036
12	5	a	0.1	-	0.0301	0.0171	-	0.0040
12	5	b	0.1	0.0751	0.0841	0.0146	0.0212	0.0155
12	5	c	0.1	0.0446	0.1100	0.0121	0.0193	0.0169
12	5	d	0.1	0.1136	0.0815	0.0148	0.0197	0.0085
12	5	e	0.1	0.0786	0.0527	0.0150	0.0193	0.0007
12	5	f	0.1	0.0699	0.0542	0.0115	0.0192	0.0019
12	5	g	0.1	-	0.0141	0.0018	-	0.0014
12	6	a	0.1	0.0227	0.0535	0.0148	0.0239	0.0053
12	6	b	0.1	0.0222	0.1060	0.0101	-	0.0153
12	6	c	0.1	0.0419	0.0728	0.0122	0.0194	0.0047
12	6	d	0.1	0.0243	0.0966	0.0117	0.0212	0.0091
12	6	e	0.1	0.0109	0.0728	0.0093	-	0.0085
12	6	f	0.1	0.0301	0.0630	0.0064	-	0.0019
12	6	g	0.1	0.0099	0.0159	0.0030	-	0.0030
12	7	a	0.1	0.0340	0.0517	0.0236	0.0330	0.0157
12	7	b	0.1	0.0447	0.1265	0.0170	0.0218	0.0222
12	7	c	0.1	0.0386	0.0748	0.0192	-	0.0020
12	7	d	0.1	0.0093	0.1235	0.0121	-	0.0159
12	7	e	0.1	0.0604	0.1041	0.0150	-	0.0068
12	7	f	0.1	0.0194	0.0792	0.0072	-	0.0008
12	8	a	0.1	0.3932	0.0756	0.0455	0.0582	0.0033
12	8	b	0.1	0.0809	0.1517	0.0254	-	0.0326
12	8	c	0.1	0.0674	0.1518	0.0275	0.0413	0.0109

Q (cfs)	Cross-section Number	Location	Relative Depth (*y/h*) for TKE and Reynolds Methods	Method				
				Law of the Wall (psf)	Preston Tube (psf)	Reynolds – Near-bed Point (psf)	Reynolds – Extrapolated (psf)	TKE (psf)
12	8	d	0.125	0.0185	0.1549	0.0204	-	0.0142
12	8	e	0.075	-	0.0973	0.0173	-	0.0061
12	9	a	0.1	0.0091	0.0892	0.0354	0.0499	0.0152
12	9	b	0.1	0.0383	0.0824	0.0525	0.0540	0.0122
12	9	c	0.1	0.0746	0.1035	0.0389	0.0456	0.0089
12	9	d	0.1	0.0072	0.0563	0.0119	-	0.0034
12	9	e	0.125	0.0077	0.0269	0.0093	-	0.0058
12	9	f	0.1	-	-	0.0018	-	0.0029
12	9	g	0.1	-	-	0.0006	-	0.0034
12	10	a	0.1	-	0.1544	0.0267	-	0.0049
12	10	b	0.1	0.0193	0.1200	0.0292	-	0.0190
12	10	c	0.1	0.0523	0.0776	0.0298	0.0362	0.0029
12	10	d	0.1	0.0213	0.0898	0.0170	-	0.0086
12	10	e	0.1	0.0088	0.0393	0.0054	-	0.0040
12	10	f	0.1	0.0058	0.0053	0.0043	-	0.0020
12	10	g	0.1	-	-	0.0017	-	0.0026
12	11	a	0.1	-	0.0424	0.0144	-	0.0044
12	11	b	0.1	0.0563	0.1410	0.0378	-	0.0033
12	11	c	0.1	0.0478	0.0994	0.0252	0.0330	0.0179
12	11	d	0.125	-	0.1144	0.0253	0.0317	0.0035
12	11	e	0.15	-	0.0822	0.0147	-	0.0041
12	11	f	0.1	0.0066	0.0473	0.0079	-	0.0033
12	11	g	0.1	-	0.0289	0.0021	-	0.0024
12	12	a	0.1	0.1566	0.0634	0.0009	-	0.0063
12	12	c	0.25	-	0.4235	0.0370	-	0.0029
12	12	d	0.125	0.0575	0.1478	0.0241	0.0414	0.0341
12	12	e	0.1	0.0241	0.0981	0.0318	-	0.0219
12	12	f	0.15	0.0666	0.1003	0.0216	-	0.0101
12	13	b	0.125	0.0125	0.0835	0.0158	-	0.0050
12	13	c	0.1	0.1213	0.1413	0.0417	0.0711	0.0143

Q (cfs)	Cross-section Number	Location	Relative Depth (y/h) for TKE and Reynolds Methods	Method				
				Law of the Wall (psf)	Preston Tube (psf)	Reynolds – Near-bed Point (psf)	Reynolds – Extrapolated (psf)	TKE (psf)
12	13	d	0.1	0.1134	0.1317	0.0354	-	0.0159
12	13	e	0.1	0.0325	0.1505	0.0460	-	0.0052
12	13	f	0.15	0.0416	0.0967	0.0270	-	0.0041
12	13	g	0.4	-	0.0773	0.0179	-	0.0050
12	14	b	0.075	0.0141	0.0782	0.0151	-	0.0061
12	14	c	0.1	0.0066	0.1601	0.0267	-	0.0125
12	14	d	0.1	0.0222	0.1664	0.0505	-	0.0221
12	14	e	0.125	0.0508	0.1077	0.0391	-	0.0064
12	14	f	0.075	0.0703	0.0815	0.0386	-	0.0069
12	14	g	0.1	-	0.1232	0.0010	-	0.0110
12	15	b	0.125	0.0277	0.1337	0.0255	0.0393	0.0054
12	15	c	0.15	0.0318	0.1836	0.0283	-	0.0118
12	15	d	0.1	0.0706	0.2181	0.0366	-	0.0131
12	15	e	0.125	0.3241	0.2172	0.0475	-	0.0046
12	15	f	0.2	0.0961	0.1682	0.0448	-	0.0045
12	16	a	0.1	-	0.0141	0.0027	-	0.0043
12	16	b	0.15	-	0.0450	0.0159	-	0.0046
12	16	c	0.2	-	0.1637	0.0275	-	0.0044
12	16	d	0.15	0.0429	0.1492	0.0294	0.0372	0.0124
12	16	e	0.125	0.0830	0.1653	0.0435	-	0.0165
12	16	f	0.2	0.1018	0.1608	0.0654	-	0.0057
12	17	b	0.1	-	0.0103	0.0012	-	0.0055
12	17	c	0.1	-	0.0511	0.0038	-	0.0032
12	17	d	0.075	-	0.1238	0.0050	-	0.0045
12	17	e	0.15	-	0.1754	0.0371	-	0.0104
12	17	f	0.075	0.1126	0.1733	0.0434	-	0.0068
12	17	g	0.1	-	0.2004	0.0041	-	0.0043
12	18	d	0.125	0.0377	0.1870	0.0337	-	0.0105
12	18	e	0.2	0.0844	0.0947	0.0365	-	0.0337
12	18	f	0.15	0.0777	0.1709	0.0373	-	0.0231

Q (cfs)	Cross-section Number	Location	Relative Depth (y/h) for TKE and Reynolds Methods	Method				
				Law of the Wall (psf)	Preston Tube (psf)	Reynolds – Near-bed Point (psf)	Reynolds – Extrapolated (psf)	TKE (psf)
16	1	a	0.1	-	-	0.0042	-	0.0059
16	1	b	0.1	0.0048	0.0616	0.0073	-	0.0201
16	1	c	0.1	0.0138	0.0473	0.0036	-	0.0049
16	1	d	0.1	0.0078	0.0571	0.0040	-	0.0079
16	1	e	0.1	0.0218	0.0396	0.0063	0.0096	0.0071
16	1	f	0.1	0.0155	0.0446	0.0051	0.0071	0.0069
16	1	g	0.1	0.0327	0.0349	0.0117	0.0168	0.0073
16	2	a	0.1	0.0069	0.0128	0.0079	-	0.0110
16	2	b	0.1	0.0047	0.0233	0.0079	0.0152	0.0103
16	2	c	0.1	0.0127	0.0264	0.0107	-	0.0065
16	2	d	0.1	0.0187	0.0251	0.0110	-	0.0046
16	2	e	0.1	0.0053	0.0199	0.0109	0.0107	0.0052
16	2	f	0.1	0.0164	0.0316	0.0081	0.0094	0.0089
16	2	g	0.1	0.0316	0.0260	0.0094	-	0.0047
16	3	a	0.1	0.0077	0.0228	0.0075	0.0113	0.0057
16	3	b	0.1	0.0058	0.0293	0.0141	-	0.0038
16	3	c	0.1	0.0192	0.0712	0.0089	0.0107	0.0070
16	3	d	0.1	0.0119	0.1115	0.0041	-	0.0071
16	3	e	0.1	0.0072	0.1196	0.0043	-	0.0082
16	3	f	0.1	0.0235	0.0394	0.0113	0.0178	0.0047
16	3	g	0.1	0.0122	0.0139	0.0065	-	0.0045
16	4	a	0.1	0.0377	0.1630	0.0110	-	0.0225
16	4	b	0.1	0.0072	0.1303	0.0149	0.0162	0.0068
16	4	c	0.1	0.0070	0.1247	0.0123	0.0193	0.0157
16	4	d	0.1	0.1199	0.0746	0.0137	0.0246	0.0117
16	4	e	0.1	0.0366	0.0730	0.0133	0.0438	0.0092
16	4	f	0.1	0.0200	0.0876	0.0150	-	0.0051
16	4	g	0.1	0.0115	0.1180	0.0097	-	0.0106
16	5	a	0.1	0.0999	0.0524	0.0305	0.0358	0.0061
16	5	b	0.1	0.0510	0.0880	0.0207	0.0400	0.0237

Q (cfs)	Cross-section Number	Location	Relative Depth (y/h) for TKE and Reynolds Methods	Method				
				Law of the Wall (psf)	Preston Tube (psf)	Reynolds – Near-bed Point (psf)	Reynolds – Extrapolated (psf)	TKE (psf)
16	5	c	0.1	0.0385	0.1355	0.0163	-	0.0205
16	5	d	0.1	0.0893	0.0994	0.0166	0.0231	0.0166
16	5	e	0.1	0.0368	0.0710	0.0163	0.0243	0.0076
16	5	f	0.1	0.1477	0.0851	0.0152	0.0239	0.0047
16	6	a	0.1	0.0211	0.0761	0.0179	0.0200	0.0085
16	6	b	0.1	0.0180	0.1140	0.0156	-	0.0060
16	6	c	0.1	0.0176	0.0891	0.0138	0.0171	0.0075
16	6	d	0.1	0.0135	0.1236	0.0166	0.0279	0.0163
16	6	e	0.1	0.0416	0.0929	0.0117	0.0330	0.0070
16	6	f	0.1	0.0127	0.0735	0.0087	0.0142	0.0091
16	6	g	0.1	0.0046	0.0163	0.0032	-	0.0038
16	7	a	0.1	0.0793	0.0645	0.0261	0.0406	0.0069
16	7	b	0.1	0.0397	0.1294	0.0321	-	0.0113
16	7	c	0.1	0.0914	0.0755	0.0192	-	0.0055
16	7	d	0.1	0.0402	0.0950	0.0171	0.0211	0.0105
16	7	e	0.1	0.0147	0.1142	0.0123	-	0.0148
16	7	f	0.1	-	0.0770	0.0101	-	0.0059
16	7	g	0.1	-	0.0880	0.0019	-	0.0072
16	8	a	0.1	0.0563	0.1319	0.0386	0.0438	0.0102
16	8	b	0.1	-	0.2452	0.0225	0.0335	0.0282
16	8	c	0.1	0.0332	0.2573	0.0328	0.0378	0.0140
16	8	d	0.1	0.0195	0.1830	0.0203	-	0.0104
16	8	e	0.125	-	0.1563	0.0210	-	0.0050
16	8	f	0.125	0.0191	0.1333	0.0163	0.0264	0.0169
16	8	g	0.2	-	0.0481	0.0116	-	0.0022
16	9	a	0.1	0.0165	0.1704	0.0380	0.0490	0.0274
16	9	b	0.1	0.0710	0.1556	0.0407	0.0542	0.0241
16	9	c	0.1	0.0887	0.1545	0.0345	0.0447	0.0044
16	9	d	0.1	0.0158	0.0696	0.0190	0.0226	0.0030
16	9	e	0.1	0.0098	0.0696	0.0127	-	0.0056

Q (cfs)	Cross-section Number	Location	Relative Depth (y/h) for TKE and Reynolds Methods	Method				
				Law of the Wall (psf)	Preston Tube (psf)	Reynolds – Near-bed Point (psf)	Reynolds – Extrapolated (psf)	TKE (psf)
16	9	f	0.125	0.0152	0.0322	0.0079	-	0.0037
16	9	g	0.1	-	-	0.0032	-	0.0055
16	10	a	0.1	0.0111	0.1648	0.0414	0.0465	0.0200
16	10	b	0.1	0.0205	0.1359	0.0360	-	0.0357
16	10	c	0.1	0.0429	0.1205	0.0235	-	0.0050
16	10	d	0.1	0.0164	0.1312	0.0181	-	0.0148
16	10	e	0.1	0.0123	0.0723	0.0123	-	0.0063
16	10	f	0.1	0.0028	0.0376	0.0073	-	0.0056
16	10	g	0.1	0.0046	0.0094	0.0040	-	0.0058
16	11	a	0.1	0.0191	0.1095	0.0183	-	0.0082
16	11	b	0.1	-	0.1350	0.0474	0.0560	0.0362
16	11	c	0.1	0.0466	0.0773	0.0329	0.0437	0.0238
16	11	d	0.1	-	0.1250	0.0230	0.0270	0.0190
16	11	e	0.1	0.0054	0.1062	0.0169	-	0.0063
16	11	f	0.1	0.0161	0.0822	0.0114	-	0.0044
16	12	b	0.2	-	0.3451	0.0424	0.0623	0.0361
16	12	d	0.1	0.0420	0.2372	0.0294	0.0387	0.0324
16	12	e	0.1	0.0229	0.1478	0.0259	0.0380	0.0238
16	12	f	0.15	-	0.0952	0.0219	-	0.0075
16	13	a	0.125	0.0273	0.1142	0.0150	-	0.0151
16	13	b	0.1	0.1102	0.2110	0.0260	0.0403	0.0080
16	13	c	0.1	0.0248	0.1933	0.0351	0.0935	0.0256
16	13	d	0.1	0.0366	0.2266	0.0313	-	0.0255
16	13	e	0.1	0.0493	0.1574	0.0337	0.0360	0.0131
16	13	f	0.1	0.0244	0.1001	0.0357	0.0373	0.0041
16	13	g	0.125	0.0341	0.0681	0.0419	0.0436	0.0055
16	14	a	0.1	0.0402	0.0822	0.0133	-	0.0105
16	14	b	0.1	0.0045	0.1404	0.0315	0.0368	0.0244
16	14	c	0.1	0.0190	0.1803	0.0245	0.0647	0.0255
16	14	d	0.1	0.0323	0.3227	0.0295	-	0.0360

Q (cfs)	Cross-section Number	Location	Relative Depth (*y/h*) for TKE and Reynolds Methods	Method				
				Law of the Wall (psf)	Preston Tube (psf)	Reynolds – Near-bed Point (psf)	Reynolds – Extrapolated (psf)	TKE (psf)
16	14	e	0.1	0.0505	0.0000	0.0369	0.0467	0.0140
16	14	f	0.4	0.0715	0.2013	0.0301	0.0484	0.0096
16	14	g	0.3	0.0227	0.1498	0.0188	0.0374	0.0069
16	15	b	0.2	-	0.1966	0.0390	-	0.0074
16	15	c	0.125	0.0694	0.2484	0.0420	0.0509	0.0559
16	15	d	0.1	0.0862	0.2656	0.0480	0.0543	0.0792
16	15	e	0.1	0.0397	0.2284	0.0459	-	0.0327
16	15	f	0.2	0.2126	0.2013	0.0473	-	0.0020
16	15	g	0.1	-	0.0813	0.0026	-	0.0036
16	16	a	0.1	-	0.0101	0.0024	-	0.0046
16	16	b	0.1	0.0308	0.0880	0.0293	-	0.0044
16	16	c	0.15	0.0405	0.2103	0.0338	-	0.0120
16	16	d	0.1	0.0711	0.1724	0.0464	-	0.0192
16	16	e	0.1	0.1126	0.1984	0.0525	-	0.0532
16	16	f	0.2	0.1514	0.1518	0.0509	-	0.0024
16	16	g	0.1	-	0.0936	0.0006	-	0.0034
16	17	b	0.1	0.0054	0.0188	0.0037	0.0064	0.0049
16	17	c	0.125	0.0136	0.0654	0.0075	-	0.0743
16	17	d	0.125	0.0053	0.1494	0.0267	-	0.0130
16	17	e	0.15	0.0517	0.2298	0.0335	-	0.0127
16	17	f	0.125	0.0688	0.3176	0.0440	-	0.0199
16	18	b	0.2	0.1459	0.1180	0.0142	-	0.0135
16	18	c	0.25	-	0.1221	0.0252	-	0.0041
16	18	d	0.1	0.0147	0.1756	0.0290	-	0.1081
16	18	e	0.1	0.0321	0.1986	0.0660	0.0635	0.0039
16	18	f	0.15	0.0724	0.2302	0.0480	0.0612	0.0141
16	18	g	0.3	-	0.2387	0.0388	-	0.0038

- denotes fields that are not applicable